WM-12

MEASUREMENTS OF 2p-1s LINE WIDTHS IN LOW-Z PIONIC ATOMS

A Thesis

Presented to

The Faculty of the Department of Physics

The College of William and Mary in Virginia

NSG 567

In Partial Fulfillment

Of the Requirements for the Degree of

Doctor of Philosophy

---

by

Robert J. Harris, Jr.

January 1968

MEASUREMENTS OF 2p-1s LINE WIDTHS IN LOW-Z PIONIC ATOMS

TABLE OF CONTENTS

I. ABSTRACT

The natural line widths of 2p-1s transitions in low-Z pionic atoms have been measured using high-resolution lithium-drifted silicon [Si(Li)] and germanium [Ge(Li)] detectors. High resolution was achieved by developing a low-noise cooled FET preamplifier which allowed the inherently good resolving capability of Si(Li) and Ge(Li) detectors to be more fully exploited than was previously possible. The instrumental resolution as measured with muonic X-rays was 0.62 keV (FWHM) at 33 keV for the Si(Li) spectrometer, and 1.1 keV (FWHM) at 75 keV for the Ge(Li) spectrometer.

Pionic atoms were formed by stopping negative pions in the following targets: Li^6, Li^7, Be^9, B^{10}, B^{11}, and C^{12}. The results obtained for pionic 2p-1s natural line widths were:

$$\Gamma(Li^6) = 0.15 \pm 0.05 \text{ keV}$$
$$\Gamma(Li^7) = 0.19 \pm 0.05 \text{ keV}$$
$$\Gamma(Be^9) = 0.58 \pm 0.05 \text{ keV}$$
$$\Gamma(B^{10}) = 1.68 \pm 0.12 \text{ keV}$$
$$\Gamma(B^{11}) = 1.72 \pm 0.15 \text{ keV}$$
$$\Gamma(C^{12}) = 3.25 \pm 0.15 \text{ keV}$$

Theoretical values for the natural line widths were computed from the theory of Ericson and Ericson and found to be in good agreement with the above measured results.

II. INTRODUCTION

In 1935, Yukawa[1] introduced a theory of nuclear forces in which the force between two nucleons was represented by a quantized field. From the approximate range of nuclear forces ($\approx 10^{-13}$ cm), the mass of the particles representing the quanta of this field was estimated to be of the order of 200 electron masses. In 1938, Neddermeyer and Anderson[2] observed a particle from cosmic radiation which was thought to be the Yukawa particle; however, a subsequent experiment by Conversi et.al.,[3] showed that this particle interacted too weakly with matter to account for the strong nuclear forces. This weakly interacting particle has since become known as the muon. The Yukawa particle was discovered in 1947 by Powell et.al.,[4] in a series of experiments in which sensitive emulsion plates were exposed to cosmic radiation. This particle, now called the pion, was observed to produce "stars" at the end of its emulsion track which were interpreted as resulting from nuclear excitation following the nuclear capture of a negative pion. With the advent of particle accelerators, pions were produced artificially in nucleon-nucleon collisions, confirming the basic concept that pions were the quanta of the nuclear force field.

The possible existence of mesic atoms was first suggested by Fermi et.al.,[5] in a paper describing the interaction of slow mesons with matter. A negative meson traveling through condensed matter was

assumed to lose its kinetic energy through ionizing collisions with atomic electrons until it was captured at rest by an atom into a Bohr orbit. Subsequent transitions between Bohr levels were then made by the meson to levels of low principal quantum number from which nuclear capture occurred. Fermi and Teller[6] calculated that the time required for a slow (2000 eV) negative meson to reach the atomic K-shell was of the order of 10^{-13} sec. For the pion, the mean life against free decay is about 2.6×10^{-8} sec which is long compared with the time estimated for the formation of a pionic atom and the subsequent cascade to the K-shell. In accordance with these theoretical considerations, a negative pion stopping in condensed matter should form a pionic atom and reach the ground state before decaying. This postulate could be confirmed experimentally by observing the characteristic X-rays emitted during the cascade process. Conclusive evidence of the formation of pionic atoms was first obtained by Camac et.al.,[7] who stopped negative pions in graphite and studied the radiation emitted with a scintillation counter. A peak was observed at approximately 100 keV which corresponded to the pionic K_α line in carbon.

Subsequent interest in pionic atoms has resulted from the possibility of obtaining specific information about the pion-nucleus strong interaction by studying pionic transitions. This idea was implicit in the work of Wheeler[8] who suggested that the nature of the weak muon-nucleus interaction could be investigated experimentally with muonic atoms. The main properties of a pionic atom are given by the Bohr equations for the energy, radius, and velocity corresponding to principal quantum number n:

$$E_n = -(m_\pi/2)(Z\alpha c/n)^2$$

$$r_n = (\hbar^2/m_\pi e\ )(n^2/Z)$$

$$V_n = Z\alpha c/n$$

Several conclusions are immediately obvious from these equations:

1. the radii of the pionic Bohr orbits are smaller than those of the corresponding electronic orbits by the ratio $m_\pi/m_e \simeq 273$.
2. the transition energies for the pionic atom are larger than those of the corresponding electronic atom by a factor of approximately 273.
3. since the velocity is independent of mass, one can expect relativistic effects to be no more important for the pionic atom than for the electronic atom.

As a consequence of the small Bohr radii for pionic atoms, most of the cascade process takes place within the electron shells and, therefore, the pionic atom may be treated as a hydrogen-like atom to a very good approximation. For example, the $n = 17$ level of the pionic atom has a Bohr radius which corresponds to that of the K-electron. Therefore, the energy levels corresponding to a low principal quantum number can be calculated to high accuracy and can serve as a basis for studying the pion-nucleus interaction. The major corrections to the energy levels predicted by simple Bohr theory are:

1. <u>finite nuclear size</u> - accounted for by solving the wave equation assuming a uniform charge distribution for the nucleus; <u>i.e.</u>,

$$V_{coul}(r>R) = -Ze^2/r$$

$$V_{coul}(r<R) = (Ze^2/2R)[-3 + (r/R)^2],$$

where R is the nuclear radius.

2. relativistic corrections - taken into account by using the Klein-Gordon wave equation. For a point nucleus, the energy levels are:

$$E_{n,\ell} = -\frac{m_\pi c^2}{2n^2}(Z\alpha)^2\left[1 + \frac{(Z\alpha)^2}{n^2}\left(\frac{n}{\ell + 1/2} - \frac{3}{4}\right)\right]$$

where higher order terms have been neglected.

3. vacuum polarization correction - corrections obtained from quantum electrodynamics.[9]
4. Pion-nucleus interaction - specific form not known.

All effects on pionic energy levels, except the last, are known and can be calculated. Thus, measurements of pionic transitions can yield information about the pion-nucleus interaction, which is related directly to the more basic pion-nucleon interaction.

The strong interaction between the pion and nucleus is expected to manifest itself in a pionic atom through three effects:

1. broadening of energy levels due to rapid absorption of the pion by the nucleus.
2. shift of energy levels due to pion-nucleus interaction.
3. decrease in intensity of pionic X-rays vs Z due to nuclear capture of the pion before completion of the cascade to the ground state.

These effects were first studied experimentally by DeBenedetti et.al.,[10,11] West and Bradley,[12,13] Camac et.al.,[14] and Stearns and Stearns[15] by means of proportional counters, scintillation counters, and critical absorber

techniques. At the same time, Brueckner[16] and Deser et.al.,[17] were doing a theoretical study of the pion-nucleus interaction. A review article covering all aspects of this work was written by West[18] in 1957. The amount of information and precision of the results obtained during this period were limited by the low pion beam intensities and the poor resolution of the detectors. In the past several years, the advent of both high resolution semi-conductor detectors and more intense pion beams has made possible the extension of these earlier measurements over a wider range of elements with greater precision. In addition, the recent theoretical work of Ericson and Ericson[19] treats the low energy pion-nucleus interaction in considerably more detail than earlier work and, therefore, makes a precise measurement of pionic X-rays desirable. The work described in this thesis was concerned with the measurement of pionic 2p-1s line broadening in low Z atoms and comparison of the results with theoretical predictions as well as with previous measurements.[20,21]

In a pionic atom, the wave-function-overlap with the nucleus and the strong pion-nucleus interaction leads to very rapid absorption of pions from the 1s state. If the 1s state is assumed to be depleted exponentially with time according to $e^{-\omega_{abs}t}$, then it is not a stationary state of definite energy E_{1s}, but has a probability distribution of energies given by a Lorentzian function:[22]

$$L(E) = \frac{A}{(E - E_{1s})^2 + (\hbar\omega_{abs}/2)^2}$$

where $\hbar\omega_{abs} = \Gamma_{nat}$ is the FWHM of the distribution .

Thus, as a result of the rapid pion absorption by the nucleus, the 1s level in a pionic atom is broadened. The natural line width is given by Γ_{nat} and is consistent with the uncertainty principle. Experimentally, one measures the 2p-1s transition energy, and therefore, the observed natural line width represents width contributions from the 2p and the 1s states. The width contribution of the 2p state is due to the radiative transition rate to the 1s state and is negligible since, for example, in Be^9:

$$\omega_{abs}(1s) \simeq 10^{18}/\text{sec}$$
$$\omega_{rad}(2p) \simeq 10^{14}/\text{sec}$$

Therefore, the natural line width of the 2p-1s transition in a pionic atom will yield directly the nuclear absorption rate of pions from the 1s state.

Theoretical descriptions of the process in which a negative pion is absorbed by a complex nucleus are based on concepts introduced by Brueckner et.al.[23] in 1951. The characteristic feature of the absorption process is the release of the pion rest mass energy (139 meV) in the form of kinetic energy of the absorbing nucleons. Absorption is assumed to involve at least two nucleons in order to conserve energy and momentum. Although the one-nucleon process $\pi^- + p \rightarrow n$ is strictly forbidden for free nucleons, the same process for nucleons in a complex nucleus is only quasi-forbidden since the nucleus can provide an external source of momentum through Fermi motion. The momentum balance required for the absorption of a zero-energy pion on a resting proton is obtained

by the conservation of total relativistic energy:

$$(m_\pi + m_p)^2c^4 = p_n^2c^2 + m_n^2c^4$$

$$p_n \simeq \sqrt{2m_\pi m_p c^2} = 525 \text{ MeV/c}$$

This is just the momentum acquired by the proton due to absorption of the pion rest mass energy. Since the Fermi momentum is approximately 250 MeV/c, the one-nucleon absorption is strongly inhibited. Thus, a negative pion in nuclear matter is assumed to be absorbed by a pair of nucleons in a process which is the inverse of pion production in the collision of the two nucleons; i.e.,

$$\pi^- + p + n \rightarrow n + n$$

$$\pi^- + p + p \rightarrow n + p$$

From these considerations, Brueckner assumed that the absorption rate from the 1s state of a pionic atom was proportional to the transition probability per second for the reaction $\pi^- + D \rightarrow n + n$, i.e.,

$$\omega_A = \frac{K|\Phi_A(0)|^2}{|\Phi_D(0)|^2} Z_A\omega_D$$

where $\Phi(0)$ = wave function of the pionic 1s state evaluated at $r = 0$,

Z_A = charge for nucleus A,

K = constant

The deuteron absorption rate, ω_D, was obtained from the measured cross section for the reaction $p + p \rightarrow \pi^+ + D$ by the principle of detailed balance and with the assumption of charge independence. The following approximate expression was obtained by Brueckner[16] for the natural line width (FWHM) of 1s levels in pionic atoms:

$$\Gamma_{1s}(\text{Brueckner}) = (2Z^2/2150)E_Z \qquad (1)$$

where E_Z is the K-shell binding energy, $(m_\pi/2)(Z\alpha)^2$.

The general trend of the measured widths[24] is described by eq. (1).

An alternative description of the pion-nucleus interaction is obtained by means of an optical model potential; i.e.,

$$V = V_R - iV_I \ , \ V_I > 0$$

There will be a complex energy shift associated with V which reflects the perturbation of the Bohr energy levels due to the pion-nucleus interaction:

$$E_{tot} = E_o + \Delta E$$

where $\Delta E = \Delta E_R - i\Delta E_I$

E_o = unperturbed energy

The time dependence of the pionic wave function is given by

$$e^{-iE_{tot}t/\hbar} = e^{-i(E_o + \Delta E_R)t/\hbar} \cdot e^{-\Delta E_I t/\hbar}$$

The probability density for finding the pion in a certain state at time t is given by the absolute square of the wave function.

$$e^{-2\Delta E_I t/\hbar} = e^{-\omega_{abs} t} .$$

Therefore, the imaginary part of V leads to an exponential decay of the system and results in a broadening of the energy level from which pion capture occurs. In terms of the imaginary part of the level shift, the natural line width is given by:

$$\Gamma_{nat} = 2\Delta E_I$$

Ericson and Ericson[19] have recently derived a phenomenological optical potential describing the pion-nucleus interaction by using a multiple scattering approach. The parameters in the potential were determined from the amplitudes for πN scattering and for π production

in NN collisions. The technique used to obtain the potential is closely connected to the solution of the wave equation by means of the Green's function $G(r,r')$. The formal solution to the wave equation

$$(\nabla^2 + K^2)\psi(r) = U(r)\psi(r)$$

$$\text{where } K^2 = 2mE/\hbar^2$$

$$U(r) = 2mV(r)/\hbar^2$$

can be written as

$$\psi(r) = \psi_0(r) + \int G(r,r')U(r')\psi(r')dr' \qquad (2)$$

where the Green's function is the solution of the wave equation with a delta function source

$$(\nabla^2 + K^2)G(r,r') = \delta(r-r').$$

and

$$(\nabla^2 + K^2)\psi_0 = 0.$$

In the multiple scattering approach of the Ericsons', the solution for the total wave function of the pion-nucleus system is expressed in the form of an integral equation similar to equation (2) which yields the optical potential directly. The pion-nucleus interaction is viewed as a complicated process in which the pion undergoes multiple elastic and inelastic scattering with nucleons. The assumption is made that bound nucleons scatter pions in the same way as free nucleons, with the exception of kinematical factors, and that s and p wave pion-nucleon scattering are sufficient for a description of the interaction. The total wave function ψ for the pion-nucleon system is written as the sum of the incident wave ψ_0 and the scattered wave emerging from each of

the scatterers in the nucleus. The scattered wave at the i^{th} nucleon is proportional to the scattering amplitude f_i and the wave Ψ_i incident on the i^{th} nucleon; i.e.,

$$\Psi(r) = \Psi_0(r) + \sum_i \int G(r,r') f_i(r') \Psi_i(r') \, dr'$$

By analogous reasoning, a similar expression can be written for Ψ_i where the sum is over index j with $i \neq j$. In this manner, the total wave function can be constructed through an expansion in terms of correlation functions which describe the degree of correlation among the nucleons participating in the multiple scattering. In practice, the expansion is terminated after a few terms and solved exactly. Termination at the earliest stage represents an uncorrelated assembly of nucleons in which a multiple scatter event proceeds without knowledge of a nearby scatterer; termination at the next step of pair correlations includes the effects of a neighboring scatterer in a way determined explicitly by the form of the correlation function. The Ericsons terminated the expansion at this step using a short-range pair correlation function and obtained the following potential for elastic scattering only:

$$V(r) = \frac{-\hbar^2}{2m} \left[4\pi b_0 \rho(r) - \frac{4\pi c_0 \nabla \cdot \rho(r) \nabla}{1 + \frac{4}{3}\pi c_0 \rho(r)} \right]$$

where the scattering amplitude was given by

$$f_i(r) = [b_0 + c_0 \vec{K} \cdot \vec{K}'] \rho(r), \quad \text{with}$$

b_0 = linear combination of s wave scattering lengths

c_0 = linear combination of p wave scattering lengths

$\vec{K}$ = initial pion momentum

$\vec{K}'$ = final pion momentum

$\rho(r)$ = nucleon density

This potential is in the form of the velocity dependent potential originally derived by Kisslinger.[25] An added feature is the non-linear dependence of the density through the factor $[1 + (4/3)\pi c_0 \rho(r)]^{-1}$. This factor enters as a result of including pair correlations in the multiple scattering formalism and has a classical analogue in the scattering of electromagnetic waves in dense media - the so-called Lorentz-Lorenz effect. The inclusion of spin and isospin terms in the scattering amplitude does not affect the basic structure of the potential but essentially modifies the coefficients b_0 and c_0. The velocity dependent, or non-local, term can be interpreted as an effective mass term since it can be included in the ∇^2 operator of the wave equation; i.e.,

$$\frac{\hbar^2}{2m_\pi} \nabla\cdot(1 + \alpha)\nabla\Psi + (E - V_L)\Psi = 0$$

$$\text{where } \frac{1 + \alpha}{m_\pi} = \frac{1}{m_\pi(\text{eff})}$$

$$V_L = \text{local part of potential}$$

The inelastic absorptive interaction is included by assuming that absorption takes place on two nucleons. Two nucleons are then treated as an additional type of scatterer in the multiple scattering formalism with $\rho^2(r)$ being used as the two-nucleon density. Two-nucleon elastic scattering is also permitted since the absorptive interaction may induce it, as pointed out by Brueckner.[16] The resulting potential due to two-nucleon interactions has a form similar to that derived for one-nucleon scattering with the exception that $\rho^2(r)$ replaces $\rho(r)$ and the coefficients are now complex. An analytic expression for the complex

energy shift due to the optical model potential has been obtained by M. Ericson[26]. The optical potential is represented in its simplest form in terms of four dominating parameters which describe the mean effect of the pion-nucleon interaction. The local part is represented by

$$V_L = \mu\rho + i\nu\rho^2$$

and the non-local part by the effective mass term

$$\alpha = a\rho + ib\rho^2 ,$$

where the imaginary parameters describe the absorption. The density $\rho(r)$ is assumed to be constant inside the nucleus of radius R and the complex energy shift is obtained by solving the Schrodinger equation

$$\frac{\hbar^2}{2m_\pi}\nabla\cdot(1+\alpha)\nabla\Psi + (E - V_{tot})\Psi = 0$$

$$\text{where } \frac{1+\alpha}{m_\pi} = \frac{1}{m_\pi(\text{eff})}$$

$$V_{tot}(r>R) = -Ze^2/r$$

$$V_{tot}(r<R) = (Ze^2/2R)[-3 + (r/R)^2] + V_L$$

which yields the following expression for the complex energy shift:

$$\Delta E = \frac{\dfrac{E_o(2K_oR)^{2\ell+2}}{(\ell+1)(2\ell+1)!}\left[-\dfrac{\alpha\ell}{K_oR} - \dfrac{2m_\pi V_L R}{\hbar^2 K_o(2\ell+3)} - \dfrac{3}{(2\ell+3)(2\ell+5)} - \cdots\right]}{1 + \dfrac{\alpha\ell}{2\ell+1} + 2K_oR\{1 + \alpha(1-\delta_{\ell o})/2\} + \dfrac{2m_\pi V_L R^2}{\hbar^2(2\ell+1)(2\ell+3)} + \cdots} \qquad (3)$$

where $E_o = -(m_\pi/2)(Z\alpha c/n)^2$

$K_o^2 = -2m_\pi E_o/\hbar^2$

ℓ = orbital angular momentum quantum number

$\delta_{\ell o}$ = Kronecker delta

Although the shift is given in terms of only four optical-model parameters representing the mean effect of the interaction, the formal theory[19] is developed in such a manner that corrections from various terms can be included directly into these four parameters. These corrections will be discussed in section VI where experimental and theoretical values of the natural line widths are compared.

In order to test more explicitly the hypothesis that absorption occurs on pairs of nucleons, M. Ericson[27] has also calculated an expression for the pion absorption probability in a complex nucleus by a different method - that based on a generalized deuteron model. This calculation is similar to the earlier one of Brueckner's[16] but is more detailed and presumably more accurate since the experimental cross sections for $(\pi,2N)$ interactions are now better known. Pion absorption by a pair of nucleons is assumed to occur by means of the following basic reactions:

$$\pi^- + p + n \rightarrow n + n$$

$$\pi^- + p + p \rightarrow n + p$$

The two absorbing nucleons are assumed to be in a relative S state because of the short range of the interaction. In addition, the pion is assumed to be absorbed from an s or p state relative to the two nucleons. The initial and final states available to the pion-two nucleon system are determined by invoking the Pauli exclusion principle and the conservation of total angular momentum and parity. The absorption probability associated with each transition can be obtained from the corresponding cross section for pion production in 2N collisions

by using the principles of detailed balance and charge independence. The transition states and corresponding cross sections are listed below:

Absorbing Pair	State of Initial Pair	State of Final Pair	Isotopic Spin Change	Production Cross Section
pn	$^3S_1$	$^3P_1$, $^1S_0$, or $^1D_2$	T=0 → T=1	σ_{01}
pn	$^1S_0$	$^3P_0$	T=1 → T=1	σ_{11}
pp	$^1S_0$	$^3P_0$	T=1 → T=1	σ_{11}
pp	$^1S_0$	$^3S_1$ or $^3D_1$	T=1 → T=0	σ_{10}

The capture probability in a nucleus corresponding to each transition is obtained by averaging the two-nucleon cross section over the interaction volume of the nucleus and approximating the two-nucleon density with the square of the one nucleon density. The total capture rate is then obtained by adding together the rates associated with each transition and results in the following expression for the natural line width ($\hbar = c = 1$):

$$\Gamma_{nat} = 2\nu \int \rho^2 |\Psi|^2 d\tau + (b/m_\pi) \int \rho^2 |\nabla\Psi|^2 d\tau \qquad (4)$$

where ρ = one-nucleon density

Ψ = pion wave function

$\nu = 165 \pm 20$ MeV F^6

$b = 17 \pm 4$ F^6

A direct comparison between the experimental line widths and the theoretical predictions given in this section tests the validity of

1. the two-nucleon absorption hypothesis and
2. the optical model potential based on multiple scattering theory.

Before 1966, no level width measurement other than one for Be^9 (West[13]) existed for comparison with theory. This result is in agreement with the estimate given by Brueckner[16] but disagrees with the predictions of Ericson and Ericson[19] by a factor of two. In more recent experiments,[20,21] the 1s level widths of low Z pionic atoms have been measured to approximately the same precision as the earlier Be^9 result. Although there is general agreement between the experimental results, the relatively large errors make a detailed comparison with theory difficult.

Because of the need for greater precision, an experimental program was undertaken to measure natural line widths using higher resolution spectrometers. These spectrometers, which consisted of lithium-drifted silicon and germanium detectors with cooled front-end electronics, represented approximately a factor of two improvement in resolution. Measurements are reported here on the pionic 1s natural line widths in Li^6, Li^7, Be^9, B^{10}, B^{11}, and C^{12}.

III. HIGH RESOLUTION SPECTROMETERS

The development of the Si(Li) and Ge(Li) spectrometers constituted a major portion of the experimental program and, therefore, will be described separately in this section. The next section will include a discussion of the ancillary equipment used in this experiment.

As mentioned in the previous section, high resolution is necessary in order to make precise line width measurements. The types of radiation detectors which are generally available for such measurements may be classified as solid-state or gas-filled. Solid-state detectors consist of the scintillation types (e.g., sodium iodide and cesium iodide) and those which are semi-conductors (e.g., germanium and silicon). Gas-filled detectors include ion chambers and proportional counters. In all of these detectors, energy is converted into charge by the formation of "ion-pairs" when incident radiation is absorbed. An analysis of the process of ion-pair formation shows that semi-conductor detectors are capable of the highest resolution. This point will be discussed next, after a brief description is given of semi-conductor detectors.

A. Semi-Conductor Detectors

The basic semi-conductor radiation detector[28] is fabricated from germanium or silicon to form a diode structure whose

junction becomes the sensitive region of the detector. The junction is a space charge or intrinsic region of very high resistance. A reverse bias voltage applied to the electrodes on opposite sides of the junction produces an electric field across the intrinsic region. When incident radiation is absorbed in the sensitive volume of the detector, electrons are raised to the conduction band and holes are left in the valence band. These electrons and holes, constituting "ion-pairs," are then collected by the electrodes under the action of the electric field. In this manner, charge is induced into an external circuit, resulting in the conversion of energy into an electrical signal.

Detectors with large sensitive volumes are made by an ion-drift technique which compensates the impurities in a semi-conductor forming a junction which can be greater than 1 cm deep. In this process, lithium ions (donor impurity) are typically made to drift through p-type germanium or silicon, originally containing a uniform distribution of acceptor centers, under the action of reverse voltage and controlled temperature. Commercial Ge(Li) and Si(Li) detectors so manufactured were used for this experiment. Fig. 1 illustrates this type of diode structure. These detectors must be operated at liquid nitrogen (LN) temperature in order to reduce the reverse leakage current which introduces noise and, in the case of germanium, to prevent the lithium from un-drifting.

Ge(Li) and Si(Li) detectors are capable of significantly better resolution than the other detectors mentioned previously. This fact becomes evident from a calculation of the energy spread (FWHM) due to

statistical fluctuations in the number of ion-pairs produced when energy E is absorbed in a detector. If the fluctuations in the amount of energy dissipated in a detector are assumed to be governed by Gaussian statistics (or Poisson statistics for a large number of events), then the energy spread is given by:

$$\text{FWHM(keV)} = 2.35\ \sigma_E\ ,$$

where σ_E represents the standard deviation in keV on the amount of energy deposited in the detector by an incident particle with energy E. Since the number of ion-pairs produced is the quantity which undergoes statistical fluctuations, σ_E must be obtained by calculating the standard deviation on the number of ion-pairs and then converting this to an energy deviation. If the average energy required to produce an ion-pair is ε and energy E is absorbed in a detector, then the average number of ion-pairs produced is E/ε. The standard deviation on the number of ion-pairs is then $\sqrt{E/\varepsilon}$ and the standard deviation in terms of energy becomes $\sqrt{E\varepsilon}$. Therefore, the contribution by the detector to the energy spread caused by the statistics of ion-pair formation is given by:

$$\text{FWHM(keV)} = 2.35\ \sqrt{E\varepsilon} \qquad (5)$$

For germanium and silicon, the value of ε is 2.9×10^{-3} and 3.6×10^{-3} keV/ion-pair, respectively. For gas counters, ε is approximately 30×10^{-3} keV/ion-pair and increases to about 500×10^{-3} keV/ion-pair for scintillation detectors. The spread in energy as calculated from eq. (5) with E = 100 keV yields 1.3 keV for germanium, 4.1 keV for a proportional counter, and 16.8 keV for a scintillation detector. In

actual practice, germanium detector contributions to resolution at an energy of 100 keV have been measured to be as low as 0.5 keV which is much smaller than that expected from Poisson statistics alone. The explanation for this discrepancy comes from a study originally made by Fano[29] and relates to the statistical treatment of the process of ion-pair formation in detectors. If one calculates, for example, the variance on the number of ion-pairs formed in a finite detector with the restriction that the energy loss has a fixed value (corresponding in practice to the photopeak energy), then a value is obtained which is two to three times smaller than that predicted by Poisson statistics without any restrictions. Therefore, a more accurate expression for the detector contribution to energy spread (FWHM) is $2.35\sqrt{\varepsilon FE}$, where F (Fano factor) is less than one.

Although semi-conductor detectors are capable of superior resolution, no mechanism exists for charge multiplication such as the multiplication process in proportional counters or the phototubes used with scintillation detectors. As a result, very small signals are generated which require a very low noise first amplification stage in order to utilize fully the resolution capability of semi-conductor detectors. In fact, the advent of semi-conductor radiation detectors has required the re-evaluation of all elements of a pulse height analysis system.[30,31]

B. Cooled FET Preamplifier

A typical high resolution spectrometer used for precise energy measurements consists of the following elements:

1. A high quality semi-conductor detector.
2. A low noise preamplifier.
3. A low noise mainline amplifier with pulse shaping flexibility for maximizing the signal to noise ratio.
4. A multichannel analyzer with good linearity and stability characteristics and a sufficient number of channels (>1000 for most applications).

The preamplifier noise is generally the limiting factor in obtaining high resolution. The lowest noise preamplifiers use a field effect transistor (FET) as the first amplifying element. At low energies (<100 keV), the contribution to the total energy spread from the best commercial FET preamplifiers is typically a factor of three or more than the detector contribution. The FET generally used is a 2N3823 manufactured by Texas Instruments, Inc. The noise performance of FET preamplifiers has been improved further[32-34] by using a selected 2N3823 in different first-stage configurations and cooling the FET to near LN temperatures. The noise figures obtained for these cryogenic preamplifiers are typically two to three times lower than the standard commercial FET preamplifiers having the same type FET. Thus, a commercial FET preamplifier was selected and modified for lower noise along the lines set forth by others.[34] The remainder of this section deals with the development of this cryogenic preamplifier and the associated Si(Li) and Ge(Li) spectrometers.

It will be useful to discuss, first, some general aspects of preamplifier circuits normally used with semi-conductor detectors.

Attention will be confined, for the most part, to the first amplifying stage since the signal to noise ratio (S/N) is essentially determined at that point. Two general types of preamplifier-circuit configurations are used with semi-conductor detectors.[35] These circuit configurations, shown in Fig. 2a and 2b, are designated as voltage sensitive and charge sensitive, respectively. The active input element can represent a vacuum tube or an FET for the purpose of this discussion. C_o and R_o represent the total input capacitance and resistance, respectively, including the detector capacitance and leakage resistance. In the voltage sensitive configuration, the output voltage is proportional to the input voltage. The advantages of this circuit are the possibility of a faster rise time and a slightly higher S/N than the charge sensitive circuit. The disadvantages are that the output signal height depends upon the detector capacitance (through C_o) and the pulse decay time depends upon the detector leakage resistance (through R_o). Therefore, any variation of these detector parameters will lead to unreliable operation. In contrast, the output voltage in the charge sensitive configuration is proportional to the charge introduced at the input of the preamplifier. Specifically, Q/C_f is the output voltage, where C_f is the feedback capacitance and is essentially independent of the detector capacitance over a broad range of operating conditions. As a result of the above considerations, the charge sensitive configuration is generally perferred and is the one used by most commercial manufacturers.

The commercial preamplifier which was selected for the cryogenic system used in this experiment was a Tennelec model TC-130 FET

preamplifier. The modifications which were made to the basic TC-130 circuit in order to reduce its noise contribution were based primarily on the work of Elad and Nakamura. Although these modifications are relatively straight-forward, the successful operation of the low-noise circuit with a semi-conductor detector places stringent requirements on certain properties of the detector. As a result, spectrometers such as these must usually be custom made. The typical sources of noise encountered in FET preamplifiers will be discussed next. The procedure for minimizing this noise and the requirements placed on the detector in the process will be outlined.

Fig. 3 is a schematic of a typical room-temperature FET pre-amplifier used with a cooled semi-conductor detector and will serve to illustrate the various sources of noise, as well as the basic operation of the FET first-stage. When radiation is absorbed in the detector, a quantity of charge is released which flows for a brief duration (depending on the collection time of the detector) and constitutes the input signal to the preamplifier in the form of a current pulse. The current pulse is integrated to approximate a step function whose decay time is determined by the product $R_G C_F$. The amplitude of the resulting voltage pulse is proportional to the energy deposited in the detector.* The gate resistor R_G is generally of the order of 10^9 ohms and serves the additional purpose of fixing the FET bias (gate-source voltage). The optimum FET bias for the highest S/N is near zero volts[36] and is determined in this type of

---

*The instantaneous amplitude of the current pulse is not proportional to the energy deposited in the detector; it is the total charge released or the integral of the current pulse which is proportional to the energy.

circuit by R_G which holds the gate lead near ground potential.

The sources of noise may be categorized as follows:

1. intrinsic S/N of the FET
2. thermal noise of R_G and R_L
3. dependence of S/N on input capacitance.

Selected FET's can give considerably better S/N than off-the-shelf units. Selected 2N3823's have been obtained from Texas Instruments (yields are typically 1 in 1000) under selection number SF3914, which are approximately 50% better than the average. An additional 30% improvement in the S/N can be obtained by cooling an FET to the optimum temperature. An expression for the noise contribution of the gate resistor has been given by Smith and Kline [32] in terms of an equivalent noise current and is proportional to T/R_G where T is the absolute temperature. This shows that large values of gate resistance result in low noise, a fact which has been verified experimentally in this laboratory using values for R_G which ranged from 10^8 to 10^{11} ohms. Thus, by using large values of gate resistance, one can expect to reduce the noise contribution of the preamplifier. A degradation in the S/N due to input capacitance occurs because the signal generated by the detector is inversely proportional to the input capacitance. Therefore, the noise contribution of a preamplifier is usually stated in terms of the noise at zero external capacitance and the slope of the noise vs input capacitance. In addition to the detector capacitance, the stray capacitance of the front-end components and associated wiring constitutes a source of noise. Therefore, the highest resolution is obtained by using a low capacitance detector and a short electrical connection from

the detector to the FET. The stray capacitance of the input connection can constitute a major fraction of the total input capacitance since typical values for detector capacitance are low, ranging from 2 to 50 picofarads.

The desire to minimize the sources of noise discussed above leads logically to the front-end configuration shown in Fig. 4d. This configuration uses a selected FET (selection #SF3914) which is placed inside the detector cryostat and cooled to the optimum temperature for the highest S/N. The optimum FET temperature is determined empirically and always occurs slightly above the temperature of LN. The thermal noise of resistors R_G and R_L, as well as their stray capacitance, has been eliminated. The stray capacitance of the remaining connections has been minimized by DC coupling the detector to the FET and mounting the two as close to each other as possible. DC coupling the detector requires that the detector be isolated from ground. The successful operation of this configuration requires that the reverse leakage current of the detector be very low in order that the FET be biased properly. In the DC coupled configuration, the FET bias is determined by the voltage drop across the gate-source junction and is developed by the detector leakage current and the gate-to-source DC impedance. Detector leakage currents range in value from 10^{-12} to 10^{-8} amperes and the gate-source resistance, in the absence of a gate resistor, is just the FET junction impedance which is approximately 10^{11} to 10^{13} ohms. Therefore, in order to maintain the optimum FET bias of near zero volts (usually less than 1 volt), the detector leakage current should be in the neighborhood of 10^{-11} amperes. Higher leakage current can be tolerated by shunting the gate-source junction with a resistor

of the appropriate value; however, this step increases the noise contribution of the preamplifier.

Three first-stage configurations, in addition to the standard TC-130 first stage, were studied. Schematics of these circuits are shown in Fig. 4a-d, and Table I summarizes the results of noise measurements for each. The noise contribution of the TC-130 for each front-end configuration was measured for zero external capacitance at room temperature, and with the FET cooled to the optimum temperature. The noise level in terms of an equivalent number of rms ion-pairs was calculated from:

$$N_{rms} = \frac{V_{noise} \times V_{in} \times C_T}{1.6 \times 10^{-19} \times V_{out}} \text{ ion pairs}$$

where:

V_{in} = peak amplitude (volts) of the pulse generator into 100 ohms impedance*,

V_{noise} = rms noise output (volts) of shaping amplifier with pulser disconnected,

V_{out} = peak amplitude (volts) at the output of the shaping amplifier,

C_T = test capacitance (farads),

1.6×10^{-19} = electronic charge in coulombs

The conversion from ion-pairs to keV (FWHM) is made with the following expression:

$$FWHM(keV) = 2.35\ N_{rms}\ \varepsilon$$

where:

$\varepsilon = 2.94 \times 10^{-3}$ keV/ion-pair for germanium and

$\varepsilon = 3.61 \times 10^{-3}$ keV/ion-pair for silicon.

---

*The TC-130 test input is terminated into 100 ohms.

A Berkeley Nucleonics Co. pulse generator, Model RP-1, was used to deposit charge on a 0.5 pF test capacitor at the preamplifier input and the shaping amplifier was a Tennelec TC-200. For all noise measurements, single differentiation was used with equal RC integrating and differentiating times constants of 3.2 μsec. V_{noise} was measured with a Hewlett-Packard 3400A rms voltmeter. The results of these noise measurements and the mechanical details of the cryogenic preamplifier are discussed in a recent publication.[37]

C. Ge(Li) and Si(Li) Spectrometers

Ge(Li) and Si(Li) spectrometers were constructed using the low noise preamplifier configuration of Fig. 4d. The Ge(Li) detector was a planar device, 3.5 cm^2 x 5 mm deep, purchased from RCA Ltd., Montreal, Canada. It was permanently encapsulated in a soft steel case 0.020 inch thick and could be easily transferred in and out of a cryostat without contaminating the detector surface. The leakage current of the detector was very low (less than 10^{-11} amperes at 800 volts bias) which permitted it to be DC coupled to the lowest noise preamplifier configuration (Fig. 4d). The silicon detector was 80 mm^2 x 3 mm deep and purchased from Technical Measurement Corporation as a selected detector, Model W80-3AA. The leakage current of this detector was also very low and measured to be less than 10^{-11} amperes at 400 volts bias. The capacitances of the silicon and germanium detectors were approximately 3 pF and 12 pF, respectively.

The DC coupled configuration requires that the detector bias be changed with care. When the detector bias is changed, the momentary variation of voltage is transferred by the detector capacitance to the

gate lead of the FET. This voltage surge can be either positive or negative depending on whether the bias is positive or negative and the change is increasing or decreasing. The effects of a voltage surge at the input can be understood in terms of the diode nature of the FET gate-source junction in which the source is identified with the cathode of a diode structure.

The effects of a bias change for the TC-130 preamplifier in the DC coupled configuration are manifested in two distinct ways. If the voltage surge is positive, the FET can discharge rapidly with no harmful effect even though parasitic oscillations are observed while a change in bias is occurring. If the voltage surge is negative, charge rapidly builds up until the FET is biased off, with the result that the output saturates and the circuit becomes paralyzed. The accumulated charge can remain for hours due to the long RC times involved unless the bias is changed back to the value for which saturation occurred. The net result is that for a detector which is used in the positive high voltage configuration (PHVC):

1. Detector high voltage can be increased at a normal rate. Momentary oscillation will be observed on an oscilloscope while the bias is being increased.
2. When the detector bias is decreased, it must be turned down very slowly while observing the output noise on an oscilloscope. The band of noise should increase slowly due to removal of the detector bias and not saturate abruptly indicating that bias is being removed too rapidly.

The opposite is true for a detector which is used in the negative high voltage configuration (NHVC):

1. The bias must be increased slowly while observing that the noise decreases slowly and does not saturate abruptly.
2. The detector bias can be decreased at a normal rate and momentary oscillations will occur while the bias is being changed.

For reasons which will be discussed shortly, the silicon detector was used in the NHVC (Fig. 5) and the germanium detector was used in the PHVC (Fig. 6). The PHVC is generally preferred because it has the best count rate capability. A count rate problem is encountered due to the very high input impedance of the FET (10^{10} - 10^{12} ohms) which allows charge to build up rapidly and to change the FET bias to a value which is far from optimum. As stated earlier, the optimum FET bias for low noise is near zero volts and usually less than one volt. When the positive high voltage configuration is used, the FET bias is positive and charge pile-up tends to make it more positive. As the instantaneous FET bias approaches about +0.6 volts due to pulse pile-up, the input impedance begins to decrease, which allows the accumulated charge to discharge quickly. Thus, for the circuit of Fig. 6, the effects of charge pile-up which accompanies high count rates are minimized. The inverse argument holds for the NHVC. Since this count rate effect results from charge pile-up, it also depends on the energy deposited in the detector and will, therefore, be a more serious problem for germanium detectors than for the smaller and less efficient silicon detectors currently available.

The count rate dependence for the Ge(Li) spectrometer was studied for the positive and negative high voltage configurations with a Co^{60} source. The detector bias for both cases was 700 volts. For the NHVC, the preamplifier output saturated for a total rate in the detector of about 2500 counts/sec. For the PHVC, the count rate dependence was studied at total rates as high as 10^5 counts/sec and no saturation was observed. The resolution (FWHM) of the 1.33 meV line was measured for the latter configuration at total rates in the detector ranging from 500 to 1.3×10^4 counts/sec. These results are listed in Table II. The mainline amplifier for the spectrometer was a Tennelec Model TC-200 with precision resistors for pole-zero cancellation* installed in the differentiating network. Single differentiation was used with equal integrating and differentiating time constants of 1.6 μsec which gave the best resolution at moderately high count rates. The pole-zero cancellation was very effective in minimizing the line broadening due to pulse pile-up in the TC-200 and also in reducing shifts in the peak amplitude at high counting rates. Most of the observed peak shift occurred for total rates in the range of 8000 to 1.3×10^4 counts/sec. Over the total range of 500 to 1.3×10^4 counts/sec, the peak shift was less than 0.15%. The resolution without pole-zero cancellation was about 10 keV at a rate of 8000 counts/sec.

At rates of less than 1000 counts/sec, the optimum time

---

*Pole-zero cancellation is used to minimize the pulse undershoot which is caused by differentiation, and thereby improves the count rate performance. This modification consists of placing a precision resistor R_{pz} in parallel with the capacitance of the RC differentiating network such that $R_{pz}C$ is equal to the decay time of the preamplifier.

constants for best resolution were found to be 3.2 μsec. Fig. 7 is a spectrum of Co^{60} γ-rays taken under these conditions. The 1.33 MeV line was measured with a resolution of 2.08 keV (FWHM). The resolution at low energies is illustrated by the Co^{57} γ-ray spectrum shown in Fig. 8. The FWHM of the 122 keV line measured to be 1.02 keV. The resolution at low energies was limited by the noise of the preamplifier first stage. A major fraction of this noise resulted from mechanical vibrations caused by the bubbling of LN in the detector cryostat. This noise was predominantly low frequency (about 3kHz) and is attributed to the detector encapsulation since the same effect has not been observed for bare silicon and germanium detectors, of comparable resolution, mounted with the same front-end. This source of noise could be temporarily suppressed by removing the LN, and under these conditions the 122 keV line was measured with 0.8 keV resolution FWHM. The noise of the preamplifier at zero external capacitance has been measured to be 0.29 keV (germanium equivalent) with a slope of about 0.034 keV/pF.

The Si(Li) detector was mounted in the NHVC. This configuration was used because the original development work on the cryogenic preamplifier was done with the Si(Li) detector using negative high voltage and resulted in a very high resolution system with no serious count rate problems such as those experienced in the Ge(Li) spectrometer. As a result, no subsequent attempt was made to use the Si(Li) detector in the PHVC, although the system should work satisfactorily in this configuration and result in a generally better spectrometer.

The noise contribution of the preamplifier used with the Si(Li) detector was measured to be 0.39 keV (silicon equivalent) at zero external capacitance with a slope of about 0.04 keV/pF. The bubbling

of LN did not constitute a major source of noise for the Si(Li) spectrometer although the spectrometer was sensitive to external noise and vibrations. The sensitive nature of the spectrometer can be demonstrated by expressing the resolution at low energies in terms of an equivalent number of rms charges injected at the input of the preamplifier. Since the average energy required to produce an electron-hole pair in silicon is 3.6 eV, an rms noise of one electron-hole pair is equivalent to a FWHM contribution of 8.5 eV. Thus a resolution of 0.5 keV FWHM is equivalent to a total of 59 rms noise charges contributed by all elements of the Si(Li) spectrometer.

The resolution of the Si(Li) spectrometer is illustrated in Fig. 9 and 10. The 26.36 keV line of Am^{241} (Fig. 9) was measured with 0.54 keV resolution. Similarly, the 6.4 keV X-ray of Co^{57} (Fig. 10) was measured with 0.46 keV resolution. Single differentiation was used, and the optimum time constants for lowest noise were found to be 6.4 μsec for the differentiator and 3.2 μsec for the integrator.

IV. EXPERIMENTAL METHOD

Most of the data for this experiment was collected during a run at the 450 MeV synchrocyclotron located at Carnegie-Mellon University, Pittsburgh, Pennsylvania. Some additional data on carbon were obtained at the 600 MeV machine of the Space Radiations Effects Laboratory (SREL) in Newport News, Virginia.

A. General Procedure

A general outline of the experimental method will be given first, and then a detailed discussion of the geometry, counters, beam characteristics, circuitry, and targets will be presented.

Pi-mesic atoms were formed by stopping a beam of negative pions in a selection of low Z targets and the resulting pionic X-rays were detected with either a high-resolution Si(Li) or a Ge(Li) spectrometer. The 75-MeV pion beam from the CMU machine was focused by a coaxial-type channel[38] and brought into the counter array through a 6" x 6" aperture in a two-foot thick concrete shielding wall. Pions were momentum-selected by a bending magnet which was placed between the counter array and the shielding wall.

The counter array, used to define pion-stops and detect pionic X-ray events, is shown in Fig. 11. An energy spectrum of events occurring in the detector was stored in a 1600-channel analyzer (Victoreen, SCIPP) which was gated to accept pulses when a coincidence was made between the detector signal and the pion-stop signal. A

pion-stop was recorded as a $12\bar{C}3\bar{4}$ coincidence and a fast logic signal corresponding to an event in the detector was generated by the "cross-over" timing technique.

Muonic X-rays were observed simultaneously with pionic X-rays because of muon contamination in the beam. Although the higher muonic transitions (3p-1s, 4p-1s, 5p-1s) constituted a source of background under each 2p-1s pionic X-ray peak, the 2p-1s muonic lines gave a reliable measure of instrumental resolution during the course of each pion run. Radioactive sources were used to determine the gain of the spectrometers and, in addition, provided an independent check of instrumental resolution. Muonic X-rays for each target were also measured in separate runs with the beam selected for maximum muon intensity. These runs were taken in order to determine the energy and relative intensity of muonic transitions so that muon contamination peaks could be accurately accounted for in a background subtraction analysis.

B. Geometry, Counters, and Beam Characteristics

The Ge(Li) and Si(Li) detectors were used in side geometry in order to keep the count rate low, since resolution begins to deteriorate at high rates (>2000 counts/sec). The detectors were placed on the low-momentum side of the counter array because the signal-to-background ratio was measured to be higher on this side. As shown in Fig. 11, each detector was shielded from the beam by lead bricks placed adjacent to it and the counter array. The target-defining counter and targets were positioned with their centers on axis with

the beam and with their faces at an angle of about 45° to the beam direction.

Counters 1, 2, 3, and 4 were plastic scintillation counters constructed at William and Mary and consisted of commercial scintillant (Pilot Chemical Co.) optically coupled by means of Lucite light pipes to Amperex 56 AVP photomultiplier tubes. The dimensions of these scintillants were: for 1 and 2, 6" X 6" X 1/4"; for 3, 5" X 5" X 1/16"; and for 4, 10" X 10" X 1/8". The target-defining counter (3) was the most serious source of carbon background (in the form of carbon muonic and pionic X-ray lines) since a pion-stop signature ($12\bar{C}3\bar{4}$) could be generated by a pion stopping in this counter instead of the target. Therefore the scintillant of 3 was chosen to be only 1/16" thick and, in addition, the light-tight wrapping was made of thin (5 mil) black plastic. Since 4 was used as an anti-coincidence counter, it was constructed much larger than the others. The efficiency of this counter measured to be 98% in the anti-coincidence mode. A $\check{C}$erenkov counter was used to identify high-energy electrons whose bremsstrahlung was a potential source of background. The signal from this counter was used in the anti-coincidence mode in order to prevent storage of this background. The two-inch thick $\check{C}$erenkov counter contained water as a radiator and was constructed from a square Lucite frame with entrance windows made of aluminized mylar 5 mil thick. The sensitive volume of the $\check{C}$erenkov counter was viewed by two RCA 8575 photomultiplier tubes. The efficiency of this counter for discriminating against electrons was approximately 50%.

Each semiconductor detector was used with a different group of targets in order to achieve optimum efficiency and resolution. The

Si(Li) detector was used to measure pionic 2p-1s transitions in the lithium ($E_{K_\alpha} \simeq 24$ keV) and beryllium ($E_{K_\alpha} \simeq 43$ keV) targets and the Ge(Li) detector was used for the boron ($E_{K_\alpha} \simeq 65$ keV) and carbon ($E_{K_\alpha} \simeq 93$ keV) targets. The Si(Li) and Ge(Li) detector sizes were 0.8 cm^2 x 3 mm and 3.5 cm^2 x 5 mm, respectively.

The beam-associated random background was low as a result of the "beam pulse stretching" technique [39] employed at the CMU synchro-cyclotron. About 70% of the total beam was contained in the stretched beam pulse, which had a spill time of approximately 3 msec. The structure of the beam pulse was uniform except for a narrow prompt spike. All logic circuitry was gated off for the duration of this prompt spike in order to prevent the random background which accompanies high instantaneous rates from being stored. The coaxial-focusing channel of the CMU machine increased the beam intensity, but also resulted in high muon contamination. The 600 MeV machine at SREL, capable of inherently higher beam intensities, did not have a channel installed at the time of this experiment and produced a pion beam of low muon contamination. However, the pulse stretching at SREL was accomplished by means of a vibrating target, resulting in a poorer stretched beam than at CMU and, presumably, was a cause of the higher background level observed at SREL. The muon contaminations were approximately 20% and 2% for the CMU and SREL beams, respectively, and the signal-to-background at CMU was approximately a factor of two higher than at SREL.

Typical pion stopping rates ($12\bar{C}34\bar{}$) in approximately 1 lb. of carbon were 2 x 10^4/sec at CMU and 5 x 10^4/sec at SREL. Polyethylene

absorber was used to maximize pion stops in each target. Differential range curves for the CMU and SREL pion beams are shown in Fig. 12 and 13, respectively.

C. Timing Logic

A block diagram of the circuitry used in this experiment is shown in Fig. 14. The main function of this circuitry was to generate a gate which allowed the analyzer to accept pulses from the detector only when a coincidence occurred between a pion-stop signal and a detector signal.

In order to generate an appropriate analyzer gating pulse, a "tight" coincidence was required between the "fast" pion-stop signal and the "slow" detector signal. The pion-stop signal ($12\bar{C}3\bar{4}$) was generated from individual pulses which were fast rising (5 nsec) and narrow (10 nsec), in contrast to the detector signal at the output of the preamplifier which was slow, rising in about 100 nsec and having a decay time of 50 μsec. A fast timing signal was generated from the slow detector pulse by the "cross-over" timing technique. In this technique, the preamplifier signal is shaped by a delay-line amplifier which generates a bi-polar pulse whose zero-crossing point is a stable time reference suitable for triggering a fast discriminator. In this manner, a timing signal corresponding to an event in the detector was generated in SCA 1 and constituted the "slow" input to the "fast-slow" coincidence circuit, COINC 4. The "fast" input represented a pion-stop signature ($12\bar{C}3\bar{4}$) which was generated in COINC 1. The output of COINC 4 triggered a delay-gate generator which provided a signal of the appropriate width and delay for gating the analyzer.

That part of the circuitry which includes the time-to-amplitude converter (TAC) and timing-analyzer (400 channels) was used initially to bring the "fast" and "slow" pulses into coincidence and also served to monitor the timing resolution throughout the experiment. The "fast" and "slow" timing signals constituted the START and STOP inputs to the TAC (EGG, Model TH200A) which generated an analog output signal proportional in amplitude to the time difference between the START and STOP signals. An additional signal, VALID STOP OUT, was generated internally whenever a stop input was accepted by the TAC. The analog output of the TAC was stored in the memory of the timing analyzer, with time-correlated events accumulating as a peak and random events as "flat" background.

The routing logic prescribed the manner in which these random and time-correlated events were stored and permitted a simple and direct determination of the time difference between correlated "fast" and "slow" inputs to COINC 4. Accordingly, all timing events were stored subject to one of the following requirements:

(1) no coincidence occurred between the router inputs. The analyzer signal was then stored in the first 200 channels, or

(2) a coincidence occurred between router inputs. The analyzer signal was then stored in the second 200 channels.

If the correlated "fast" and "slow" timing signals into COINC 4 were initially out of time by T, clearly requirement (2) could only be satisfied by <u>random</u> coincidences made in COINC 4. These random coincidences corresponded to a definite range of time intervals between

the inputs to the TAC; as a result, a trough (center at channel X) appeared at a time T away from the timing peak and its inverted image at channel 200 + X (Fig. 15a). The width of this trough was determined by the resolving time of COINC 4. When the fast-slow signals were brought into time at COINC 4, requirement (2) could be satisfied by time-correlated events. The trough then appeared at the channel location of the timing peak (X + T) and the peak itself was stored in channel 200 + X + T (Fig. 15b). The pion-stop signal and its correlated detector signal were then in time coincidence. The timing resolution, as determined from the base of the timing peak, was approximately 300 nsec for this experiment, with the largest contribution resulting from the time-jitter of the "slow" signal.

D. Resolution Optimization and Gain Calibration.

In order to achieve the highest resolution under experimental conditions, the following effects were considered:

1. total count rate in the detector
2. extraneous noise pick-up
3. system drifts.

The primary source of the degradation in resolution with increasing count rate is the main amplifier and is due to the random overlap of one pulse with the undershoot of the preceding pulse. This undershoot can be minimized by selecting "short" time constants in the amplifier shaping network and by using pole-zero cancellation (section III-C). "Long" time constants are, however, typically required for inherently high S/N and, therefore, a compromise was made in the choice

of RC times. In addition to these electronics considerations, count rates were kept low by using the detectors in side geometry. For the Si(Li) spectrometer, the optimum time constants for best resolution were 6.4 μsec (differentiator) and 3.2 μsec (integrator); for the Ge(Li) spectrometer equal RC time constants of 1.6 μsec were used.

The usual precautions were taken for eliminating electrical noise pick-up in the system:

1. all electronics in the detector signal chain were powered from a common-ground outlet.
2. signal-carrying cables were located such that noise induced from other cables and components was minimized.

Care was also taken to keep sources of mechanical vibrations out of the immediate experimental area.

System drifts were minimized during Ge(Li) runs by the use of a digital gain stabilizer (Canberra, Model 1495) which stabilized on a reference peak generated by a radioactive source. Optimum performance of the gain stabilizer occurs when the reference peak is located at the upper end of the energy spectrum since gain changes are more easily detected in this range. However, due to the low-energy background associated with such a reference line, a source was selected whose highest energy was below all experimental lines of interest. For the Ge(Li) spectrometer, the 60 keV line of Am^{241} was used as a reference peak. The experimental lines measured with this detector occurred in an energy range between 52 keV and 93 keV. For the Si(Li) detector, experimental lines were observed between 6 keV and 43 keV and precluded the use of a stabilizer. Typical drifts observed during the course of

the experiment were approximately 0.3 channel/day for the Ge(Li) system (gain = 0.192 keV/ch) and 0.5 channel/day for the Si(Li) system (gain= 0.076 keV/ch). Individual runs for a given target typically consisted of four and, in some cases, eight hours of data accumulation.

The resolution of the Si(Li) spectrometer, as measured from the muonic 2p-1s line (33 keV) of Be^9, was 0.62 keV FWHM. The Ge(Li) gave a resolution of 1.1 keV FWHM for the muonic 2p-1s line (75 keV) of C^{12}. These figures represent less than 10% degradation in resolution as measured under laboratory-controlled conditions with radioactive sources.

Radioactive sources were used to determine the gain of the spectrometers. Calibration spectra, under beam conditions and with no pion-stop requirement, were taken before and after each pionic run.

The following lines[40,41] of Am^{241} and Ta^{182} were used for calibrating the Si(Li) and Ge(Li) spectrometers:

Si(Li), Gain 0.076 keV/ch		Ge(Li), Gain 0.192 keV/ch	
Am^{241}:	59.568 ± 0.017 keV	Am^{241}:	59.568 ± 0.017 keV
Am^{241}:	26.364 ± 0.017 keV	Ta^{182}:	67.751 ± 0.001 keV
		Ta^{182}:	84.693 ± 0.001 keV
		Ta^{182}:	100.107 ± 0.001 keV

E. Targets

Pertinent information on the targets used in this experiment is given below. The target holders consisted of square plastic frames with 5 mil mylar windows which covered the target area. The beryllium and carbon targets required no holder.

Target	Mass	Purity	Size	Form
Li^6 (separated)	124.5 gms	total lithium = 99.9 % of this, Li^6 = 95.63% Li^7 = 4.37%	5½"X5½"X1"	sheets
Li^7 (natural)	200 gms	total lithium = 99.9 % of this, Li^7 = 92.58% Li^6 = 7.42%	7"X7"X1"	foil
Be^9 (natural)	500 gms	total beryllium=98.0 % of this, Be^9 =100.0%	5"X5"X0.7" (own holder)	sheets (3)
B^{10} (separated)	100 gms	total boron = 93.16% of this, B^{10} = 92.67% B^{11} = 7.33%	6"X6"X3/8"	granules
B^{11} (natural)	454 gms	total boron = 99.8 % of this, B^{11} = 80.22% B^{10} = 19.78%	7"X7"X3/4"	granules
C^{12} (natural)	440 gms	total carbon = 99.8 % of this, C^{12}= 98.89% C^{13}= 1.11%	6"X6"X1/2" (own holder)	plates

The separated Li^6 and B^{10} targets were obtained from Oak Ridge National Laboratory; the Li^7 and B^{11} targets from the United Mineral and Chemical Company; the Be^9 sheets from the Brush Beryllium Company; and the C^{12} plates from the Products Division of Union Carbide.

V. DATA ANALYSIS

The natural line width associated with the 2p-1s transition in a pi-mesic atom is a direct measure of the nuclear absorption rate of pions from the 1s atomic level and is the physical quantity of interest in this experiment. As pointed out in the introduction, the natural line shape for the 2p-1s energy distribution can be described by a Lorentzian function:

$$L(E) = \frac{A}{(E-E_{2p-1s})^2 + (\omega_{abs}\hbar/2)^2} ,$$

where $\omega_{abs}\hbar = \Gamma_{nat}$ = FWHM

and ω_{abs} = nuclear absorption rate of pions from 1s level.

Experimentally, this Lorentzian distribution of energies is measured with a spectrometer which imposes its own characteristic line shape since the system resolution is not negligible compared with natural widths. Thus, the observed 2p-1s pionic lines represent the combined effects of spectrometer and natural line shapes. In addition, the nature of the experimental background also affects the observed line shape. The accurate unfolding of Γ_{nat} from raw experimental data, then, required that the complications introduced by the spectrometer line shape and background be understood and taken into proper account. These considerations determined the procedure used in the data analysis. The specific methods used in analyzing the data to obtain Γ_{nat} for each

target will be discussed in the remaining sections. In section A, a description is given of the combined effect of the natural line shape and the spectrometer line shape; in section B, the methods used for obtaining Γ_{nat} from experimental data are presented; and in section C, the error analysis for each target, as well as the final results for Γ_{nat}, is given.

A. Line Shapes and Width Relations

In the absence of experimental background, the observed line shape can be described in terms of the combined effect of three independent processes:

1. photon emission corresponding to 2p-1s pionic transitions,
2. photon detection and subsequent conversion to charge,
3. signal amplification and processing for final storage of data.

A probability density function can be associated with each of the above processes and, then, the methods of mathematical statistics [42] used to determine the theoretical line shape. Although the mathematical results which will be obtained here have been derived previously for analogous problems in physics, this discussion will serve to illustrate their validity for this specific line shape problem.

A probability density function, $f(x)$, defines the probability that a random variable $\underline{x}$ will assume a value in the interval $x_2 - x_1$ according to the following relation:

$$\int_{x_1}^{x_2} f(x)\,dx = \text{probability that } \underline{x} \text{ assumes a value between } x_2 \text{ and } x_1.$$

A random variable is defined as a number associated with the outcome of a "chance experiment." Thus, the Lorentzian function L(E) given above is the probability density function describing the energy distribution of individual photons which are emitted in a pionic 2p-1s transition. The energy of an arbitrary photon represents the random variable and the random time emission of a photon constitutes the "chance experiment." A similar identification can be made for the effects of the detector and electronics on the total line shape. Once the proper random variable has been chosen for each process affecting the measured line shape and a corresponding probability density function determined, the general rules of mathematical statistics can be used to give directly the analytical form expected for the observed line shape. Accordingly, the processes affecting the line shape, the appropriate random variables, and the corresponding probability density functions are given below.

Process	Random Variable	Probability Density Function
Photon emission from 2p-1s pionic transitions.	E_{ph}: photon energy for given 2p-1s transition.	Lorentzian: $L(E_{ph},\Gamma_{nat})$
Conversion of photon energy to charge.	ΔE_{det}: deviation from mean energy in the conversion process.	Gaussian: $G(\Delta E_{det},\Gamma_{det})$
Random effect of noise on amplitude of energy signal.	ΔE_{el}: deviation from mean amplitude of the energy signal.	Gaussian: $G(\Delta E_{el},\Gamma_{el})$

The random variable representing the observed energy distribution can now be written as the sum of three statistically independent random variables:

$$\underline{E_{observed}} = \underline{E_{ph}} + \underline{\Delta E_{det}} + \underline{\Delta E_{el}}$$

The total line shape is described by the probability density function associated with the random variable $\underline{E_{observed}}$. The determination of this density function now becomes a standard statistics problem whose solution is outlined, for example, in reference 42. Specifically, if $\underline{x_1}$ and $\underline{x_2}$ are statistically independent random variables described by probability density functions $f_1(x_1)$ and $f_2(x_2)$, respectively, then, for $\underline{Y} = \underline{x_1} + \underline{x_2}$, one obtains:

$$f(Y) = \int f_1(Y-x_2)\ f_2(x_2)\ dx_2$$

or

$$f(Y) = \int f_1(x_1)\ f_2(Y-x_1)\ dx_1$$

where $f(Y)$ is the probability density function describing $\underline{Y}$. Thus, in order to obtain the line shape due to the electronics and detector (i.e., spectrometer line shape), one has to evaluate the convolution integral of two Gaussians:

$$f(Y) = \frac{1}{\sigma_1\sigma_2 2\pi} \int e^{-(Y-x_2)^2/2\sigma_1^2} \cdot e^{-x_2^2/2\sigma_2^2} \cdot dx_2 \ ,$$

where $\sigma = \frac{\Gamma}{2.35}$

This integration is done in Appendix A and yields:

$$f(Y) = \frac{e^{-Y^2/2(\sigma_1^2 + \sigma_2^2)}}{(\sigma_1^2 + \sigma_2^2)^{1/2}\sqrt{2\pi}}$$

This is the well-known result that two Gaussians "fold" together to give another Gaussian whose width is quadratically related to the individual widths:

$$\Gamma_{tot}^2 = \Gamma_1^2 + \Gamma_2^2$$

For contrast, the convolution integral for two Lorentzian functions (evaluated in Appendix B) results in a Lorentzian function whose total width is related linearly to the separate widths:

$$\Gamma_{tot} = \Gamma_1 + \Gamma_2 \quad .$$

The expected energy distribution for pionic 2p-1s X-rays required the evaluation of a convolution integral for a Gaussian and Lorentzian function:

$$f(x) = \int L(Y)G(x-Y)dY$$

Although this integral, known as the Voigt integral, cannot be evaluated in closed form, its properties have been studied extensively.[43] A recent tabulation of Voigt profiles, based on numerical integration techniques, has been given by Davies and Vaughan[44] for a wide range of Gaussian to Lorentzian ratios and for which an accuracy of one part in 10^4 is claimed. This table of Voigt profiles was used to fit experimental 2p-1s pionic lines. A detailed discussion of the fitting procedure is presented next.

B. Natural Line Width Analysis

Pionic 2p-1s data from all the targets, except the lithium isotopes, were analyzed by the same general method in order to obtain Γ_{nat}. The analysis of the lithium data will be discussed separately after the general method is described.

1. General Method: Be^9, B^{10}, B^{11}, and C^{12} Analysis

In the general method, Γ_{nat} was obtained from each run by fitting a Voigt profile to the pionic 2p-1s data after the subtraction of muonic background lines. Random background could be represented by a simple function (Mx + I; M = slope, I = intercept) and was included as part of the Voigt fit. The muonic background subtraction analysis will be described first and then the Voigt fitting procedure for obtaining Γ_{nat} will be presented. All computations and curve fitting for the data analysis were done on an IBM 360-Model 50 computer.

a. Muonic Background Subtraction

Muonic 3p-1s, 4p-1s and 5p-1s peaks occurred in the energy range used for the analysis of the pionic 2p-1s peak for each target. Gaussian curves of the appropriate width, center, and amplitude were generated to represent the muon background lines for each run and were subtracted from the experimental data. The Gaussian parameters were determined from an analysis of the corresponding muonic lines in separate muon runs and by normalizing the results to each pion run. The $2\bar{p}$-1s muonic line was uncontaminated in both muon and pion

runs and was used as the reference peak in the normalization. The specific background subtraction analysis proceeded in the following manner:

1) Muonic lines from pion and muon runs were fit by a least squares technique to the function:

$$Y(x) = A\, e^{-(x - \bar{x})^2/2\sigma^2} + Mx + I$$

where: x = channel number

$Y(x)$ = counts in channel x

A = amplitude

$\bar{x}$ = center channel of peak

Γ = 2.35σ (FWHM in channels)

$Mx + I$ = linear background term

2) The analysis of muonic lines from muon runs permitted relative intensities and center channel differences to be determined; i.e.,

$$\text{relative intensity: } R_i \equiv \frac{A_i(\mu \text{ run})}{A_1(\mu \text{ run})},$$

$$\text{center channel difference: } \Delta x_i = \bar{x}_i - \bar{x}_1,$$

where i refers to the 3p-1s, 4p-1s, or 5p-1s muonic transitions, and $\bar{x}_1$ and A_1 refer to the 2p-1s transition. The ratio of the amplitudes alone was used to determine the relative intensity since the widths were essentially constant in the energy range from $E_{2p\text{-}1s}$ to $E_{5p\text{-}1s}$.

3) The analysis of the 2p-1s muonic lines from the pion runs gave amplitudes and centers from which 3p-1s, 4p-1s, or

5p-1s peaks could be generated in the form of Gaussian curves; i.e., with

$$\bar{x}_i\ (\pi\ \text{run}) = \bar{x}_1\ (\pi\ \text{run}) + \Delta x_i \text{ and}$$

$$A_i\ (\pi\ \text{run}) = A_1\ (\pi\ \text{run}) R_i, \text{ the functions}$$

$$Y_i(x) = A_i(\pi\ \text{run})\ e^{-(x - \bar{x}_i(\pi\ \text{run}))^2/2\sigma^2} \text{ were}$$

generated. The width of the muonic 2p-1s line in the muon run for each target was used to determine σ.

4) The value of the generated Gaussian function at each channel was subtracted from the pionic 2p-1s data.

The muonic transition energies and relative intensities are listed in Table III.

b. Voigt Profile Analysis

As pointed out in section V-A, a Voigt profile cannot be represented in closed form by a simple analytic function. This fact precluded a usual least squares fitting procedure. In order to make a Voigt curve fit to the 2p-1s pionic data, a computer program was devised which used the family of Voigt profiles tabulated by Davies and Vaughan[44] to perform a "search" and select the Voigt curve which best fit the data. Table IV is the Voigt profile tabulation given by Davies and Vaughan. The pertinent columns for this analysis are 3, 4, and 8 through 22. Columns 8 through 22 and the corresponding 27 rows define a family of 27 Voigt profiles in which the ratio of Gaussian width (FWHM) to total width (FWHM) ranges from 0.083 to 0.939. This ratio is

called the Gaussian fraction (G.F.) and is tabulated in column 4. Similarly, the Lorentzian fraction (L.F.) is listed in column 3 and is the ratio of the Lorentzian width (FWHM) to the total width. This table of Voigt profiles is given in terms of relative quantities and requires values for the amplitude and total width in order to have absolute meaning. For example, the argument of a given profile is given as a fraction of the total width. Each fraction, then, represents two points on the abscissa which are symmetric about the center of the profile. The value of a given profile along the ordinate is given as a fraction of its amplitude and ranges from 0.01 to 0.95. A column corresponding to 0.5 is not listed since, for all profiles, the fraction of the total width at one-half of the amplitude is unity. From the previous description, it becomes clear that a given Voigt profile could correspond to many Voigt curves, with each curve having different Gaussian, Lorentzian and total widths, but with the restriction that the G.F. (or L.F.) is the same for all curves. Thus, the term Voigt profile will refer only to the relative quantities given in Table IV and Voigt curve will refer to a specific curve generated from Table IV for a given value of amplitude and width.

The range of profiles (defined by extreme values of G.F. and L.F.) given in Table IV was sufficient for the widths involved in this experiment but the profile density, or number of profiles per change in L.F. (or G.F.), was too low. The profile density should be high enough such that the change in the Lorentzian width between any two profiles with the same total width is negligible compared with the error introduced by experimental statistics and background. In order to satisfy

this criterion, the number of profiles was increased by interpolation between rows. Thus, the number of profiles, and the corresponding number of values for G.F. and L.F. were increased from 27 to 1000. The interpolation program was an internal subroutine written by IBM and had a convergence criterion of 0.001. In order to use the table of Voigt profiles for a point-by-point comparison to 2p-1s pionic peaks, several further modifications were required. From Table IV, a Voigt curve is defined by only 31 points and in such a manner that makes a point-by-point comparison with experimental data difficult. Therefore, the interpolation program was used as a part of the main program to interpolate between the 31 points and give the value of the Voigt curve at any arbitrary point. In addition, a subroutine was also written which ordered the one-to-one correspondence between the value of a Voigt curve and its argument into a monotonic sequence from low channels to high channels. Finally, a linear term (Mx + I), whose two parameters were variable, was added in order to take the random background into account for each run.

Before a final fitting procedure was selected, six Voigt profiles were generated in order to study the behavior of the Voigt parameters. The parameters of these profiles were chosen to correspond, approximately, to those of the observed line shapes for each target. Each of these Voigt curves was analyzed by a least squares fit to the following functions:

$$L(x) = \frac{A_L}{(x-\bar{x}_L)^2 + (\Gamma_L/2)^2} + M_L x + I_L$$

$$G(x) = A_G\, e^{-(x-\bar{x}_G)^2/2\sigma_G{}^2} + M_G x + I_G\ , \quad \Gamma_G = 2.35\sigma_G$$

In all cases, the following relations were observed between the true Voigt parameters and those parameters as determined by a best fit to the Gaussian and Lorentzian functions.

1) $\bar{x}_V = \bar{x}_L = \bar{x}_G$, to within ± 0.05 channel

2) $\Gamma_L < \Gamma_V < \Gamma_G$

3) $A_G < A_V < A_L$

4) $|M_L| < |M_V| < |M_G|$

5) $I_L < I_V < I_G$

The values of all true Voigt parameters were systematically within the limits determined by the Gaussian and Lorentzian fits. Moreover, as the G.F. or L.F. became large, the parameters as determined by the Gaussian or Lorentzian fit were, respectively, closer to the true Voigt parameters. This behavior provided a convenient method of determining the ranges for the variable parameters in the Voigt search program. Thus, pionic 2p-1s peaks from each run were analyzed by a least squares fit to Gaussian and Lorentzian functions in order to establish reasonable limits on the total width, amplitude, center, slope, and intercept.

There were several ways to implement a search program for selecting the best Voigt fit to experimental data, depending on which parameters were free and which were held fixed. With a linear term $(Mx + I)$ added to the table of Voigt profiles, there are a total of 7 parameters and 2 equations of contraint which exist to specify the family of Voigt curves used in the search:

A = amplitude

$\bar{x}$ = center

Γ_V = Voigt width, FWHM

Γ_{instr} = width, FWHM, of Gaussian component (spectrometer resolution)

Γ_{nat} = width, FWHM, of Lorentzian component (natural line width)

M = slope of background

I = intercept, and the

equations of constraint G.F. = $\frac{\Gamma_{instr}}{\Gamma_V}$ and L.F. = $\frac{\Gamma_{nat}}{\Gamma_V}$.

For a given profile (definite G.F. or L.F.), there are only 5 independent parameters, the other two parameters being determined by the equations of constraint; i.e., A, $\bar{x}$, M, I, Γ_V or Γ_{nat} or Γ_{instr}. The instrumental line width, Γ_{instr}, was taken as a constant for each run since an independent experimental measurement of spectrometer resolution was available. The muonic 2p-1s background line in each pion run accumulated simultaneously with the pionic 2p-1s peak and, therefore, gave a reliable measurement of Γ_{instr} during each run. A fixed Γ_{instr} introduced an additional constraint since it specified Γ_{nat} and Γ_V for each profile. Therefore, the Voigt fitting procedure was selected according to the following requirements:

1) parameters A, $\bar{x}$, M, and I were free to vary

2) Γ_{instr} was chosen constant for each pion run

3) G.F. $\equiv \frac{\Gamma_{instr}}{\Gamma_V}$, L.F. $\equiv \frac{\Gamma_{nat}}{\Gamma_V}$. Therefore, because of requirement 2), each profile had fixed values for Γ_V and Γ_{nat}.

4) Gaussian and Lorentzian fits should place limits on the values of A, $\bar{x}$, M, I, and Γ_V.

For each run, the constant value of Γ_{instr} and the limits placed on Γ_V by the Gaussian and Lorentzian fits were used to determine the range of G.F. (and, hence the family of Voigt profiles) to be used in the search. For each profile within this range, the parameters A, $\bar{x}$, M, and I were varied in discrete steps over their ranges as defined by the Gaussian and Lorentzian fits until a best Voigt fit was obtained. A chi-squared test was used as the best-fit criterion for each Voigt curve within the search, with

$$\chi^2 = \sum_{i=1}^{n} \left(\frac{Y_i(\text{data}) - Y_i(\text{Voigt})}{\sigma_i(\text{data})} \right)^2,$$

where n = channel range in fit,

$\sigma_i(\text{data}) = \sqrt{Y_i(\text{data})}$

$Y_i(\text{data})$ = number of counts in i^{th} channel.

The quantity χ^2 was computed for each Voigt curve generated in the fit and the value of Γ_{nat} (as well as Γ_V) corresponding to the minimum χ^2 was retained as the "best fit" value. For all runs, the Voigt parameters determined from the search program were within the limits set by the Gaussian and Lorentzian fits. In addition, the Voigt parameters were closer in value to the Gaussian or Lorentzian results when the G.F. or L.F. was larger, respectively.

The values of Γ_{nat}, Γ_{instr}, Γ_V, and the minimum χ^2 obtained for individual runs in each target are listed in Tables V, VI, VII, and VIII.

The errors quoted on the widths include uncertainties due to background subtraction and are discussed in detail in section C. As a test for the goodness of fit, the values of χ^2 listed should be compared with the theoretical values of χ^2 for data which have obeyed a function well: i.e.,

$$\chi^2_{th} = n - p \pm \sqrt{2(n-p)} \quad ,$$

where n is the number of data points used in the fit and p is the number of adjustable parameters. Based on this test, the experimental values of χ^2 were generally acceptable, except for the carbon fits. The high values of χ^2 for these sets of data are attributed primarily to the subtraction of muonic contamination lines, which, in the case of carbon, constituted the largest relative fraction of counts under the pionic peak. In addition, the approximation of the random background by a linear term over a wide channel range (120 channels) also contributed to the higher values of χ^2. The uncertainties due to these effects are reflected in the larger errors on Γ_v for the carbon runs. The larger values of Γ_{instr} in the additional carbon runs taken at SREL (K run numbers) were due to the poorer quality FET used in the preamplifier when an FET failure necessitated a quick replacement.

Examples of Voigt fits to the muonic-background subtracted data are given in Fig. 16 and 17 for beryllium and carbon, respectively. Plots of raw experimental data are given in Fig. 18 through 27 for typical pion and muon runs in each target.

2. Li^6 and Li^7 Analysis

The complicated nature of the background in the lithium spectra precluded the use of the Voigt search technique for obtaining

Γ_{nat}. In addition to the expected muonic contamination lines from the lithium targets, higher transitions in carbon and oxygen were also present. The following lines occurred in the channel range used for the analysis:

$$\pi\text{-}L_{\beta}(C^{12}),\ \mu\text{-}L_{\alpha}(O^{16}),\ \mu\text{-}L_{\beta}(Li),\ \mu\text{-}K_{\gamma}(Li),\ \text{and}\ \mu\text{-}K_{\delta}(Li).$$

In addition, the μ-K_{α}(Li) line was contaminated by π-$L_{\alpha}(C^{12})$ events and, therefore, could neither be used to determine Γ_{instr} nor as a reference peak for generating the remaining μ-Li background lines. The oxygen lines were attributed to contamination of the targets and the carbon lines resulted from pion stops in the scintillant of counter 3. In order to account properly for these background lines in the analysis, separate runs were taken with pions stopping in a carbon target and muons stopping in the lithium targets. The shape of the "random" background was also more complicated, being composed of both a broad curved component, centered on the low energy side of the pionic 2p-1s peak, and a linear part. The curved component was attributed to backscatter events which resulted from the pionic 2p-1s line ($\simeq$24 keV) and the combined oxygen (μ-$L_{\alpha}\simeq$25 keV) and carbon (π-$L_{\beta}\simeq$25 keV) lines. The possibility that backscatter peaks could generate such a curved background was verified experimentally by using a Cd^{109} source (intense line at 22 keV) positioned between two equally thick sections of the Li^{6} target in order to simulate the backscatter geometry. The resulting spectrum, indicating a curved background component, is shown in Fig. 28a. For comparison, the Cd^{109} spectrum obtained with normal geometry is shown in Fig. 28b.

These background considerations determined the method by which the lithium data were analyzed in order to obtain Γ_{nat}. The observed 2p-1s pionic line shape was assumed to be a Gaussian, $G(A_v, \bar{x}_v, \Gamma_v)$, and the background components were approximated by separate functions having a total of 6 variable parameters. A least squares fit of the data to this nine-parameter function determined Γ_v for each run. Γ_{instr} was obtained from the 26.36 keV line of Am^{241} used for calibration before and after each run. The natural line width was then obtained from the Voigt table, using the Lorentzian fraction (Γ_{nat}/Γ_v) which corresponded to the Gaussian fraction determined from Γ_v and Γ_{instr}. The G.F. for each run was typically 0.8 to 0.9 and, as a result, the error introduced into Γ_v by assuming a Gaussian line shape for the pionic 2p-1s peak was negligible.

The specific form of the function used in the least-squares fit to the pionic lithium data was determined from the following considerations:

1) pionic 2p-1s peak: A Gaussian line shape was assumed for the pionic 2p-1s peak.

2) π-$L_\beta(C^{12})$ and μ-$L_\alpha(O^{16})$ background lines: from relative intensities obtained in separate pion and muon runs, the ratio of the π-$L_\beta(C^{12})$ amplitude to the μ-$L_\alpha(O^{16})$ amplitude was estimated to be approximately 10/1. The centers of these two lines were the same within $\pm$ 0.5 channels. Therefore, these lines were treated as one Gaussian with its center equal to that of the π-$L_\beta(C^{12})$, its width equal to Γ_{instr}, and with a variable amplitude, A_c.

3) μ-L_β (Li), μ-L_γ (Li) and μ-L_δ (Li) background lines: from muonic runs in lithium, the relative intensities of these lines were approximately 1, 0.15 and 0.06, respectively. The μ-L_γ (Li) and μ-L_δ (Li) lines were neglected because of their small amplitude compared with the pionic 2p-1s amplitude. The μ-L_β (Li) line was treated as a Gaussian peak with a fixed center determined from the muon run, a fixed width given by Γ_{instr}, and a variable amplitude, A_μ.

4) curved background: this was approximated by a Gaussian function with all parameters (A_B, $\bar{x}_B$, Γ_B) variable.

5) flat background: this was approximated by a constant, C.

The final functional form used in the lithium analysis was therefore:

$$Y(x) = A_v e^{-(x-\bar{x}_v)^2(2.35)^2/2\Gamma_v^2} + A_c e^{-(x-\bar{x}_c)^2(2.35)^2/2\Gamma_{instr}^2} + A_\mu e^{-(x-\bar{x}_\mu)^2(2.35)^2/2\Gamma_{instr}^2} + A_B e^{-(x-\bar{x}_B)^2(2.35)^2/2\Gamma_B^2} + C,$$

where the variable parameters were Γ_v, $\bar{x}_v$, A_v, A_c, A_μ, A_B, $\bar{x}_B$, Γ_B, and C. Data from each Li^6 and Li^7 run over the channel range 364-453 were fit by a least-squares method to the above function in order to obtain Γ_v and, hence, Γ_{nat}.

The results of the Li^6 and Li^7 analysis for each run are listed in Tables IX and X, respectively. Good statistical fits to the data were obtained for each run as verified by the values of χ^2. A plot of

the function and the data for run A-17 is shown in Fig. 29. Plots of raw experimental data, including separate muon and pion background runs, are shown in Figs. 30-34 over the channel range 305-545.

C. Error Analysis and Final Results

The error on Γ_{nat}, for a given run, was determined by applying the general rules for the propagation of errors[45] to an approximate formula for the natural line width given by Allen[46]:

$$\Gamma_{nat} = \Gamma_V - \Gamma^2_{instr}/\Gamma_V$$

The values of Γ_{nat} calculated from this relation agreed with the results obtained from the Voigt table to within 5%. The error on Γ_{nat} becomes:

$$(\Delta\Gamma_{nat})^2 = (\Delta\Gamma_V)^2 + (\Gamma^4_{instr}/\Gamma^2_V)[2(\Delta\Gamma_{instr}/\Gamma_{instr})^2 + (\Delta\Gamma_V/\Gamma_V)^2]$$

where $\Delta\Gamma_{instr}$ and $\Delta\Gamma_V$ are errors on the instrumental width and the total (or Voigt) width, respectively. The sources of error affecting the measurement of Γ_{instr} and Γ_V will be discussed separately and, then, the final values of Γ_{nat} for each target will be given.

1. Instrumental Line Width

For all targets, except lithium, it was possible to use the muonic K_α background line as a measure of Γ_{instr}. Since the muonic 2p-1s events were accumulated simultaneously with the pionic 2p-1s events, many possible systematic errors in the measurement of Γ_{instr} were automatically eliminated. For example, some effects which could

have, but did not, introduce a systematic error into Γ_{nat} were:

a) gain drifts during the course of each run,

b) degradation in resolution due to beam effects,

c) effect of target thickness on resolution,

d) sporadic noise pick-up by the preamplifier.

The μ-K_α line is lower in energy than that of the corresponding π-K_α and, therefore, its use as a direct measure of Γ_{instr} could introduce an error because of the resolution vs energy dependence of the detector. This dependence is illustrated in the graphs of Fig. 35a and b for the Ge(Li) and Si(Li) detector, respectively. The solid curves in these figures were determined by using radioactive sources for approximately 20-minute accumulation intervals. The dashed curves were determined from measurements of muonic and, in one case, higher pionic transitions taken during the course of a typical four-hour run. These two graphs indicate the difference in resolution as measured under "laboratory" and "running" conditions, as well as resolution vs energy dependence. The error introduced into Γ_{instr} due to using the lower μ-K_α energy was generally considered negligible except in the case of beryllium. For this target, the μ-K_α energy is 33 keV and the π-K_α energy is 42 keV. The difference in resolution at these energies was approximately 45 volts. Therefore, a correction of + 45 volts was added to Γ_{instr} for each Be run.

For each π-run (except the Li runs), Γ_{instr} was obtained from the μ-K_α line by a least-squares fit to a Gaussian function plus a linear background. The total fitting range typically extended over at least four times that of the FWHM (channels). The data were fit over

selected channel ranges within this total range in order to determine the change in Γ_{instr} as a function of the fitting range. The total variation in Γ_{instr} did not exceed two statistical standard deviations and resulted from a change in the linear background term vs fitting range. Therefore, $\Delta\Gamma_{instr}$ was chosen to be twice the standard deviation as determined by the computer fit. The value for the instrumental line width was selected from the fit over the widest range of channels because the background was more reliably represented over this range.

As noted previously, the μ-K_α line of lithium was contaminated and could not be used to determine Γ_{instr}. Instead, the 26.36 keV line of Am^{241}, appearing in calibration runs taken before and after each pion run, was used to determine Γ_{instr}. Since the calibration runs were not taken during the π-runs, a correction of +23 volts (see Fig. 35a and b) was added to the average width of the calibration lines in order to obtain Γ_{instr}. Due to this additional uncertainty in determining Γ_{instr} for the lithium runs, $\Delta\Gamma_{instr}$ was chosen to be three times the standard deviation as determined from the computer fits to the 26.36 keV lines.

2. Total Line Width

The error on the total line width of the pionic 2p-1s peak reflected uncertainties due to background subtraction and constituted a major fraction of the final error on the natural line width. In order to include the effects of background uncertainties into Γ_v, a number of fits and different background assumptions were used in the

analysis. The resulting spread, $\Delta\Gamma_V(\text{bgnd.})$, in the total width from these fits was taken as an estimate of the error on Γ_V due to uncertainty in background subtraction. This error was then added to the standard deviation on the total width to obtain $\Delta\Gamma_V$: i.e.,

$$\Delta\Gamma_V = \Delta\Gamma_V(\text{std.dev.}) + \Delta\Gamma_V(\text{bgnd.})$$

Data from all targets, except lithium, were treated in a similar manner. Among these targets (Be^9, B^{10}, B^{11} and C^{12}), the worst case was studied in detail and the percent effect on Γ_V was taken as an estimate of $\Delta\Gamma_V(\text{bgnd.})$ for the remaining targets. The carbon spectra exhibited the most serious background problem, which was due, primarily, to the low yield of pionic 2p-1s X-rays. In the carbon runs, the μ-K_β, μ-K_γ, and μ-K_δ lines had to be subtracted whereas all other targets required only the subtraction of the μ-K_β and μ-K_γ lines. For a typical carbon spectrum, the parameters describing the background peaks were varied plus and minus one standard deviation and used in various combinations, giving a total of nine sets of subtraction parameters. The total change in Γ_V resulting from fits to these nine spectra was approximately 5% of Γ_V. Thus, $\Delta\Gamma_V(\text{bgnd.})$ was assumed to be $.05\Gamma_V$ for each run with the above targets. The error on the total width was then

$$\Delta\Gamma_V = \Delta\Gamma_V(\text{std.dev.}) + 0.05\Gamma_V \ ,$$

where $\Delta\Gamma_V(\text{std.dev.})$ was determined from the largest standard deviation on the total width as given by the Gaussian or Lorentzian fit for each run. The change in Γ_V as a function of both the Voigt channel range and of the variation of Γ_{instr} over its error was always within $\Delta\Gamma_V$ as defined above.

For the lithium data, the dependence of Γ_V on the background (section B-2) was determined by fitting the data over different channel ranges and with the background parameters being held fixed or free to vary. In addition, the fixed parameters were changed by ±10% in order to determine their effect on the total width. All together, the number of free parameters ranged from 3 to 11 and the channel fitting region from 364-453 to 400-440. The total change in Γ_V was 50 volts which was taken as an estimate of $\Delta\Gamma_V$(bgnd.) for the lithium data. The final error on Γ_V for each run was obtained by adding 50 volts to the standard deviation on the total width:

$$\Delta\Gamma_V = \Delta\Gamma_V(\text{std.dev.}) + 50 \text{ volts}$$

As a consistency check, the widths of the pionic-lithium 3p-1s peaks were determined. These peaks had few statistics and therefore the separate Li^6 and Li^7 runs were respectively added together. Although the 3p-1s peaks were free from muon contamination lines, there was evidence of a backscatter peak on the low energy side. Thus, a Gaussian function plus a fixed constant background term were used to fit the 3p-1s sum data over the limited channel range 468-490. The total widths obtained were:

$$\Gamma_V(Li^6;3p\text{-}1s) = 0.710 \text{ keV}$$
$$\Gamma_V(Li^7;3p\text{-}1s) = 0.740 \text{ keV}$$

For comparison, an average of the total pionic 2p-1s widths of Li^6 and Li^7 (from Tables IX and X) is given:

$$\Gamma_V(Li^6;2p\text{-}1s) = 0.686 \text{ keV}$$
$$\Gamma_V(Li^7;2p\text{-}1s) = 0.707 \text{ keV}$$

In view of the errors quoted on separate runs, the agreement between the pionic 3p-1s and 2p-1s widths is good.

There are several other general sources of error which can affect a width measurement, but which will be shown to be negligible. These sources are:

a) statistical error on the slope, M(keV/ch),

b) non-linearities in pulse height analysis system.

Each will be considered in turn.

If a linear response is assumed, the conversion from channels to energy for a width measurement is given by

$$\Gamma_E = M\Gamma_{ch} \ ,$$

$$\text{with } M = \frac{E_2 - E_1}{x_2 - x_1} \ .$$

E_2 and E_1 are calibration energies and x_2 and x_1 their corresponding peak channel locations. If no error is assumed on Γ_{ch}, the error on Γ_E becomes:

$$\Delta\Gamma_E = \Gamma_{ch}\Delta M$$

$$= M\Gamma_{ch} \sqrt{\frac{(\Delta E_1)^2 + (\Delta E_2)^2}{(E_2 - E_1)^2} + \frac{(\Delta x_2)^2 + (\Delta x_1)^2}{(x_2 - x_1)^2}}$$

where the general rules for error propagation have been used to calculate ΔM.

If the following typical values

$$\Delta E_2 = \Delta E_1 = 2 \times 10^{-2} \text{ keV},$$

$$E_2 - E_1 = 25 \text{ keV},$$

$$x_2 - x_1 = 130 \text{ ch, and}$$

$$\Delta x_2 = \Delta x_1 = 0.07 \text{ ch}$$

are used, then $\Delta\Gamma_E = 8$ volts. Therefore, the error introduced into a width measurement because of the statistical error on the slope can be considered negligible for this experiment.

Non-linearities in the pulse height analysis system affect a width measurement in two ways:

1) deviation from the assumed linear response introduces an error in the slope (integral non-linearity).
2) non-uniform channel widths represent variations in the slope from channel to channel and thus introduce an error (differential non-linearity).

The error introduced into the slope as a result of integral non-linearity was estimated by using a precision pulser.[47] Pulser peaks stored at 30-channel intervals were used to generate the "true response" of the system. The percent spread among values of the slope given by any pair of pulser dial settings and corresponding peak centers did not exceed 0.2%; i.e.,

$$|\Delta M/\bar{M}| < 0.2\%$$

Therefore, an estimate of the error introduced into a width measurement due to integral non-linearity was taken to be:

$$\Delta\Gamma(\text{integral non-linearity}) = 0.002M\Gamma_{ch}$$

If a typical width of 10 channels is assumed for Γ_{ch}, $\Delta\Gamma$ is less than 4 volts for the Ge(Li) spectrometer (M = 0.192 keV/ch) and less than 2 volts for the Si(Li) spectrometer (M = 0.076 keV/ch), and is therefore negligible.

The differential non-linearity was measured with a Berkeley Nucleonics Pulser, Model GL-3, whose specification is an inherent differential non-linearity of less than $\pm 0.25\%$. Measurements indicated that the channel-width non-uniformity was approximately $\pm 1\%$. In order to obtain a conservative estimate of $\Delta\Gamma$ due to differential non-linearity, the assumption was made that every channel in a width measurement systematically deviated from the average channel width by 1%. Then, the error on a 10-channel width would be:

$$\Delta\Gamma(\text{differential non-linearity}) = 0.01M\Gamma_{ch}$$
$$= 19 \text{ volts for Ge(Li) system}$$
$$= 8 \text{ volts for Si(Li) system}$$

On the basis of these estimates, it can be concluded that system non-linearities introduced a negligible error into the width measurements.

The final result for the natural line width of the 2p-1s pionic transition in each target was determined by taking a weighted

average of Γ_{nat} obtained from the separate runs. Each value of Γ_{nat} used in the average was weighted inversely proportional to its error. The error on the mean value of Γ_{nat} was computed by taking deviations from the mean and by compounding individual errors. The larger of these two errors was selected as the final error on the mean. The final results are listed in Table XI along with the corresponding absorption rates computed from $\Gamma_{nat}/\hbar$. The line width for B^{11} includes a -4% correction due to the 20% B^{10} contamination of the target. The corrections for isotopic impurities were negligible for the other targets.

VI. DISCUSSION OF RESULTS

In this section, a comparison between theory and experiment will be given for the natural line widths of 1s states in low Z pionic atoms. Theoretical values for the line widths are obtained from eqs. (3) and (4) of the introduction which, for s states, reduce respectively to

$$\Gamma_{nat}(S.E.) = 2E_o(2K_oR)^2 \ Im\left[\frac{-1/5 - i2m_\pi V_I R/3\hbar^2 K_o}{1 + 2K_oR + i2m_\pi V_I R^2/3\hbar^2}\right] \tag{6}$$

and

$$\Gamma_{nat}(pert.) = 2\int V_I|\psi_{1s}|^2 d\tau \tag{7}$$

where $V_I = \nu\rho^2$.

Since the s-state wave function is essentially constant over the volume of the nucleus, the contribution from the velocity-dependent part of the pion-nucleus interaction is expected to be small. Thus, there is no explicit dependence on α for s states in eq. (3); also, the corresponding gradient term of eq. (4) is neglected for s states since its contribution to the width is less than 0.5% of the local term.

Basing her conclusion on eq. (3), M. Ericson[26] states that first-order perturbation theory is a valid approximation for the s-state pion-nucleus interaction. This result follows from the expression

obtained for ΔE in the limit as $R \to 0$. For example, eq. (6) above for the width reduces to

$$\lim_{R\to 0} \Gamma_{nat}(S.E.) = 8V_I Z^3 R^3/(3a_\pi^3)$$

$$\text{where } a_\pi = \hbar^2/(m_\pi e^2)$$

According to eq. (7), first-order perturbation theory gives for a constant V_I:

$$\begin{aligned}\Gamma_{nat}(pert.) &= 2V_I \int |\psi_{1s}(r)|^2 d\tau \\ &\simeq 2V_I |\psi_{1s}(o)|^2 4\pi R^3/3 \\ &= 8V_I Z^3 R^3/(3a_\pi^3)\end{aligned}$$

The use of first-order perturbation theory as a valid approximation for the pionic atom contradicts the conclusions of Seki and Cromer[48]. In their work, the complex 2p-1s shifts measured by Jenkins et.al., were used to calculate a square well π^--nucleus potential by solving the Schrodinger equation numerically. The probability that the pion is inside the nucleus was then calculated by them using both

$$\int |\psi_{exact}|^2 d\tau \equiv \Delta E_{sp}/V_I \qquad (8)$$

and $$\int |\psi_{coul}|^2 d\tau, \qquad (9)$$

where ΔE_{sp} = measured 2p-1s width,

V_I = potential calculated from ΔE_{sp}, and

ψ_{coul} = hydrogen-like wave function.

The results of eq. (9) were approximately a factor of two larger than those of eq. (8). According to these results, first-order perturbation theory should yield widths which are too large by a factor of two.

In order to compare theory and experiment, the natural line widths have been calculated according to eqs. (6) and (7). With the constants evaluated explicitly, these become respectively:

$$\Gamma_{nat}(S.E.) = aZ^4R^2 \frac{[(\nu A^2 b/ZR^5)(1 + RZc) - \nu A^2 d/R^4]}{(1 + RZc)^2 + (\nu A^2 e/R^4)^2} \quad keV \tag{10}$$

$$\Gamma_{nat}(pert.) = (f\nu A^2 Z^3/R^6)[e^{kR}\{R^2/k - 2R/k^2 + 2/k^3\} - 2/k^3] \quad keV \tag{11}$$

where $a = 0.78 \times 10^{-3}$

$b = 2.68 \times 10^{-2}$

$c = 1.03 \times 10^{-2}$

$d = 0.27 \times 10^{-4}$

$e = 1.36 \times 10^{-4}$

$f = 0.63 \times 10^{-4}$

$k = -1.03 \times 10^{-2} Z$

R is the nuclear radius in units of F

ν is in units of MeV F^6

Z is the number of protons

A is the number of nucleons

A constant nuclear density has been used for ρ and a hydrogen-like wave function for Ψ_{1s}:

$$\rho = \frac{A}{\frac{4}{3}\pi R^3}$$

$$\Psi_{1s}(r) = (Z/a_\pi)^{3/2} \frac{1}{\sqrt{\pi}} e^{-Zr/a_\pi}$$

From the deuteron-model calculation of M. Ericson[26], ν was found to be 165 ± 20 MeV F^6. An independent value for ν is obtained from the optical

model calculation of Ericson and Ericson.[19] This value is not given directly, but can be extracted from the optical potential as an "effective ν".

The complete optical potential derived by the Ericsons, including one- and two-nucleon contributions, is given in the form

$$V(r) = \frac{\hbar^2}{2m_\pi}\left[-m_1(r) - m_2(r) + \frac{\nabla \cdot (n(r) - i4\pi d_0 \vec{\sigma}(r)\Lambda)\nabla}{1 + n(r)/3} \right]$$

where
1. m_1 and m_2 are one- and two-nucleon contributions, respectively, representing the local part of the interaction,
2. n is the non-local interaction and contains both one- and two-nucleon terms,
3. d_0 is a single-nucleon parameter,
4. $\vec{\sigma}(r)$ is the nucleon spin density,
5. only m_2 and the two-nucleon part of n contain imaginary parameters.

An "effective ν" can be obtained from this potential by considering each term and calculating its contribution to the imaginary part of the potential. The spin density term in the vector cross product gives rise to a strong hyperfine interaction which could affect the experimental width of a state only because of the level splitting that it introduces. For a spin density proportional to the nucleon density, the strong hyperfine interaction potential is of the form

$$V(H.F.) = \frac{-4\hbar^2\pi d_0}{m_\pi} \frac{\vec{F} \cdot \vec{L}}{A} \frac{(\vec{I} \cdot \vec{F})}{F(F+1)} \frac{1}{r} \frac{d\rho}{dr} ,$$

where $\vec{I}$ = nuclear spin,

$\vec{F}$ = total angular momentum of pion-nucleus system, and

$\vec{L}$ = orbital angular momentum of pion.

The splitting induced by this interaction was estimated using first-order perturbation theory and found to be less than 0.1 eV for the maximum splitting of the p state in Li^6. It was, therefore, considered negligible.

With the assumption that both spin and isospin densities are proportional to a constant nucleon density and that the hyperfine interaction is small, the optical potential can be written in terms of constant parameters as

$$V = \frac{\hbar^2}{2m_\pi} \left[- m_1 - m_2 + \nabla \cdot \alpha \nabla \right]$$

For absorption from the s state, only the imaginary part of the local two-nucleon term m_2 contributes to the width. This term is given explicitly by Ericson and Ericson[19] and may be written in the form ($\hbar = m_\pi = c = 1$):

$$\text{Im } m_2 = 4\pi \text{ Im } B_0(\text{eff})\rho^2$$

where $\text{Im } B_0(\text{eff}) = (1 + m_\pi/2M)[\text{Im}\{B_0 + \Delta B(A^{-1}) + \Delta B(\text{F.M.})\}]$,

with M the nucleon mass.

The dominating term in $\text{Im } B_0(\text{eff})$ is the constant term $\text{Im } B_0$ of the two-nucleon scattering operator for s-wave pions. The remaining terms in the s-wave scattering operator depend on constants B_k, nucleon spin, and isospin and contribute to order A^{-1}. The contribution of these terms

constitutes $\Delta B(A^{-1})$ which is computed from an expression given by the Ericsons and listed in Appendix C of this paper. The Fermi motion of the nucleons is taken into account by writing the p-wave scattering operator as a translationally invariant quantity in terms of the relative velocities of the pion and the two scattering nucleons. As a result, there is an induced s-wave interaction whose contribution to Im m_2 is given by

$$[\text{Im } \Delta B(\text{F.M.})]\rho^2 \simeq \text{Im } C_0 \, (m_\pi/2M)^2(6p_n^2/5)\rho^2$$

where p_n = Fermi momentum $\simeq$ 250 MeV/c.

The value of Im C_0 is given by the Ericsons to be 0.088 and yields for the correction due to Fermi motion

$$\text{Im } \Delta B(\text{F.M.}) = 0.002.$$

The factor $1 + m_\pi/2M$ is a kinematical correction which multiplies the free scattering amplitude in order to account correctly for scattering of pions from bound nucleons. Numerically, this factor is 1.07. Im B_0(eff) can now be written ($\hbar = c = m_\pi = 1$)

$$\text{Im } B_0(\text{eff}) = 1.07 \, [\text{Im}\{B_0 + \Delta B(A^{-1})\} + 0.002]$$

The imaginary part of the optical potential for s states becomes

$$V_I = -(\hbar^2/2m_\pi) \, 4\pi \text{Im } B_0(\text{eff})\rho^2$$

Therefore, in units of MeV F^6, the parameter ν(eff) is

$$\begin{aligned}\nu(\text{eff}) &= -(\hbar^2/2m_\pi) \, 4\pi \text{Im } B_0(\text{eff})(\hbar/m_\pi c)^4 \text{ MeV } F^6 \\ &= -(7.94 \times 10^3 \text{ MeV } F^6) \text{ Im } B_0(\text{eff}) \qquad (12)\end{aligned}$$

The dominant term Im B_0 is evaluated from a formula given by the Ericsons[19]:

$$\text{Im } B_0 = (1/48)(9 \text{ Im } \beta_{11} + 3 \text{ Im } \beta_{01})$$

where Im β_{11} and Im β_{01} are proportional to the cross sections for s-wave pion absorption onto the triplet and singlet states, respectively, of two nucleons. Im β_{01} was obtained from the measured cross section[49] for the reaction $p + p \rightarrow \pi^0 + p + p$ by using the principles of detailed balance and charge independence resulting in

$$\text{Im } \beta_{01} = 0.054 \pm 0.020.$$

Im β_{11} was obtained by the Ericsons from the experimental cross section[50] for the reaction $p + p \rightarrow D + \pi^+$, yielding

$$\text{Im } \beta_{11} = 0.044 \pm 0.004.$$

The s-wave cross section for this process has recently been re-measured[51] to the same absolute precision by studying the inverse reaction $\pi^+ + D \rightarrow p + p$ at low energies and was found to be a factor 0.240/0.138 larger than the results used by the Ericsons. This measurement results in a new value of Im β_{11},namely

$$\text{Im } \beta_{11}' = (0.240/0.138)(0.044)$$
$$= 0.0765 \pm 0.004.$$

The natural line widths for pionic s states have been calculated using eqs. (10) and (11) for values of $\nu(\text{eff})$ obtained from eq. (12).

These results are listed in Tables XII and XIII for values of Im β_{11} and Im β'_{11}, respectively. The nuclear radii were taken from electron scattering data. The uncertainty in the calculated widths due to errors in experimental parameters is approximately 15%.

The following conclusions can be made from a comparison of the results given in these tables:

1. Theory and experiment agree very well when β'_{11} is used in the width calculation, but disagree when β_{11} is used. Unlike β_{11}, the parameter β'_{11} was determined from a cross section measurement in the low energy range where s-wave scattering dominates and would, therefore, seem to be a more reliable measure of the cross section for s-wave pion absorption at zero energy. In addition, the recent cross section measurement from which β'_{11} was obtained resolves a discrepancy[51] in the prediction of the pion photo-production cross section from the reaction $p + p \rightarrow \pi^+ + D$. If β'_{11} is assumed to be accurate, it can be stated that the optical-model potential derived by Ericson and Ericson[19] predicts 1s line widths for low Z atoms which are in substantial agreement with the results of this experiment.
2. The value of $\nu = 165 \pm 20$ obtained by M. Ericson[26] in the deuteron-model calculation is in agreement with the optical-model calculation. This conclusion follows by comparing 165 ± 20 to the average value, 140, of $\nu(\mathrm{eff})$ obtained from Table XII. Table XII must be used for this comparison since

the results listed there depend on the earlier cross section measurement[50] of the reaction $p + p \rightarrow \pi^+ + D$ which was also the one used by M. Ericson in the deuteron-model calculation. The more recent cross section measurement of Rose[51] would tend to force the value of ν obtained from the deuteron-model calculation to a higher value and thus be in better agreement with the average value of $\nu(\text{eff})$ taken from Table XIII. On the basis of these comparisons, it can be concluded that the deuteron model of M. Ericson provides an adequate description of pion absorption from the 1s states of low Z atoms.

3. The corrections to the dominant term Im B_0 are not small and are essential if theory is to agree with this experiment. These corrections constitute a +60% enhancement of Im B_0 for Li^6 and +35% for C^{12}.

4. The assumption that pion absorption proceeds primarily by a two-nucleon process leads to theoretical values for 1s line widths in low Z atoms which are in agreement with the results of this experiment. This assumption is also supported by experimental studies[52] of the angular distribution of two-nucleon emission following pion absorption.

5. The 1s widths, $\Gamma(\text{pert.})$, calculated from first-order perturbation theory using $V_I = \nu(\text{eff})\rho^2$ are in agreement with experiment and are approximately 4% larger than the values, $\Gamma(\text{S.E.})$, obtained from the Schrodinger equation. These

results contradict the conclusion of Seki and Cromer[48], which were based on earlier width measurements, that first-order perturbation theory used to describe pion absorption effects is invalid.

Table XIV is a summary of pionic 2p-1s line widths measured at William and Mary, CERN, and Berkeley. The agreement among the various experimental results is generally satisfactory for low Z elements. However, wide discrepancies exist for widths measured in elements above N^{14}. Width measurements for this range of elements become increasingly more difficult because of the lower yield of 2p-1s X-rays. The theoretical widths begin to diverge from the experimental results in this range, becoming larger than either CERN's or Berkeley's results. In view of the above inconsistencies as well as the agreement which exists between theory and experiment for low Z elements, it would seem desirable to have precise measurements made of the 2p-1s line widths for elements with $Z > 7$.

VII. LIST OF TABLES

Table I - Noise of TC-130, FWHM (Si), for different first-stage configurations at zero external capacitance. Single differentiation was used with equal time constants of 3.2 μsec.

First-stage of TC-130	Preamplifier noise, FWHM (Si) in keV.	
	Room temperature	Cooled
Fig. 4a	1.58	——
Fig. 4b	1.16	0.88
Fig. 4c	0.89	0.63
Fig. 4d	0.64	0.39

Table II - Count-rate in Ge(Li) detector vs resolution (FWHM) of the 1.33 MeV line of Co^{60}. The first-stage configuration of the preamplifier was as shown in Fig. 6. Equal differentiation and integrating time constants of 1.6 μsec were used in the TC-200 which also had pole-zero cancellation.

Count rate (10^3 sec^{-1})	Resolution (FWHM) in keV
13.0	5.30
8.0	4.44
5.0	4.01
3.0	3.17
1.0	2.48
0.5	2.19

Table III - Measured muonic transition energies and relative intensities. The measured $\pi - K_\alpha$ and $\mu - K_\alpha$ energies are also listed and were supplied by W. B. Shuler (Thesis, William and Mary 1968). All energies are in keV.

ELEMENT	$E(\pi K_\alpha)$	$E(\mu K_\alpha)$	$E(\mu K_\beta)$	$I(K_\beta/K_\alpha)$	$E(\mu K_\gamma)$	$I(K_\gamma/K_\alpha)$	$E(\mu K_\delta)$	$I(K_\delta/K_\alpha)$
Li^6	24.18	18.64	22.1	0.37	23.3	0.05	——	——
Li^7	24.06	18.69	22.2	0.36	23.5	0.05	——	——
Be^9	42.32	33.39	39.5	0.18	41.6	0.05	43.1	0.01
B^{10}	65.79	52.18	61.9	0.55	65.2	0.3	66.5	0.06
B^{11}	65.00	52.23	62.0	0.60	65.3	0.3	66.6	0.06
C^{12}	93.19	75.23	89.3	0.31	94.3	0.16	96.5	0.04

Table IV - Tabulation of Voigt profiles (from ref. 44).

Parameters		Lorentzian Fraction	Gaussian Fraction	$\Psi(0, \eta)$	$\delta/2$	ρ	$\Psi(x, \eta)$ as a Fraction of $\Psi(0, \eta)$												
η	$1/\eta$						0.95	0.90	0.85	0.80	0.70	0.60	0.40	0.30	0.25	0.20	0.15	0.10	0.05	0.02	0.01
							x in Terms of $\delta/2$ (Width in Terms of Half-Value Width)												
0.1000....	10.00	0.993	0.083	0.99507$_3$	1.0074$_4$	1.3669$_2$	0.2304$_1$	0.3346$_2$	0.4215$_1$	0.5011$_1$	0.6559$_2$	0.8172$_9$	1.2235$_4$	1.5245$_2$	1.7277$_9$	1.9941$_0$	2.3722$_5$	2.9881$_8$	4.3395$_8$	6.9668$_8$	9.9017$_7$
0.2000....	5.00	.972	.162	.98109$_4$	1.0290$_2$	1.5559$_0$	.2330$_2$	.3380$_1$	.4252$_2$	.5058$_4$	.6593$_4$	.8194$_6$	1.2202$_1$	1.5161$_4$	1.7158$_5$	1.9774$_8$	2.3491$_2$	2.9547$_6$	4.2848$_6$	6.8730$_8$	9.7656$_4$
0.3000....	3.33	.941	.235	.96002$_0$	1.0629$_9$	1.5392$_6$	.2364$_1$	.3425$_0$	.4303$_1$	.5105$_1$	.6640$_4$	.8224$_0$	1.2154$_1$	1.5038$_6$	1.6982$_4$	1.9529$_0$	2.3147$_3$	2.9048$_9$	4.2029$_0$	6.7323$_2$	9.5613$_0$
0.4000....	2.50	.904	.301	.93411$_1$	1.1071$_0$	1.5189$_2$	.2400$_3$	.3472$_0$	.4356$_2$	.5160$_3$	.6691$_4$	.8258$_2$	1.2099$_0$	1.4894$_0$	1.6775$_6$	1.9234$_0$	2.2734$_1$	2.8446$_1$	4.1033$_7$	6.5610$_4$	9.3124$_2$
0.4444....	2.25	.886	.327	.92158$_1$	1.1293$_8$	1.5091$_8$	.2415$_3$	.3492$_2$	.4378$_9$	.5184$_4$	.6713$_8$	.8272$_3$	1.2074$_0$	1.4828$_6$	1.6678$_1$	1.9098$_4$	2.2538$_7$	2.8159$_6$	4.0558$_6$	6.4791$_0$	9.1933$_0$
0.5000....	2.00	.863	.359	.90535$_1$	1.1592$_2$	1.4967$_0$	.2433$_1$	.3516$_1$	.4406$_1$	.5213$_1$	.6740$_1$	.8290$_5$	1.2043$_7$	1.4746$_1$	1.6557$_1$	1.8925$_1$	2.2291$_0$	2.7794$_1$	3.9950$_0$	6.3739$_8$	9.0404$_3$
0.6666....	1.50	.794	.441	.85499$_2$	1.2591$_1$	1.4591$_8$	.2479$_5$	.3578$_2$	.4476$_8$	.5287$_8$	.6809$_0$	.8337$_8$	1.1958$_9$	1.4513$_7$	1.6211$_0$	1.8421$_9$	2.1561$_0$	2.6703$_0$	3.8115$_1$	6.0556$_8$	8.5768$_4$
0.8000....	1.25	.742	.494	.81493$_6$	1.3472$_7$	1.4306$_8$	.2509$_4$	.3617$_3$	.4521$_9$	.5335$_6$	.6854$_9$	.8368$_2$	1.1902$_4$	1.4354$_0$	1.5968$_6$	1.8061$_7$	2.1025$_8$	2.5885$_8$	3.6717$_9$	5.8114$_9$	8.2206$_4$
1.0000....	1.00	.672	.559	.75787$_7$	1.4884$_8$	1.3924$_8$	.2543$_8$	.3663$_6$	.4574$_1$	.5391$_6$	.6907$_1$	.8403$_9$	1.1835$_4$	1.4160$_4$	1.5670$_4$	1.7609$_8$	2.0336$_9$	2.4802$_7$	3.4822$_0$	5.4771$_8$	7.7316$_8$
1.0526....	0.95	.655	.574	.74364$_8$	1.5269$_4$	1.3833$_4$	.2551$_2$	.3673$_8$	.4585$_4$	.5403$_0$	.6918$_8$	.8411$_6$	1.1820$_7$	1.4117$_7$	1.5604$_2$	1.7507$_8$	2.0178$_7$	2.4547$_9$	3.4366$_4$	5.3962$_0$	7.6130$_7$
1.1111....	0.90	.637	.589	.72826$_8$	1.5701$_7$	1.3736$_0$	.2558$_4$	.3683$_7$	.4597$_2$	.5415$_8$	.6930$_2$	.8419$_8$	1.1805$_8$	1.4073$_8$	1.5535$_8$	1.7402$_2$	2.0013$_6$	2.4279$_3$	3.3881$_1$	5.3095$_8$	7.4859$_8$
1.1765....	0.85	.618	.605	.71160$_0$	1.6190$_3$	1.3634$_4$	.2566$_6$	.3694$_1$	.4609$_1$	.5427$_3$	.6942$_1$	.8427$_7$	1.1790$_2$	1.4028$_4$	1.5465$_1$	1.7293$_1$	1.9841$_6$	2.3996$_2$	3.3364$_4$	5.2169$_1$	7.3499$_8$
1.2500....	0.80	.597	.622	.69352$_7$	1.6746$_0$	1.3525$_2$	.2574$_8$	.3704$_8$	.4621$_8$	.5440$_8$	.6954$_2$	.8436$_1$	1.1774$_4$	1.3982$_1$	1.5392$_4$	1.7180$_3$	1.9663$_0$	2.3699$_0$	3.2813$_4$	5.1176$_7$	7.2040$_6$
1.3333....	0.75	.575	.639	.67389$_3$	1.7382$_2$	1.3409$_8$	.2582$_3$	.3715$_7$	.4633$_7$	.5454$_0$	.6970$_9$	.8444$_8$	1.1758$_2$	1.3934$_7$	1.5318$_1$	1.7064$_4$	1.9478$_3$	2.3387$_6$	3.2226$_8$	5.0112$_9$	7.0474$_4$
1.4286....	0.70	.552	.656	.65253$_1$	1.8116$_7$	1.3287$_2$	.2591$_1$	.3726$_8$	.4646$_4$	.5467$_4$	.6979$_8$	.8453$_3$	1.1741$_7$	1.3886$_3$	1.5242$_2$	1.6945$_8$	1.9287$_6$	2.3062$_8$	3.1601$_8$	4.8971$_6$	6.8791$_9$
1.5385....	0.65	.527	.675	.62925$_2$	1.8972$_8$	1.3157$_4$	.2599$_8$	.3738$_2$	.4659$_4$	.5481$_1$	.6992$_4$	.8462$_1$	1.1725$_0$	1.3837$_0$	1.5164$_3$	1.6824$_7$	1.9092$_1$	2.2724$_1$	3.0937$_2$	4.7745$_0$	6.6981$_3$
1.6666....	0.60	.500	.694	.60384$_8$	1.9979$_7$	1.3010$_3$	.2608$_2$	.3749$_7$	.4672$_8$	.5495$_0$	.7005$_6$	.8471$_1$	1.1707$_9$	1.3787$_0$	1.5086$_2$	1.6701$_4$	1.8892$_4$	2.2374$_3$	3.0231$_1$	4.6427$_3$	6.5029$_6$
1.8181....	0.55	.472	.715	.57606$_3$	2.1180$_1$	1.2874$_2$	.2617$_1$	.3761$_4$	.4685$_9$	.5509$_2$	.7018$_9$	.8480$_1$	1.1690$_7$	1.3736$_4$	1.5006$_7$	1.6576$_1$	1.8689$_2$	2.2014$_4$	2.9482$_7$	4.5008$_0$	6.2922$_8$
2.0000....	0.50	.442	.736	.54564$_1$	2.2632$_0$	1.2720$_1$	.2626$_0$	.3773$_4$	.4699$_4$	.5523$_4$	.7032$_4$	.8489$_4$	1.1673$_2$	1.3685$_3$	1.4926$_5$	1.6450$_5$	1.8483$_8$	2.1647$_0$	2.8692$_8$	4.3477$_8$	6.0641$_8$
2.2222....	0.45	.410	.758	.51226$_3$	2.4419$_4$	1.2557$_2$	.2635$_1$	.3785$_4$	.4713$_3$	.5538$_1$	.7046$_3$	.8498$_3$	1.1655$_7$	1.3633$_8$	1.4845$_3$	1.6323$_8$	1.8277$_1$	2.1275$_0$	2.7863$_8$	4.1825$_8$	5.8168$_1$
2.5000....	0.40	.375	.780	.47557$_8$	2.6668$_7$	1.2385$_1$	.2644$_3$	.3797$_7$	.4727$_8$	.5552$_8$	.7060$_1$	.8508$_2$	1.1637$_8$	1.3582$_1$	1.4764$_9$	1.6197$_0$	1.8070$_8$	2.0901$_8$	2.7001$_8$	4.0037$_1$	5.5475$_8$
2.8571....	0.35	.338	.804	.43518$_0$	2.9577$_6$	1.2203$_8$	.2653$_8$	.3810$_1$	.4741$_4$	.5567$_1$	.7074$_1$	.8517$_7$	1.1620$_9$	1.3530$_4$	1.4684$_1$	1.6070$_7$	1.7863$_2$	2.0530$_1$	2.6119$_6$	3.8100$_8$	5.2532$_1$
3.3333....	0.30	.299	.829	.39061$_2$	3.3477$_4$	1.2012$_2$	.2663$_0$	.3822$_6$	.4755$_8$	.5582$_7$	.7088$_2$	.8527$_3$	1.1602$_8$	1.3479$_0$	1.4603$_7$	1.5945$_4$	1.7662$_2$	2.0164$_2$	2.5232$_8$	3.6002$_8$	4.9298$_0$
4.0000....	0.25	.257	.855	.34135$_1$	3.8962$_8$	1.1810$_6$	.2672$_4$	.3835$_1$	.4769$_9$	.5597$_8$	.7102$_8$	.8536$_8$	1.1584$_7$	1.3427$_8$	1.4523$_7$	1.5821$_4$	1.7462$_4$	1.9806$_7$	2.4360$_0$	3.3740$_4$	4.5719$_3$
5.0000....	0.20	.212	.882	.28679$_0$	4.7221$_9$	1.1598$_8$	.2681$_9$	.3847$_8$	.4784$_3$	.5613$_0$	.7116$_4$	.8546$_3$	1.1567$_0$	1.3376$_8$	1.4444$_8$	1.5699$_4$	1.7267$_2$	1.9460$_8$	2.3525$_3$	3.1355$_8$	4.1726$_4$
6.6666....	0.15	.164	.910	.22623$_7$	6.1031$_8$	1.1376$_2$	.2691$_8$	.3860$_4$	.4798$_7$	.5628$_2$	.7130$_8$	.8556$_1$	1.1549$_4$	1.3326$_1$	1.4366$_9$	1.5579$_6$	1.7077$_0$	1.9128$_4$	2.2743$_8$	2.8987$_1$	3.7248$_7$
10.0000....	0.10	0.113	0.939	0.15889$_8$	8.8716$_1$	1.1143$_2$	.2701$_1$	.3873$_2$	.4813$_2$	.5643$_4$	.7145$_0$	.8565$_6$	1.1532$_6$	1.3276$_4$	1.4290$_4$	1.5462$_7$	1.6892$_7$	1.8811$_8$	2.2026$_6$	2.6862$_7$	3.2450$_7$
0.....	$(1+x^2)^{-1}$	1	0	1	1	$\pi/2$	.2294$_2$	.3333$_3$	.4200$_8$	.5000$_0$	.6546$_8$	.8165$_0$	1.2247$_8$	1.5275$_3$	1.7320$_8$	2.0000$_0$	2.3804$_8$	3.0000$_0$	4.3589$_6$	7.0000$_0$	9.9498$_7$
∞.....	$\pi^{-1/2}e^{-x^2}$	0	1	$\pi^{-1/2}$ 0.56419$_6$	$(\log e2)^{1/2}$ 0.8325$_6$	$\frac{1}{2}\pi^{1/2}\cdot(\log e2)^{-1/2}$ 1.0644$_7$	0.2720$_3$	0.3898$_8$	0.4842$_2$	0.5673$_9$	0.7173$_4$	0.8584$_7$	1.1497$_8$	1.3179$_4$	1.4142$_1$	1.5237$_9$	1.6543$_8$	1.8226$_2$	2.0789$_2$	2.3756$_8$	2.5775$_7$

Table V - Results of pionic 2p-1s width analysis for each Be^9 run. Number of degrees of freedom in each fit equals 66. Widths in keV.

RUN	χ^2	Γ_v	Γ_{instr}	Γ_{nat}	Total Counts
A20	75	1.028±0.095	0.678±0.036	0.562±0.109	4187
A21	79	1.025±0.113	0.674±0.044	0.563±0.130	1794
A22	91	0.984±0.097	0.701±0.040	0.467±0.116	3377
A26	84	1.057±0.098	0.665±0.052	0.623±0.115	1669
A31	52	1.083±0.097	0.664±0.046	0.659±0.111	2621

Table VI - Results of pionic 2p-1s width analysis for each B^{10} run. Number of degrees of freedom in each fit equals 48. Widths in keV.

RUN	χ^2	Γ_v	Γ_{instr}	Γ_{nat}	Total Counts
G5	72	2.091±0.305	1.033±0.115	1.552±0.324	1011
G12	74	2.406±0.229	1.033±0.060	1.935±0.236	2686
G13	41	2.158±0.240	1.018±0.096	1.651±0.254	2354
G22	82	2.270±0.236	0.985±0.077	1.817±0.245	3477
G23	56	1.894±0.264	1.075±0.115	1.254±0.292	1387

Table VII - Results of pionic 2p-1s width analysis for each B^{11} run. Number of degrees of freedom in each fit equals 48. Widths in keV.

RUN	χ^2	Γ_V	Γ_{instr}	Γ_{nat}	Total Counts
G4	51	2.298±0.270	1.093±0.058	1.749±0.280	1823
G11	67	2.420±0.223	1.093±0.068	1.899±0.232	6715
G14	60	2.269±0.253	1.104±0.035	1.701±0.261	5308

Table VIII - Results of pionic 2p-1s width analysis for each C^{12} run. Number of degrees of freedom in each fit equals 115. Widths in keV.

RUN	χ^2	Γ_V	Γ_{instr}	Γ_{nat}	Total Counts
G1	383	3.459±0.417	1.142±0.054	3.057±0.420	5451
G2	336	3.440±0.396	1.156±0.050	3.025±0.399	5475
G10	443	3.477±0.481	1.108±0.046	3.101±0.484	9071
K4	178	4.198±0.475	1.459±0.092	3.658±0.481	5730
K6	421	3.919±0.355	1.452±0.070	3.349±0.360	24182
K7	155	3.791±0.450	1.382±0.092	3.255±0.456	2948
K8	250	4.022±0.346	1.421±0.072	3.487±0.350	16071
K10	204	3.628±0.430	1.440±0.070	3.026±0.437	6818

Table IX - Results of pionic 2p-1s width analysis for each Li^6 run. Number of degrees of freedom in each fit equals 81. Widths in keV.

RUN	χ^2	Γ_v	Γ_{instr}	Γ_{nat}	Total Counts
A18	106	0.699±0.074	0.610±0.045	0.159±0.108	4882
A25	89	0.703±0.070	0.621±0.045	0.147±0.105	5268
A28	98	0.636±0.077	0.591±0.045	0.083±0.118	2636
A30	93	0.668±0.072	0.600±0.045	0.123±0.109	4194
A35	88	0.723±0.071	0.600±0.045	0.215±0.101	3958

Table X - Results of pionic 2p-1s width analysis for each Li^7 run. Number of degrees of freedom in each fit equals 81. Widths in keV.

RUN	χ^2	Γ_v	Γ_{instr}	Γ_{nat}	Total Counts
A17	88	0.682±0.064	0.621±0.045	0.111±0.101	6343
A23	112	0.717±0.075	0.610±0.045	0.189±0.107	2879
A27	78	0.688±0.076	0.562±0.045	0.219±0.105	3149
A29	114	0.748±0.072	0.607±0.045	0.244±0.100	3476
A33	107	0.702±0.072	0.610±0.045	0.164±0.106	4170

Table XI - Weighted average of widths obtained from separate runs for each element.

TARGET	Γ_{nat} (keV)	ω_{abs} (10^{18} sec^{-1})
Li^6	0.15 ± 0.05	0.23 ± 0.08
Li^7	0.19 ± 0.05	0.29 ± 0.08
Be^9	0.58 ± 0.05	0.88 ± 0.08
B^{10}	1.68 ± 0.12	2.55 ± 0.18
B^{11}	1.72 ± 0.15	2.61 ± 0.23
C^{12}	3.25 ± 0.15	4.94 ± 0.23

Table XII - Calculated values of 1s line widths using parameter β_{11}. Nuclear radii in units of F, widths in keV and ν(eff) in MeV F^6.

ELEMENT	RADIUS	Γ_{nat}(S.E.)	Γ_{nat}(pert.)	Γ_{nat}(exp)	Im $B_o(eff)_{exp}$	Im $B_o(eff)_{th}$	$\Delta B(A^{-1})$	$\nu(eff)_{th}$
Li^6	3.28±0.06 [53]	0.08	0.08	0.15±0.05	0.0363±0.0109	0.0185	0.0037	147
Li^7	3.09±0.04 [53]	0.12	0.13	0.19±0.05	0.0274±0.0072	0.0185	0.0037	147
Be^9	3.25±0.50 [54-56]	0.38	0.40	0.58±0.05	0.0263±0.0023	0.0176	0.0029	140
B^{10}	3.16±0.15 [57]	0.96	1.01	1.68±0.12	0.0299±0.0021	0.0173	0.0025	137
B^{11}	3.12±0.15 [57]	1.20	1.26	1.72±0.15	0.0243±0.0021	0.0171	0.0023	135
C^{12}	3.11±0.05 [58,59]	2.34	2.47	3.25±0.15	0.0227±0.0011	0.0165	0.0018	131

Table XIII - Calculated values of 1s line widths for parameter β_{11}. Nuclear radii in units of F, widths in keV and $\nu(\text{eff})$ in MeV F^6.

ELEMENT	RADIUS	$\Gamma_{nat}(S.E.)$	$\Gamma_{nat}(pert.)$	$\Gamma_{nat}(exp)$	Im $B_o(eff)_{exp}$	Im $B_o(eff)_{th}$	$\Delta B(A^{-1})$	$\nu(eff)_{th}$
Li^6	3.28	0.11	0.12	0.15±0.05	0.0363±0.0109	0.0278	0.0063	221
Li^7	3.09	0.18	0.19	0.19±0.05	0.0274±0.0072	0.0274	0.0059	217
Be^9	3.25	0.56	0.59	0.58±0.05	0.0263±0.0023	0.0258	0.0044	205
B^{10}	3.16	1.48	1.55	1.68±0.12	0.0299±0.0021	0.0265	0.0051	211
B^{11}	3.12	1.75	1.84	1.72±0.15	0.0243±0.0021	0.0249	0.0036	198
C^{12}	3.11	3.41	3.60	3.25±0.15	0.0227±0.0011	0.0240	0.0028	191

Table XIV - Summary of all 2p-1s line width measurements. Calculated widths Γ_{nat}(S.E.) are for β'_{11}. Radii in F and widths in keV.

ELEMENT	RADIUS	Γ_{nat}(W&M)	Γ_{nat}(Berkeley)	Γ_{nat}(CERN)	Γ_{nat}(S.E.)
He^4	2.07[60]	0.00±0.06[63]	—	—	0.06
Li^6	3.28	0.15±0.05	0.39±0.36	—	0.11
Li^7	3.09	0.19±0.05	0.57±0.30	—	0.18
Be^9	3.25	0.58±0.05	0.85±0.28	1.07±0.30	0.56
B^{10}	3.16	1.68±0.12	1.4±0.5	1.27±0.25	1.48
B^{11}	3.12	1.72±0.15	2.3±0.5	1.87±0.25	1.75
C^{12}	3.11	3.25±0.15	2.6±0.5	2.96±0.25	3.41
N^{14}	3.16[56]	—	4.1±0.4	4.48±0.30	6.72
O^{16}	3.42[58]	—	9.0±2.0	7.56±0.50	9.69
O^{18}	3.58[61]	—	—	8.67±0.70	10.57
F^{19}	3.68[62]	—	4.6±2.0	9.40±1.5	14.76
Na^{23}	3.79[62]	—	4.6±3.0	10.3±4.0	33.57
Mg^{24}	3.88[62]	—	—	—	41.80
Al^{27}	3.91[62]	—	—	—	63.73

VIII. ACKNOWLEDGMENTS

The author would like to acknowledge the following persons for their contributions and support:

Dr. Morton Eckhause, his advisor, for his continuous encouragement and aid during all phases of this research, and for his invaluable suggestions and guidance while the manuscript was being written.

Mr. William B. Shuler, his colleague in this experiment, with whom he worked in preparation for the experimental runs and in the taking of data.

Drs. Robert T. Siegel and Robert E. Welsh for their support, helpful advice, and careful reading of the manuscript.

Drs. Rolf G. Winter and David A. Jenkins for reading the manuscript.

Dr. Raymond W. Southworth for reading the manuscript and, as Director of the William and Mary Computer Center, for the support of his staff during all programming.

Dr. David K. Anderson for useful discussions and for bringing to his attention the recent cross section measurement by Rose.

Mr. W. Wade Sapp for aid tendered during the experimental run and Messrs. George H. Miller and Darrell G. Eisenhut for their help in computer programming and analysis of the data.

Mr. Stanley Hummel and the William and Mary Machine Shop staff for constructing much of the cryogenic hardware.

Dr. Roger B. Sutton and the Carnegie Mellon Nuclear Research Center for their hospitality.

His wife who patiently and carefully typed much of the manuscript.

The National Aeronautics and Space Administration for support through a predoctoral traineeship during the years 1966-68.

The research reported in this paper was supported in part by the National Aeronautics and Space Administration.

IX. APPENDICES

A. Evaluation of the convolution integral for two Gaussian functions.

The convolution integral for two normalized Gaussian functions is

$$f_G(Y) = (1/\sigma_1\sigma_2\ 2\pi)\int_{-\infty}^{\infty} e^{-(Y - x_2)^2/2\sigma_1^2} \cdot e^{-x_2^2/2\sigma_2^2} \cdot dx_2 \ .$$

The integrand reduces to

$$I \equiv e^{-Y^2/2\sigma_1^2} \cdot e^{[x_2Y/\sigma_1^2 - (\sigma_1^2 + \sigma_2^2)x_2^2/2\sigma_1^2\sigma_2^2]} \ .$$

The argument of the exponential term is a quadratic function of x_2 and may be written as a squared term by completing the square. The integrand then becomes

$$I = e^{-\alpha v^2} \cdot e^{-Y^2/2\sigma_1^2} \cdot e^{Y^2/2\sigma_1^2(\sigma_1^2 + \sigma_2^2)}$$

where

$$\alpha \equiv (\sigma_1^2 + \sigma_2^2)/2\sigma_1^2\sigma_2^2 \quad \text{and} \quad V \equiv x_2 - Y\sigma_2^2/(\sigma_1^2 + \sigma_2^2)$$

The integral is now in a form which can be evaluated directly; <u>i.e.</u>,

$$f_G(Y) = \frac{2e^{-Y^2/2(\sigma_1^2 + \sigma_2^2)}}{\sigma_1\sigma_2 2\pi} \int_0^{\infty} e^{-\alpha v^2}\, dv$$

$$f_G(Y) = \frac{e^{-Y^2/2\sigma^2}}{\sigma\sqrt{2\pi}}$$

where $\sigma^2 \equiv \sigma_1^2 + \sigma_2^2$

B. Evaluation of the convolution integral for two Lorentzian functions.

The convolution integral for two Lorentzian functions is

$$f_L(Y) = (A_1A_2/\pi^2) \int_{-\infty}^{\infty} \frac{dx}{[A_1^2 + x^2][A_2^2 + (Y - x)^2]}$$

By the method of partial fractions, the integrand can be written in the form

$$I \equiv \frac{ax + b}{A_1^2 + x^2} + \frac{cx + d}{A_2^2 + (Y - x)^2}$$

where $$a = \frac{2Y}{4Y^2A_1^2 + (A_2^2 + Y^2 - A_1^2)^2}$$

$$b = \frac{A_2^2 + Y^2 - A_1^2}{4Y^2A_1^2 + (A_2^2 + Y^2 - A_1^2)^2}$$

$$c = -a$$

$$d = \frac{4Y^2 - (A_2^2 + Y^2 - A_1^2)}{4Y^2A_1^2 + (A_2^2 + Y^2 - A_1^2)}$$

The integral can now be integrated directly and yields

$$f_L(Y) = (A_1A_2/\pi)[b/A_1 + cY/A_2 + d/A_2].$$

With constants b, c, and d substituted and after some algebra, $f_L(Y)$ reduces to

$$f_L(Y) = \frac{k/\pi}{k^2 + Y^2}$$

where $k = A_1 + A_2$.

C. Calculation of A^{-1} corrections.

A formula has been given by the Ericsons[19] for calculating the A^{-1} corrections in the s-wave scattering operator for two free nucleons:

$$\Delta B(A^{-1}) = \left[\frac{4S(S+1)}{A} - 3\right]\frac{B_1}{A-1} + \left[\frac{4T(T+1)}{A} - 3\right]\frac{B_2}{A-1}$$
$$+ \left[\frac{4S(S+1)}{A} - 3\right]\left[\frac{4T(T+1)}{A} - 3\right]\frac{B_4}{(A-1)^2}$$
$$- \left[1 + \frac{3}{A-1} - \frac{4S(S+1)}{A(A-1)}\right]\frac{4B_5}{A-1}$$
$$+ \left[1 + \frac{3}{A-1} - \frac{4S(S+1)}{A(A-1)}\right]\frac{4(\vec{t}\cdot\vec{T})(B_3+B_5)}{A}$$
$$+ \left[1 + \frac{3}{A-1} - \frac{4S(S+1)}{A(A-1)}\right]\frac{8(\vec{t}\cdot\vec{T})^2 B_5}{A(A-1)}$$

where $\mathrm{Im}\, B_1 = (1/16)\ \mathrm{Im}(\beta_{11} - \beta_{01})$

$\mathrm{Im}\, B_2 = (1/16)\ \mathrm{Im}(-3\beta_{11} + \beta_{01})$

$\mathrm{Im}\, B_3 = (1/16)\ \mathrm{Im}\, \beta_{01}$

$\mathrm{Im}\, B_4 = (-1/16)\ \mathrm{Im}(\beta_{11} + \beta_{01})$

$\mathrm{Im}\, B_5 = (-1/32)\ \mathrm{Im}\, \beta_{01}$

and S = nuclear ground state spin quantum number

T = nuclear ground state isospin quantum number

$\vec{t}$ = pion isospin

$\vec{t}\cdot\vec{T} = \frac{N-Z}{2}$.

X. LIST OF REFERENCES

1. H. Yukawa, Proc. Phys. - Math Soc. Japan 17, 48 (1935).

2. S. H. Neddermeyer and C. D. Anderson, Phys. Rev. 54, 88 (1938).

3. M. Conversi, E. Pancini, and O. Piccioni, Phys. Rev. 71, 209 (1947).

4. C. M. G. Lattes, H. Muirhead, G. P. S. Occhialini, and C. F. Powell, Nature 159, 694 (1947).

5. E. Fermi, E. Teller, and V. Weisskopf, Phys. Rev. 71, 314 (1947).

6. E. Fermi and E. Teller, Phys. Rev. 72, 399 (1947).

7. M. Camac, A. D. McGuire, J. B. Platt, and H. J. Shulte, Phys. Rev. 88, 1934 (1952).

8. J. A. Wheeler, Phys. Rev. 21, 133 (1949).

9. A. B. Mickelwait and H. C. Corben, Phys. Rev. 96, 1145 (1954).

10. S. DeBenedetti, M. Stearns, M. B. Stearns, and L. Leipuner, Phys. Rev. 95, 1353 (1954a).

11. S. DeBenedetti, M. Stearns, M. B. Stearns, and L. Leipuner, Phys. Rev. 96, 804 (1954b).

12. D. West and E. F. Bradley, Phil. Mag. (Ser. 8) 1, 97 (1956).

13. D. West and E. F. Bradley, Phil. Mag. (Ser. 8) 2, 957 (1957).

14. M. Camac, M. L. Halbert, and J. B. Platt, Phys. Rev. 99, 905 (1955).

15. M. Stearns and M. B. Stearns, Phys. Rev. 103, 1534 (1956); Ibid. 105, 1573 (1957a); Ibid. 107, 1709 (1957b).

16. K. A. Brueckner, Phys. Rev. 98, 769 (1955).

17. S. Deser, M. L. Goldberger, K. Bauman, and W. Thirring, Phys. Rev. 96, 774 (1954).

18. D. West, Repts. Progr. Phys. 21, 271 (1958).

19. M. Ericson and T. E. O. Ericson, An. Phys. 36, 323 (1966).

20. D. A. Jenkins and R. Kunselman, Phys. Rev. Letters 17, 1148 (1966).

21. G. Backenstoss, S. Charalambus, H. Daniel, H. Koch, G. Poelz, H. Schmitt, and L. Tauscher, Phys. Letters 25B, 365 (1967).

22. H. A. Bethe and E. E. Salpeter, Quantum Mechanics of One- and Two-Electron Atoms; Academic Press (1957).

23. K. A. Brueckner, R. Serber, and K. M. Watson, Phys. Rev. 84, 258 (1951).

24. D. A. Jenkins, R. Kunselman, M. K. Simmons, and T. Yamazoki, Phys. Rev. Letters 17, 1 (1966).

25. L. Kisslinger, Phys. Rev. 98, 761 (1955).

26. M. Ericson, Compt. rend. 257, 3831 (1963).

27. M. Ericson, Compt. rend. 258, 1471 (1964).

28. W. J. Price, Nuclear Radiation Detection, McGraw Hill Book Co. New York, 2nd ed. (1964). See also G. T. Ewan and A. J. Tavendale, Can. J. Phys. 42, 2286 (1964).

29. U. Fano, Phys. Rev. 72, 26 (1947).

30. R. L. Heath, W. W. Black, and J. E. Cline, IEEE Trans. Nucl. Sci. NS-13, 445 (1966).

31. E. Fairstein and J. Hahn, Nucleonics 23, 56 (1965).

32. K. F. Smith and J. E. Kline, IEEE Trans. Nucl. Sci. NS-13, 468 (1966).

33. T. V. Blalock, Ibid. 468.

34. E. Elad and M. Nakamura, Nucl. Instr. and Methods 42, 315 (1966).

35. E. Fairstein, IRE Trans. on Nucl. Sci. NS-8, 129 (1961).

36. A. M. R. Ferrari, Nucl. Instr. and Methods 52, 179 (1967).

37. R. J. Harris, Jr. and W. B. Shuler, Nucl. Instr. and Methods 51, 351 (1967). See also R. J. Harris, Jr., William and Mary Report 8 (1967) for a description of the Ge(Li) spectrometer.

38. M. H. Foss, Conference on High Energy Cyclotron Improvement at the College of William and Mary, p. 85 (1964).

39. M. H. Foss, R. W. Findley and A. Suzuki, Nucl. Instr. and Methods 29, 282 (1964).

40. P. B. Day, Phys. Rev. 97, 689 (1955).

41. E. J. Seppi, H. Henrikson, F. Boehm, and J. W. M. DuMond, Nucl. Instr. and Methods 16, 17 (1962).

42. J. E. Freund, Mathematical Statistics, Prentice-Hall, Inc. Englewood Cliffs, N. J. (1964).

43. H. C. van de Hulst and J. M. Reesinck, Ap. J. 106, 121 (1947).

44. J. Tudor Davies and J. M. Vaughan, Ap. J. 137, 1302 (1963).

45. Y. Beers, Introduction to the Theory of Error, Addison-Wesley Pub. Co., Inc. Cambridge, Mass. (1953).

46. C. W. Allen, Astrophysical Quantities, The Athlone Press, The University of London, London, England, 2nd. ed. p. 82 (1963).

47. Precision pulser on loan from J. Biggerstaff, Oak Ridge National Laboratory, Oak Ridge, Tenn.

48. Ryoichi Seki and Alan H. Cromer, Phys. Rev. 156, 93 (1967). See also L. P. Fulcher, J. M. Eisenberg and J. LeTourneux, Can. J. Phys. 45, 3313 (1967).

49. R. A. Stallwood, R. B. Sutton, T. H. Fields, J. G. Fox and J. A. Kane, Phys. Rev. 109, 1716 (1958).

50. F. S. Crawford, Jr. and M. L. Stevenson, Phys. Rev. 97, 1305 (1955).

51. Carl M. Rose, Jr., Phys. Rev. 154, 1305 (1967).

52. S. Osaki et.al., Phys. Rev. Letters 4, 533 (1960).

P. M. Hattersley, H. Muirhead and J. N. Woulds, Nuclear Physics 67, 309 (1965).

M. E. Norberg, Jr., K. F. Kinsey and R. L. Burman, Phys. Rev. (to be published)

53. L. R. Suelze, M. R. Yearian, and Hall Crannell, Phys. Rev. 162, 992 (1967).

54. R. Hofstadter, Rev. Modern Phys. 28, 214 (1956); private communication from J. F. Streib.

55. R. Hofstadter, Ann. Rev. Nucl. Sci. 7, 231 (1957).

56. U. Meyer,Berkhout, K. W. Ford, and A. E. S. Green, Ann. Phys. 8, 119 (1959).

57. T. Stovall, J. Goldemberg, and D. B. Isabelle, Nucl. Phys. 86, 225 (1966).

58. H. Crannell, Phys. Rev. 148, 1107 (1966).

59. R. Engfer and D. Turck, Z. Physik 205, 60 (1967).

60. L. R. B. Elton, Nuclear Sizes, Oxford University Press, London (1961).

61. G. R. Bishop, Nucl. Phys. 41, 118 (1963).

62. G. Backenstoss et.al., Phys. Letters 25B, 547 (1967).

63. R. J. Wetmore, D. C. Buckle, J. R. Kane and R. T. Siegel, Phys. Rev. Letters 19, 1003 (1967).

XI. FIGURES

FIGURES

1. Schematic of Ge(Li) detector (from A. J. Tavendale, ref. 28).

2a. Voltage-sensitive preamplifier configuration.

2b. Charge-sensitive preamplifier configuration (from E. Fairstein, ref. 35).

3. Typical room-temperature FET preamplifier.

4. a-d: Four first-stage preamplifier configurations studied using TC-130.

5. Negative high voltage configuration [Si(Li)].

6. Positive high voltage configuration [Ge(Li)].

7. Co^{60} spectrum measured with Ge(Li) detector.

8. Co^{57} spectrum measured with Ge(Li) detector.

9. Am^{241} spectrum measured with Si(Li) detector.

10. Co^{57} spectrum measured with Si(Li) detector.

11. Counter array.

12. Differential range curve taken at CMU for pions stopping in 1/2" thick C^{12} target.

13. Differential range curve taken at SREL for pions stopping in 1" thick C^{12} target.

14. Block diagram of circuitry.

15a. Sketch of timing-analyzer display for "fast" and "slow" pulses out of time by T.

15b. Sketch of timing-analyzer display for "fast" and "slow" pulses in coincidence.

FIGURES

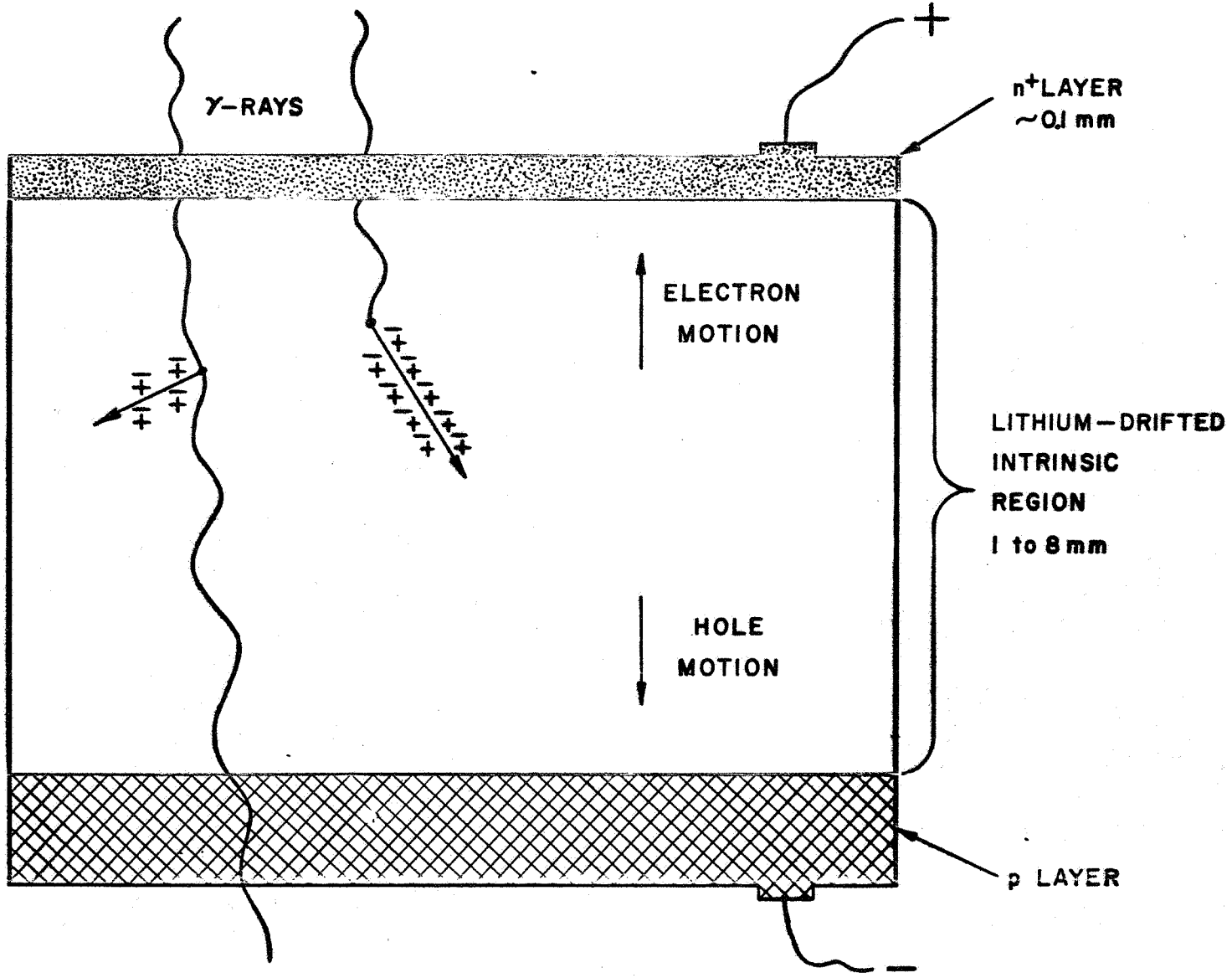
γ-RAYS
+
n+LAYER
~0.1 mm
ELECTRON
MOTION
LITHIUM-DRIFTED
INTRINSIC
REGION
1 to 8 mm
HOLE
MOTION
p LAYER
−

FIG. 1

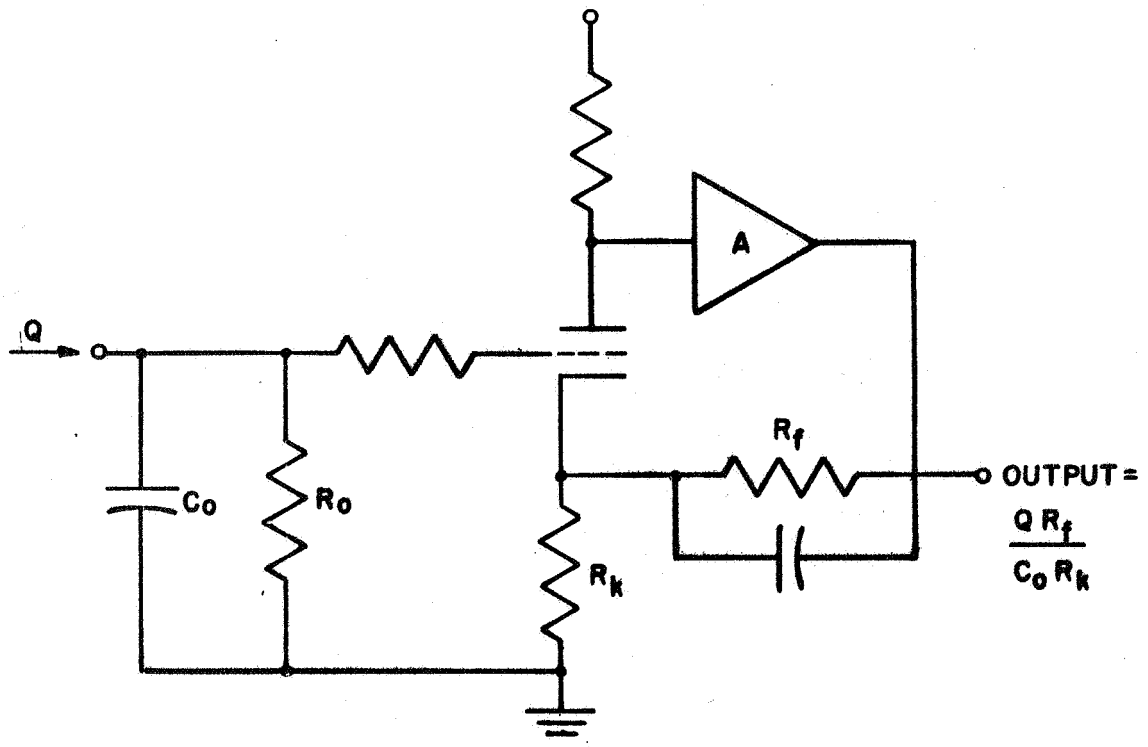

FIG. 2a

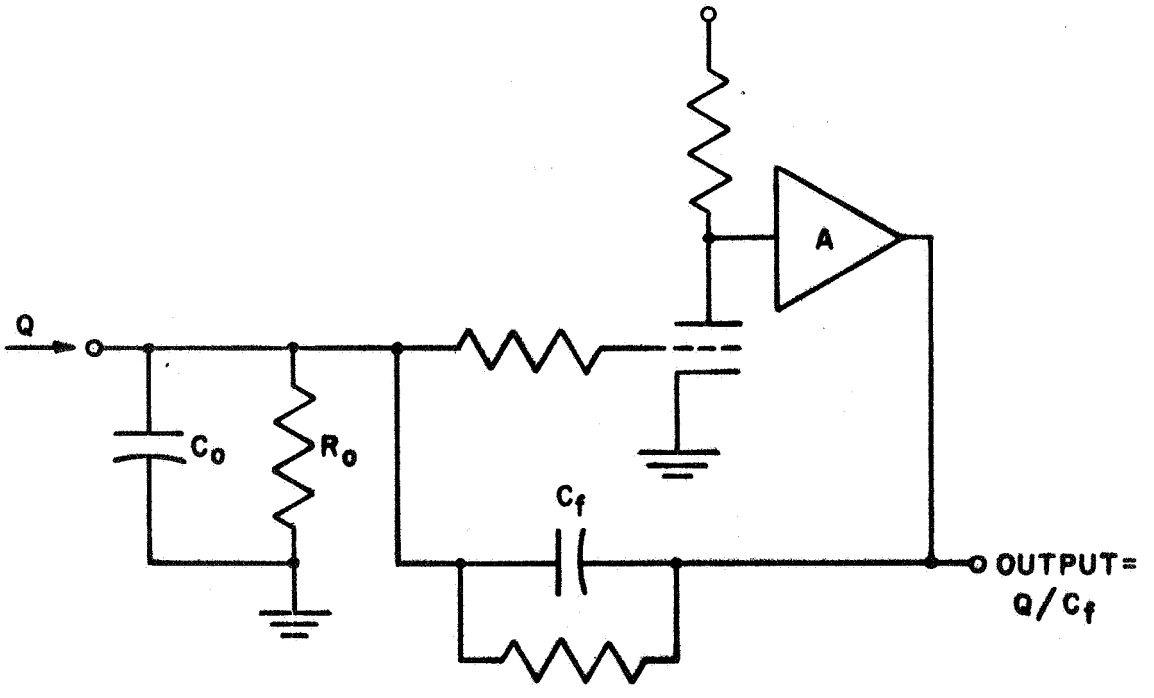

FIG. 2b

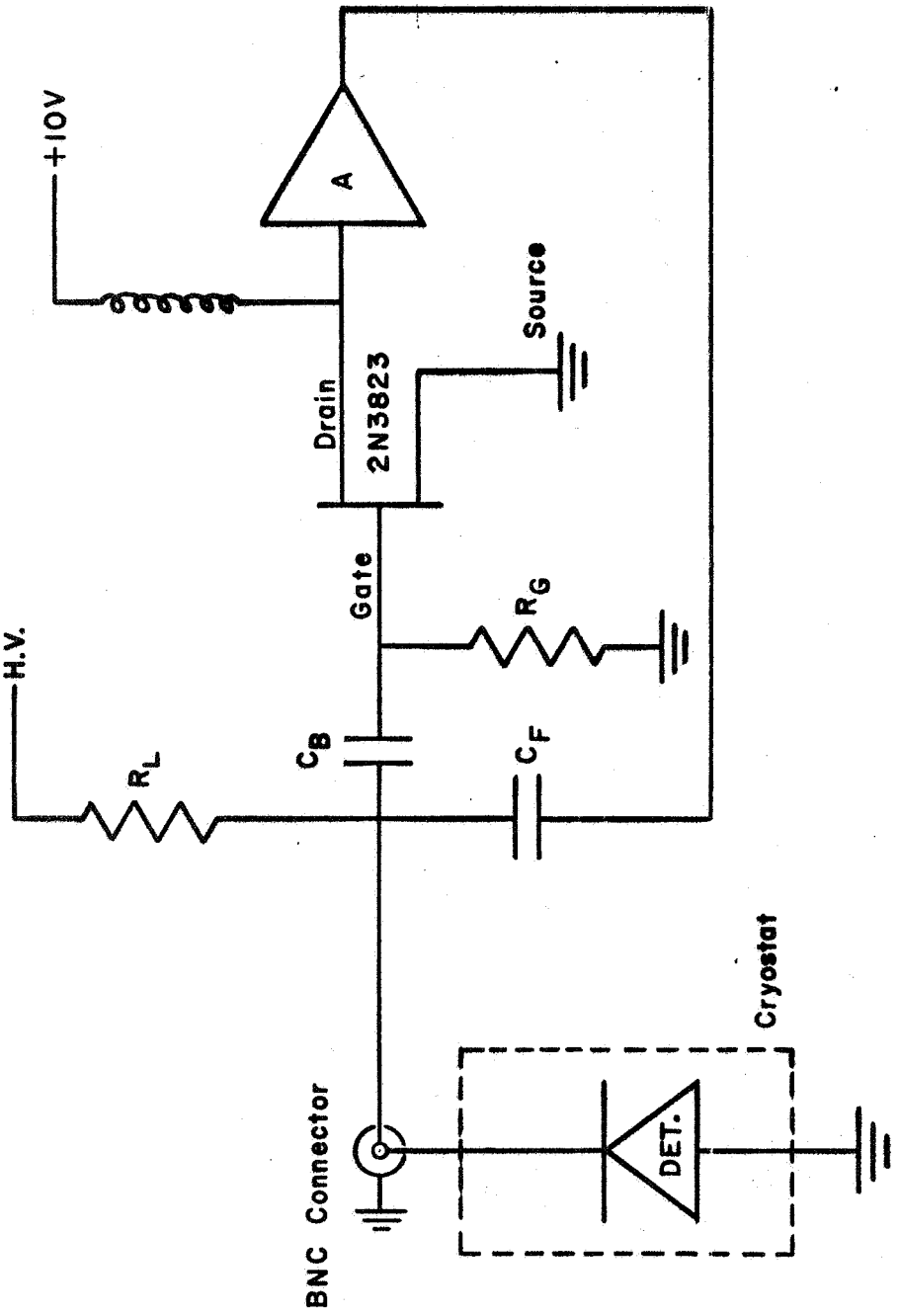
+10V
A
Source
Drain
2N3823
Gate
R_G
H.V.
C_B
C_F
R_L
Cryostat
BNC Connector
DET.

FIG. 3

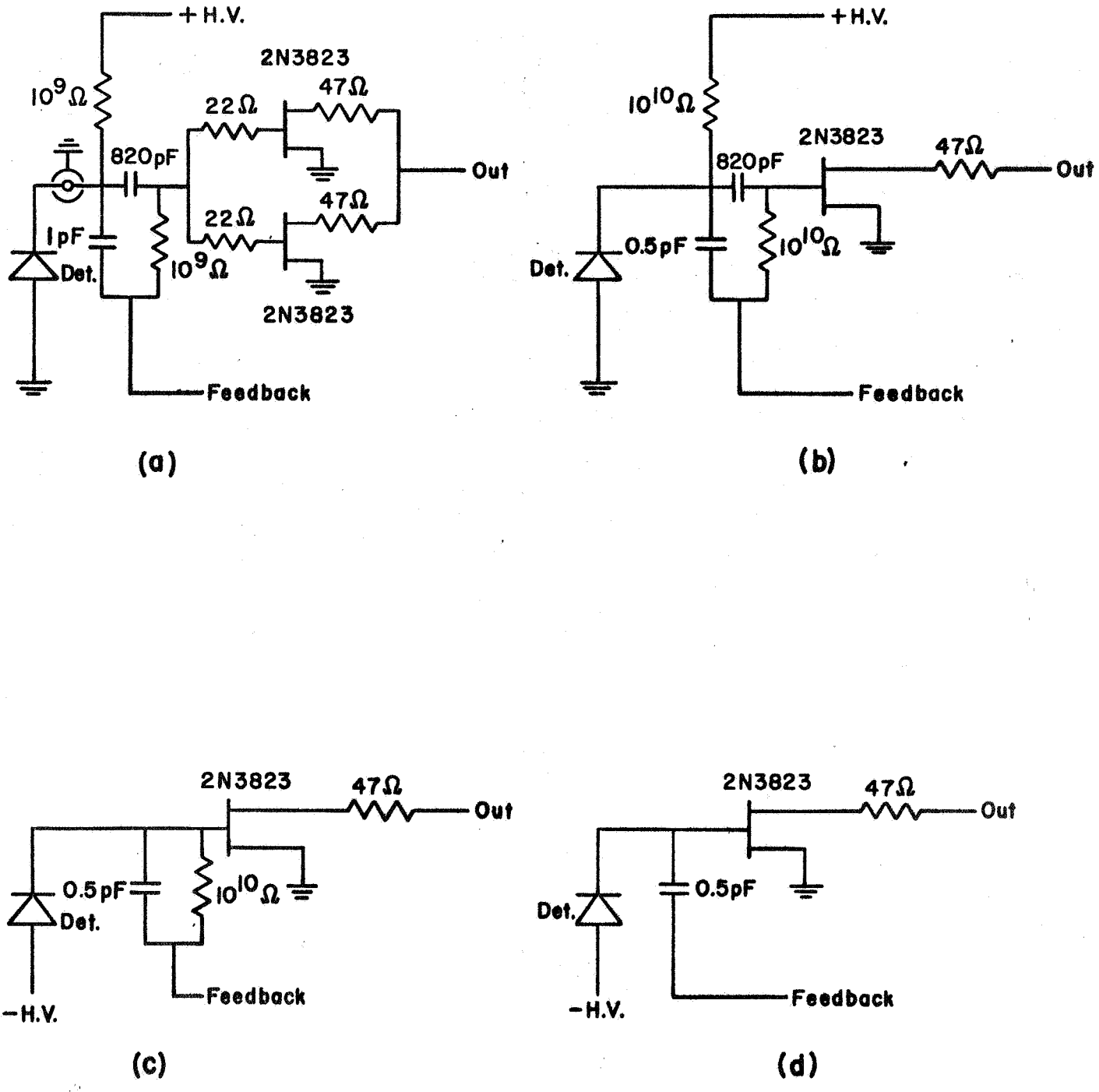
+H.V.
$10^9\Omega$
2N3823
47Ω
22Ω
820pF
Out
47Ω
22Ω
1pF
Det.
$10^9\Omega$
2N3823
Feedback
(a)
+H.V.
$10^{10}\Omega$
2N3823
47Ω
820pF
Out
0.5pF
Det.
$10^{10}\Omega$
Feedback
(b)
2N3823
47Ω
Out
0.5pF
Det.
$10^{10}\Omega$
Feedback
−H.V.
(c)
2N3823
47Ω
Out
Det.
0.5pF
Feedback
−H.V.
(d)

FIG. 4

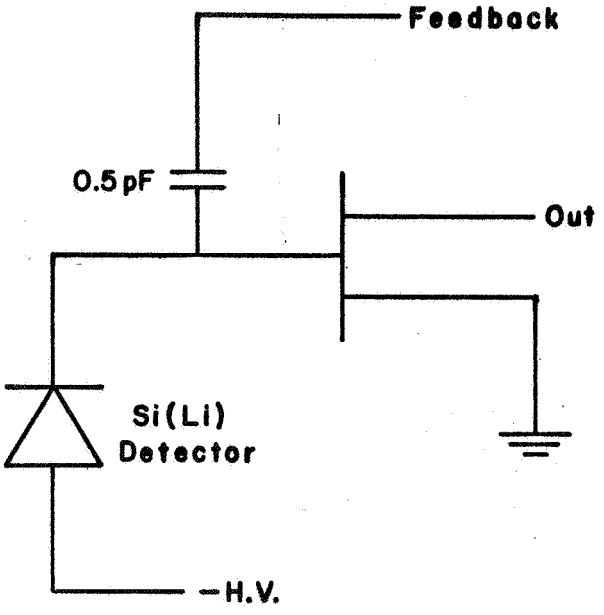
Feedback
0.5pF
Out
Si(Li)
Detector
-H.V.

FIG. 5

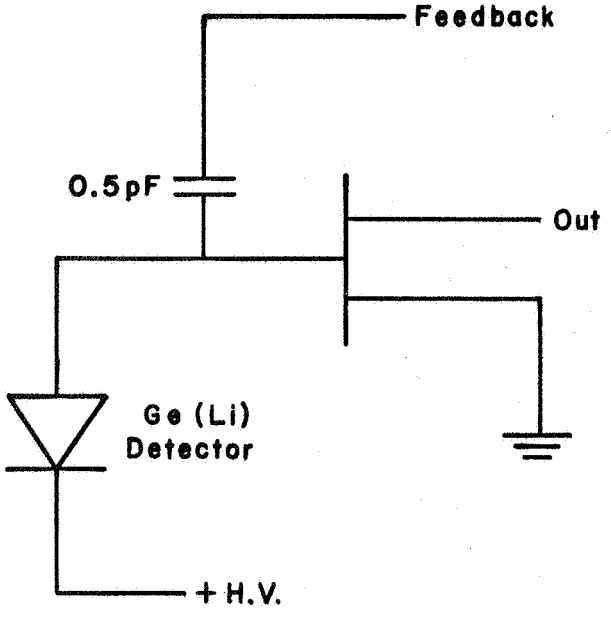
Feedback
0.5pF
Out
Ge (Li)
Detector
+H.V.

FIG. 6

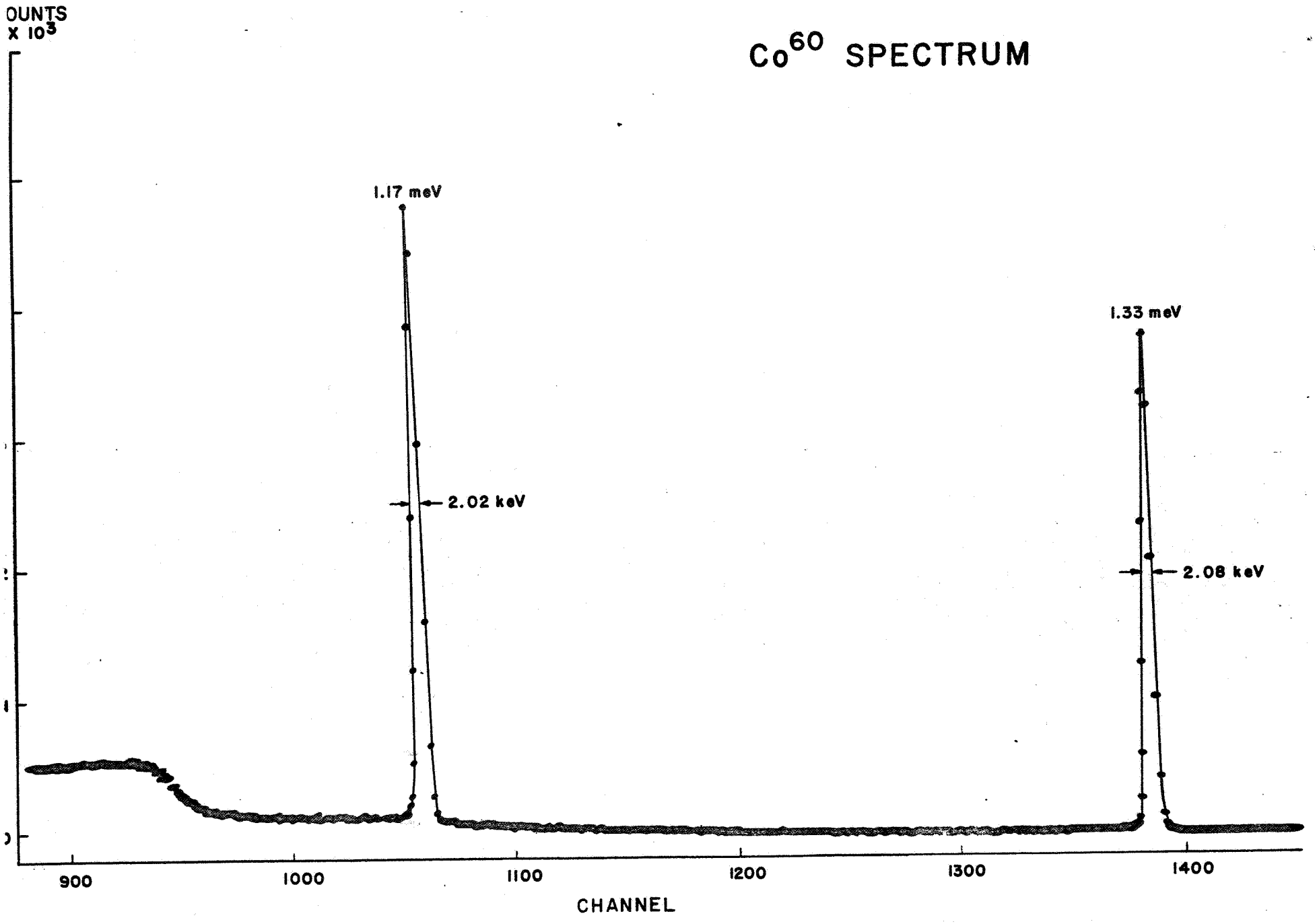
OUNTS
X 10³
Co⁶⁰ SPECTRUM
1.17 meV
2.02 keV
1.33 meV
2.08 keV
900
1000
1100
1200
1300
1400
CHANNEL

FIG. 7

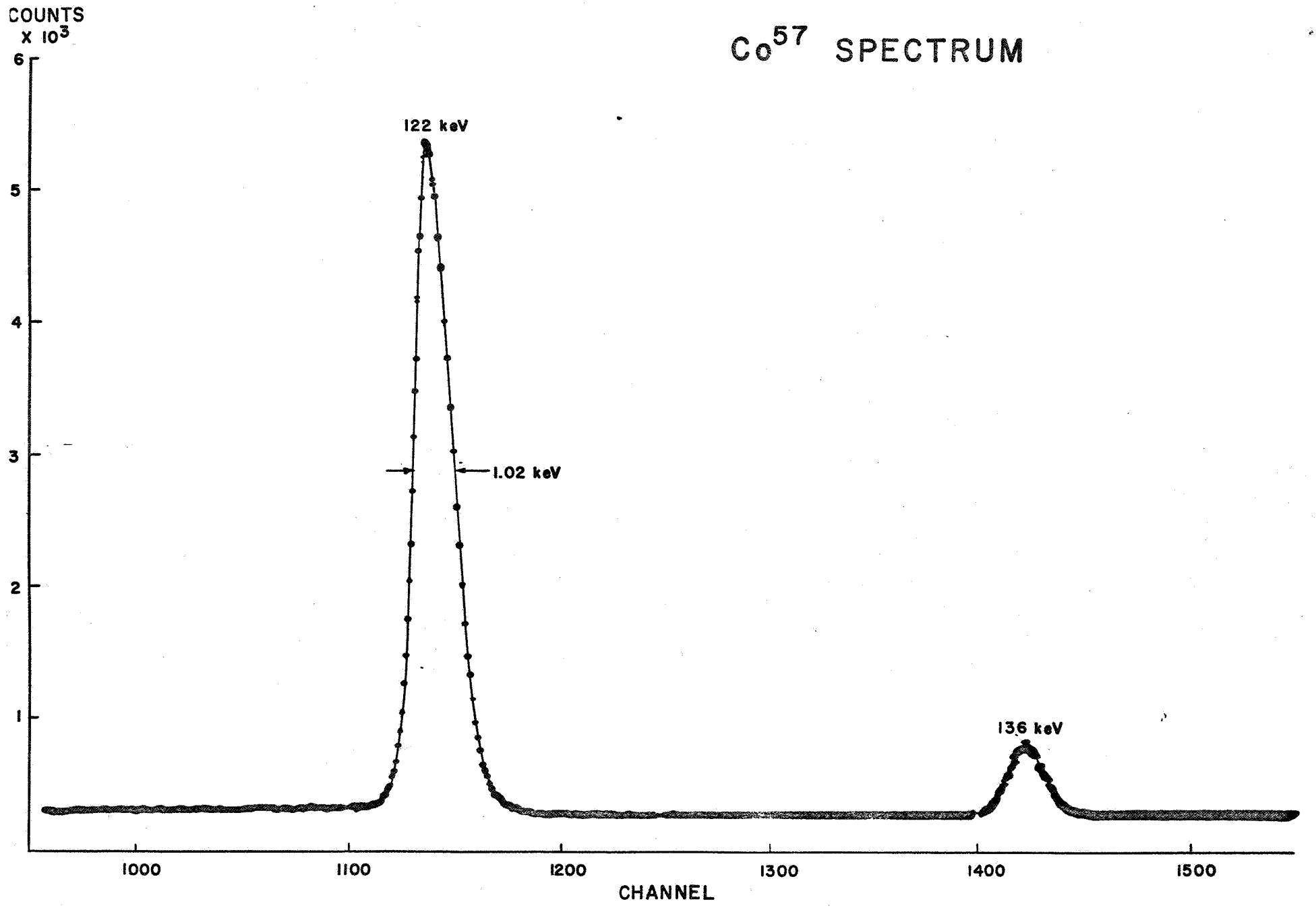
COUNTS
X 10³
6
5
4
3
2
1
Co⁵⁷ SPECTRUM
122 keV
1.02 keV
136 keV
1000
1100
1200
1300
1400
1500
CHANNEL

FIG. 8

Am^{241} SPECTRUM

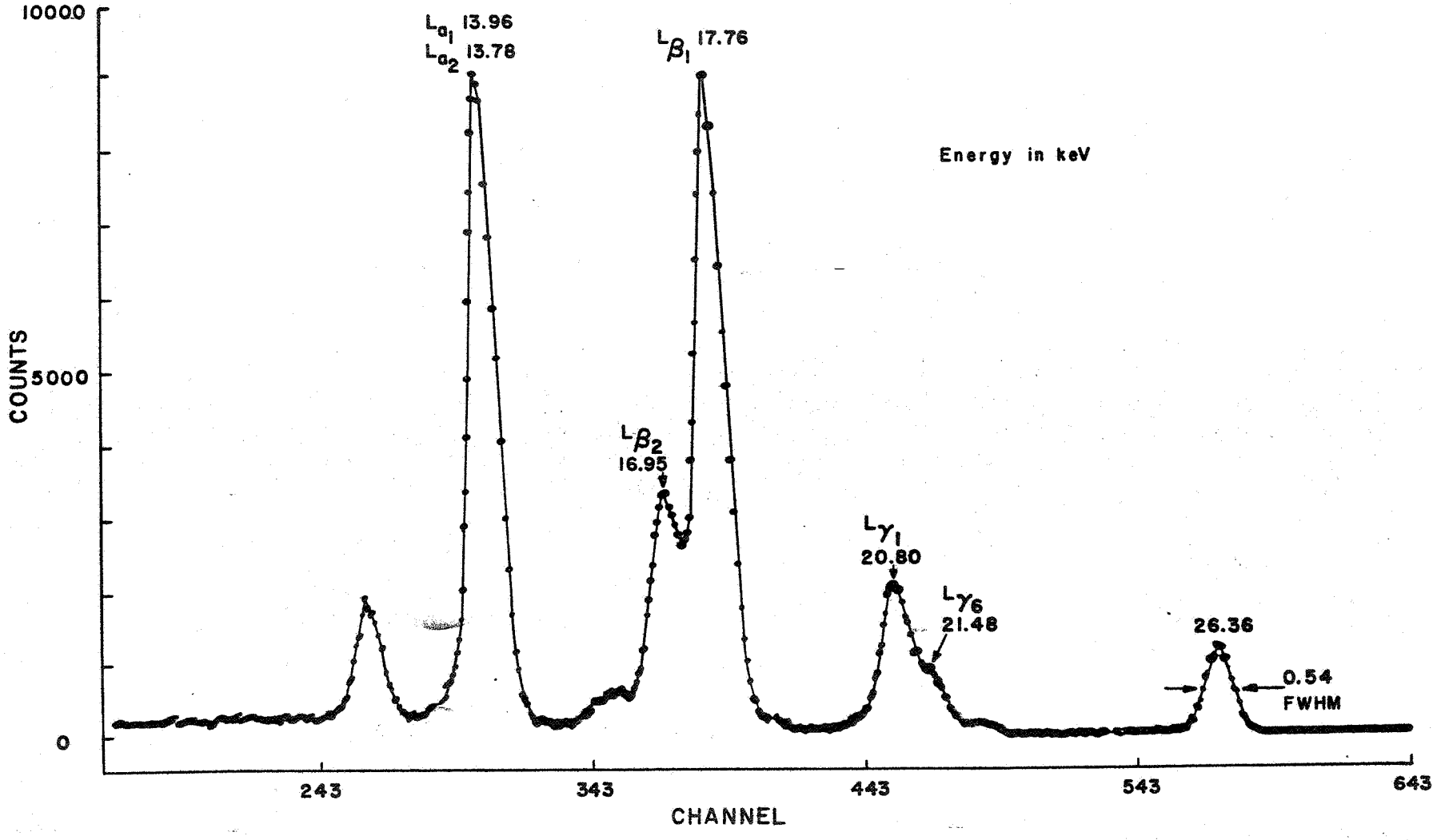

FIG. 9

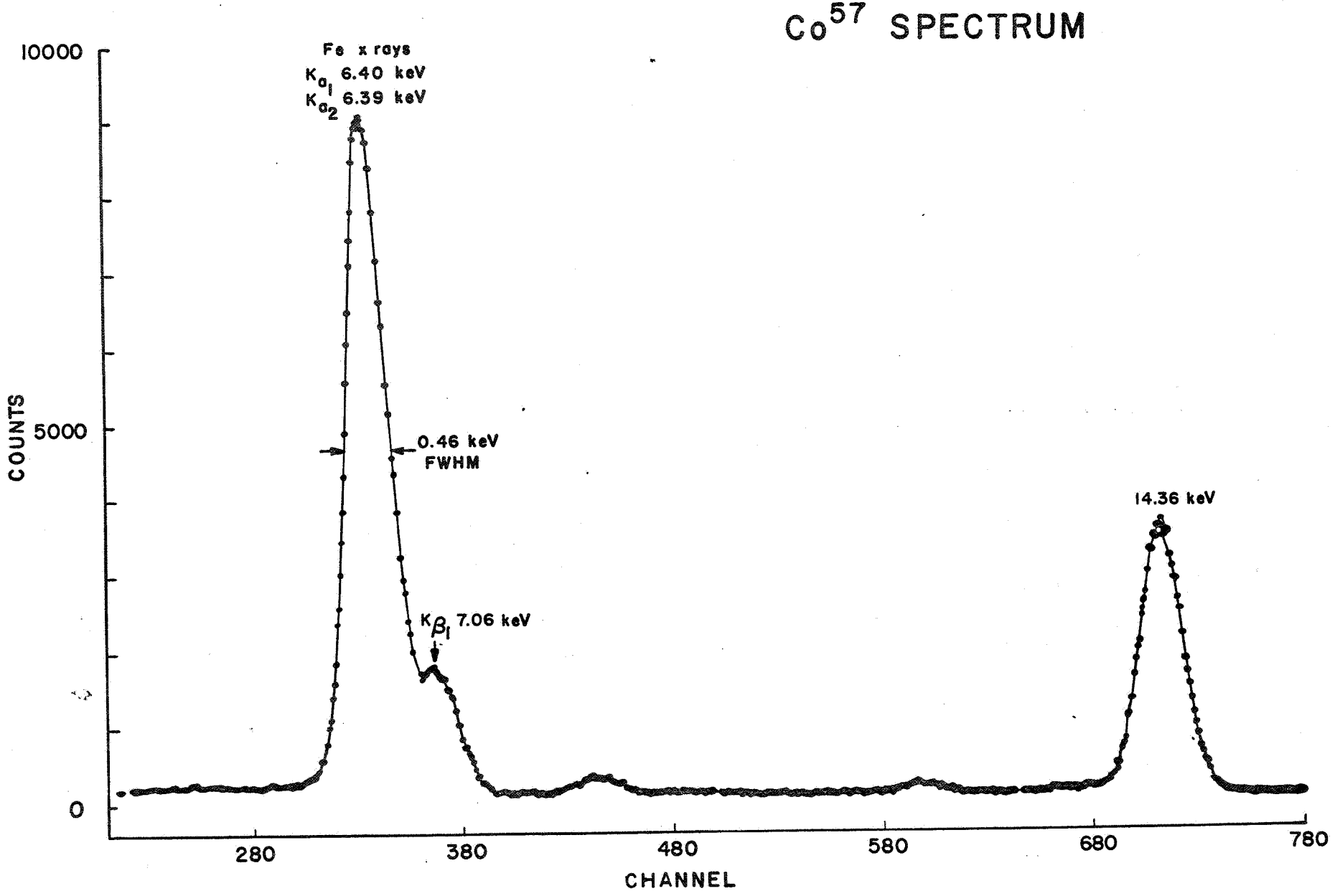
Co57 SPECTRUM
Fe x rays
Ka1 6.40 keV
Ka2 6.39 keV
0.46 keV
FWHM
Kβ1 7.06 keV
14.36 keV
10000
5000
0
COUNTS
280
380
480
580
680
780
CHANNEL

FIG. 10

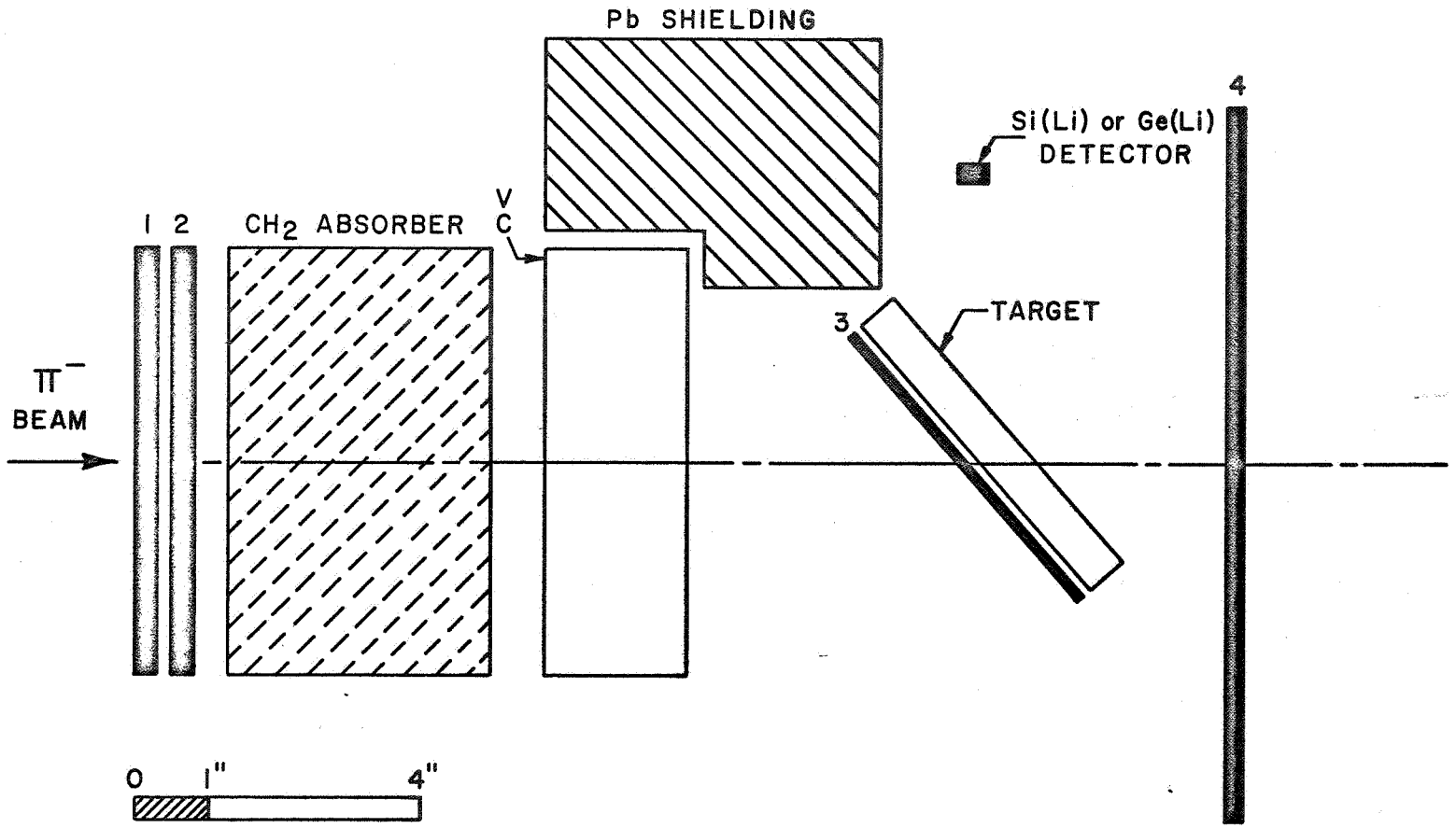
Pb SHIELDING
4
Si(Li) or Ge(Li)
DETECTOR
1 2
CH_2 ABSORBER
V
C
TARGET
3
π^-
BEAM
0
1"
4"

FIG. 11

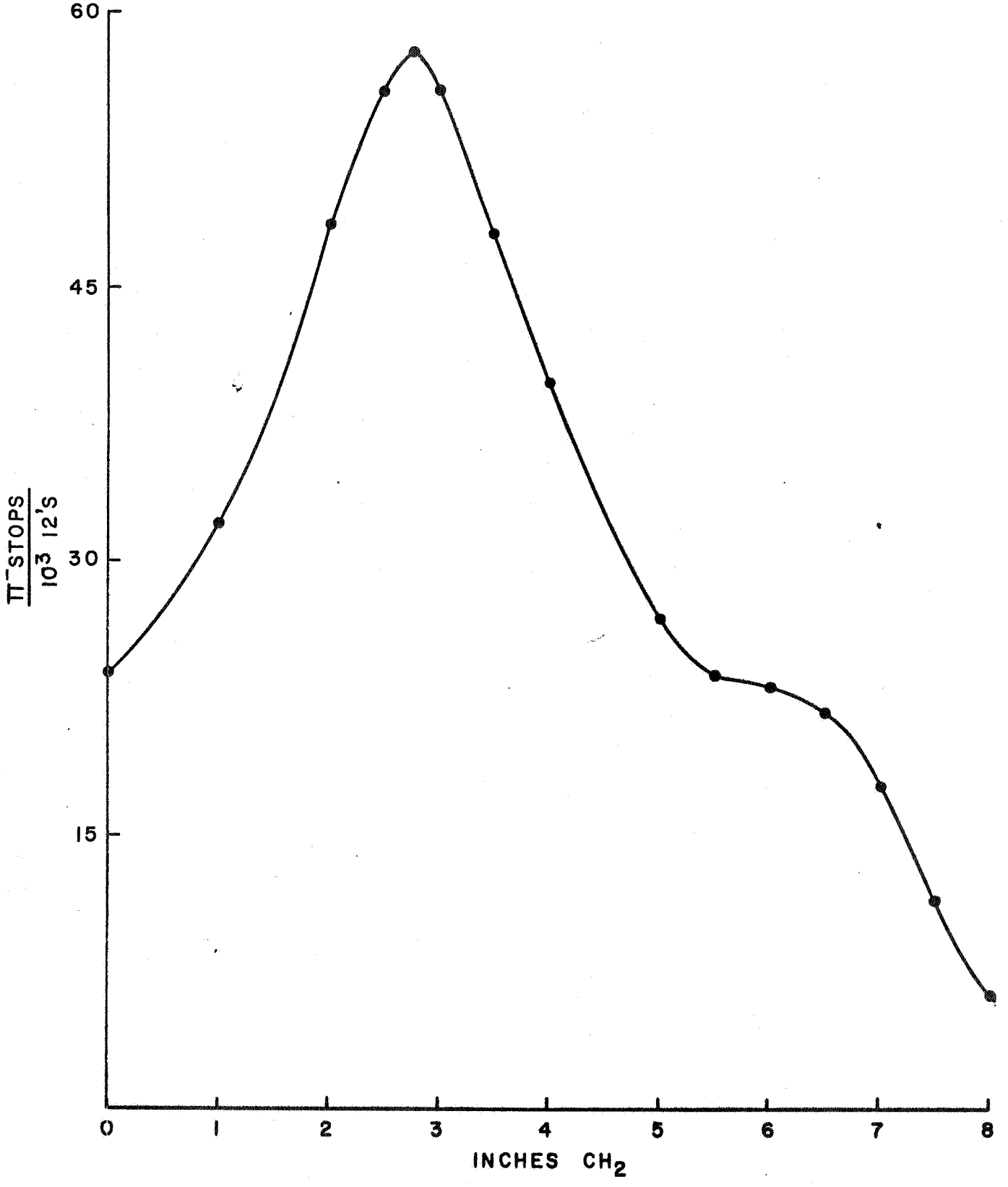
60
45
30
15
$\frac{\pi^- \text{STOPS}}{10^3\ 12\text{'S}}$
0
1
2
3
4
5
6
7
8
INCHES CH_2

FIG. 12

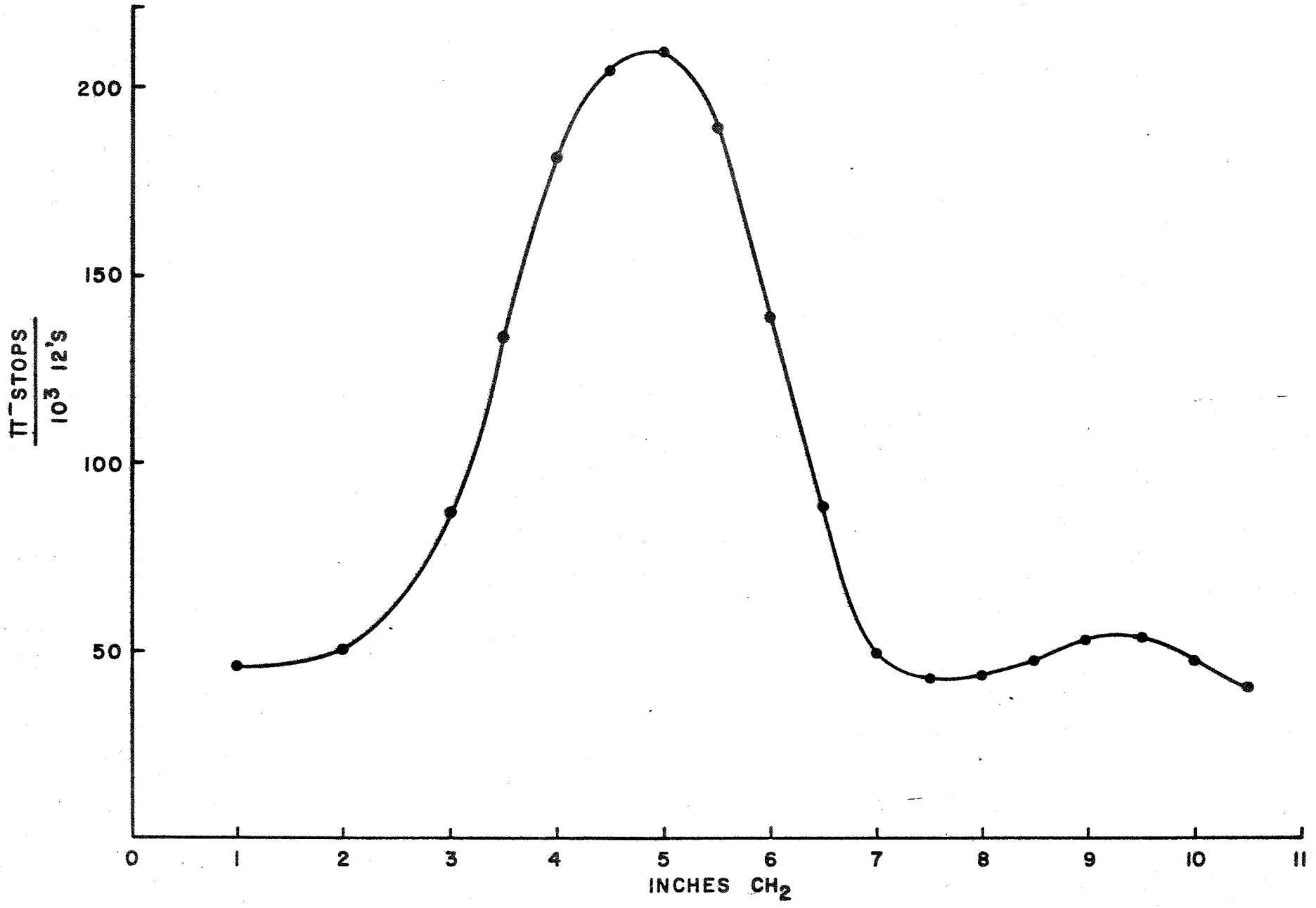
200
150
100
50
$\frac{\pi^- \text{STOPS}}{10^3\ 12\text{'S}}$
0
1
2
3
4
5
6
7
8
9
10
11
INCHES CH_2

FIG. 13

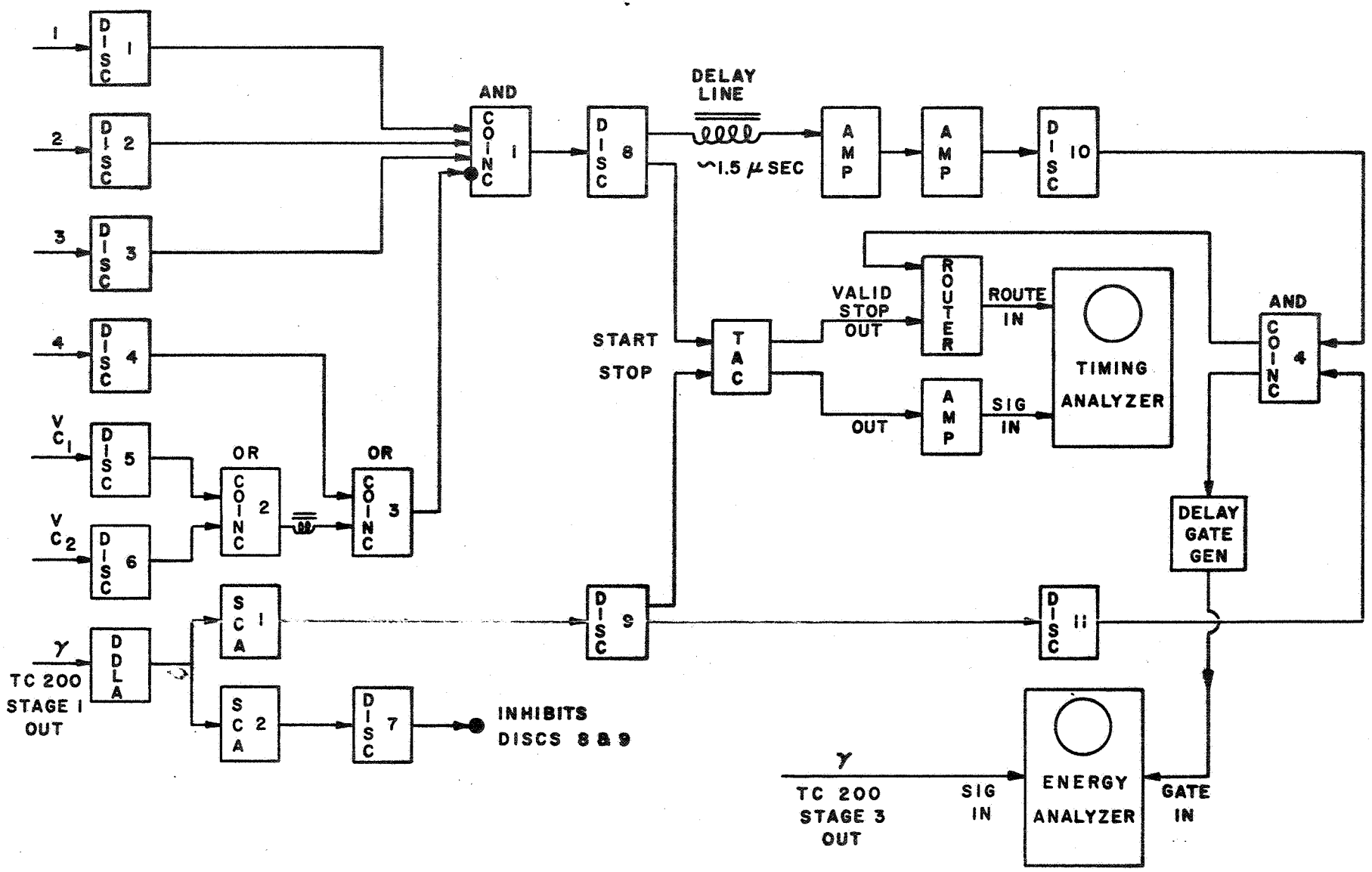
1
DISC 1
2
DISC 2
3
DISC 3
4
DISC 4
VC1
DISC 5
VC2
DISC 6
γ
TC 200
STAGE 1
OUT
DDLA
OR
COINC 2
OR
COINC 3
AND
COINC 1
SCA 1
SCA 2
DISC 7
INHIBITS
DISCS 8 & 9
DISC 8
DELAY
LINE
~1.5 μ SEC
AMP
AMP
DISC 10
START
STOP
TAC
VALID
STOP
OUT
ROUTER
ROUTE
IN
TIMING
ANALYZER
OUT
AMP
SIG
IN
AND
COINC 4
DISC 9
DISC 11
DELAY
GATE
GEN
γ
TC 200
STAGE 3
OUT
SIG
IN
ENERGY
ANALYZER
GATE
IN

FIG. 14

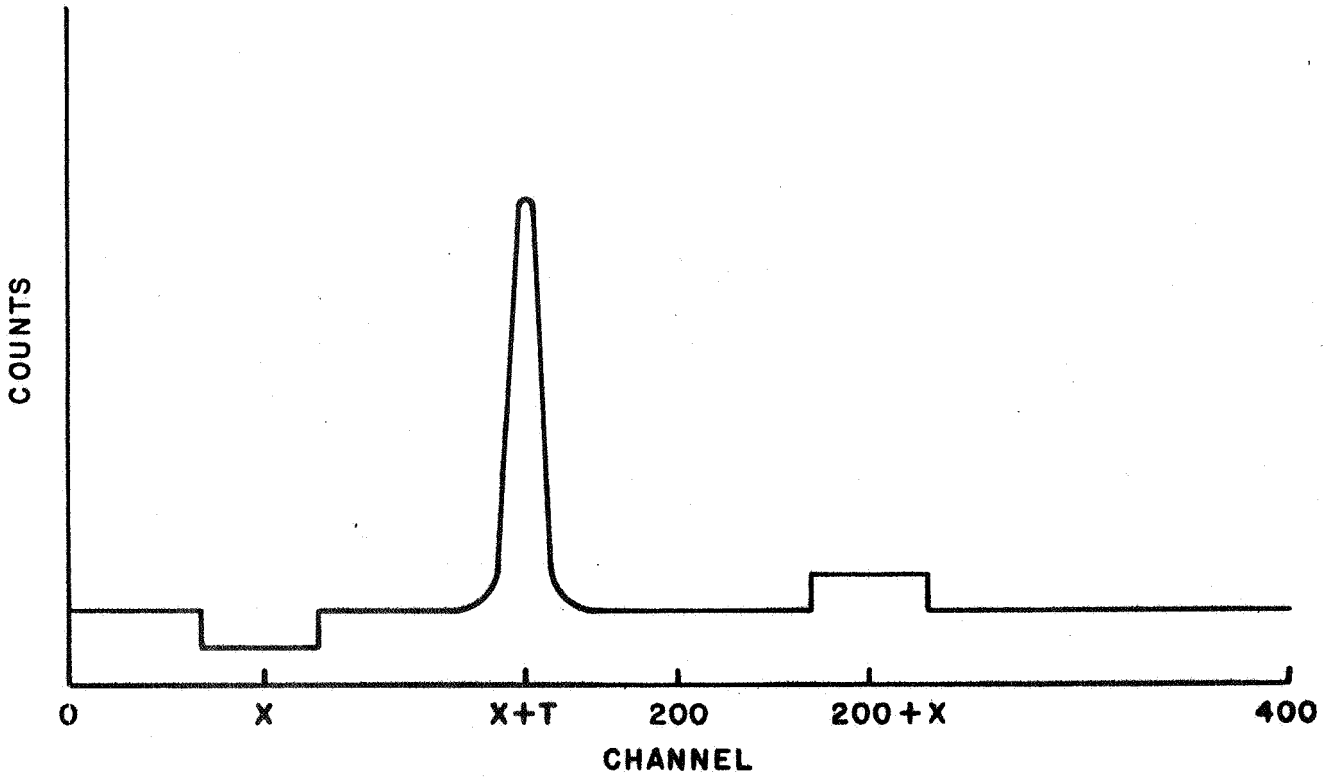

FIG. 15a

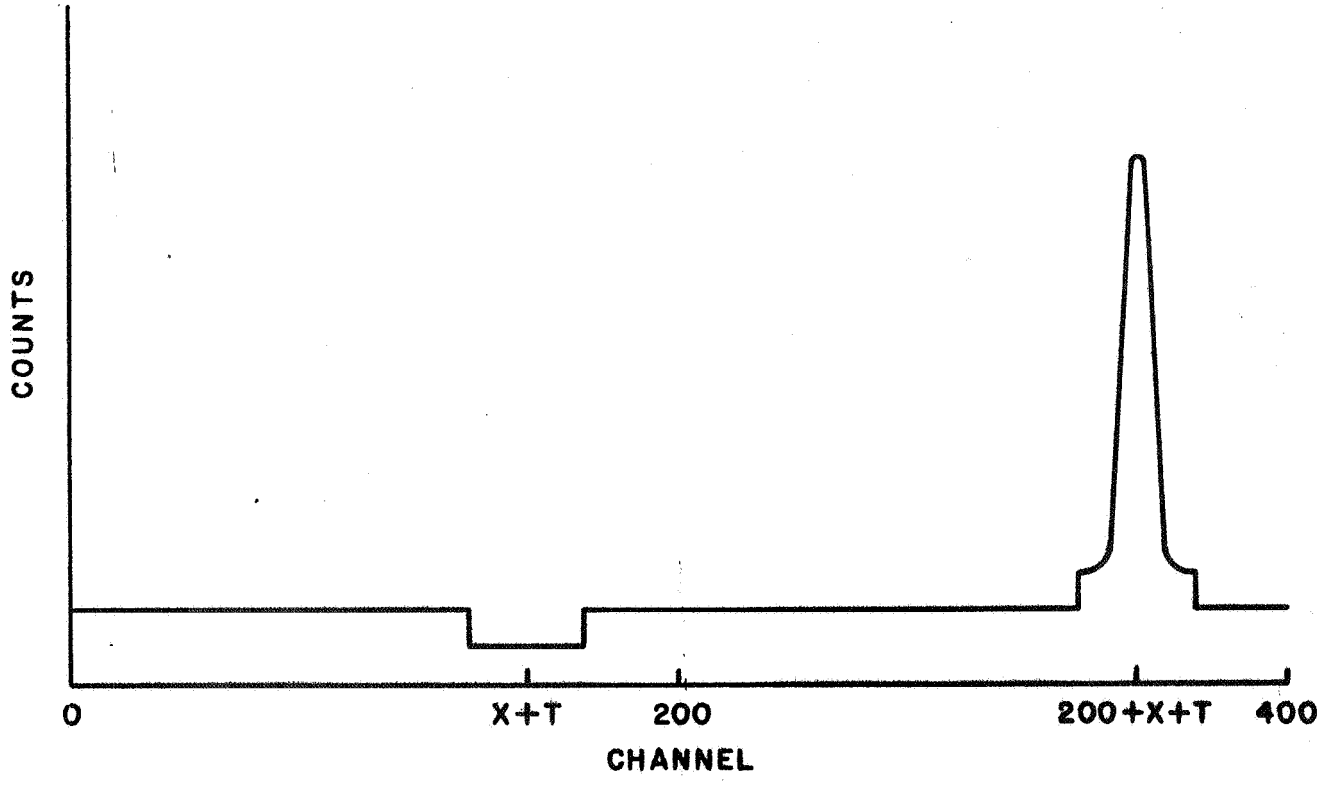

FIG. 15b

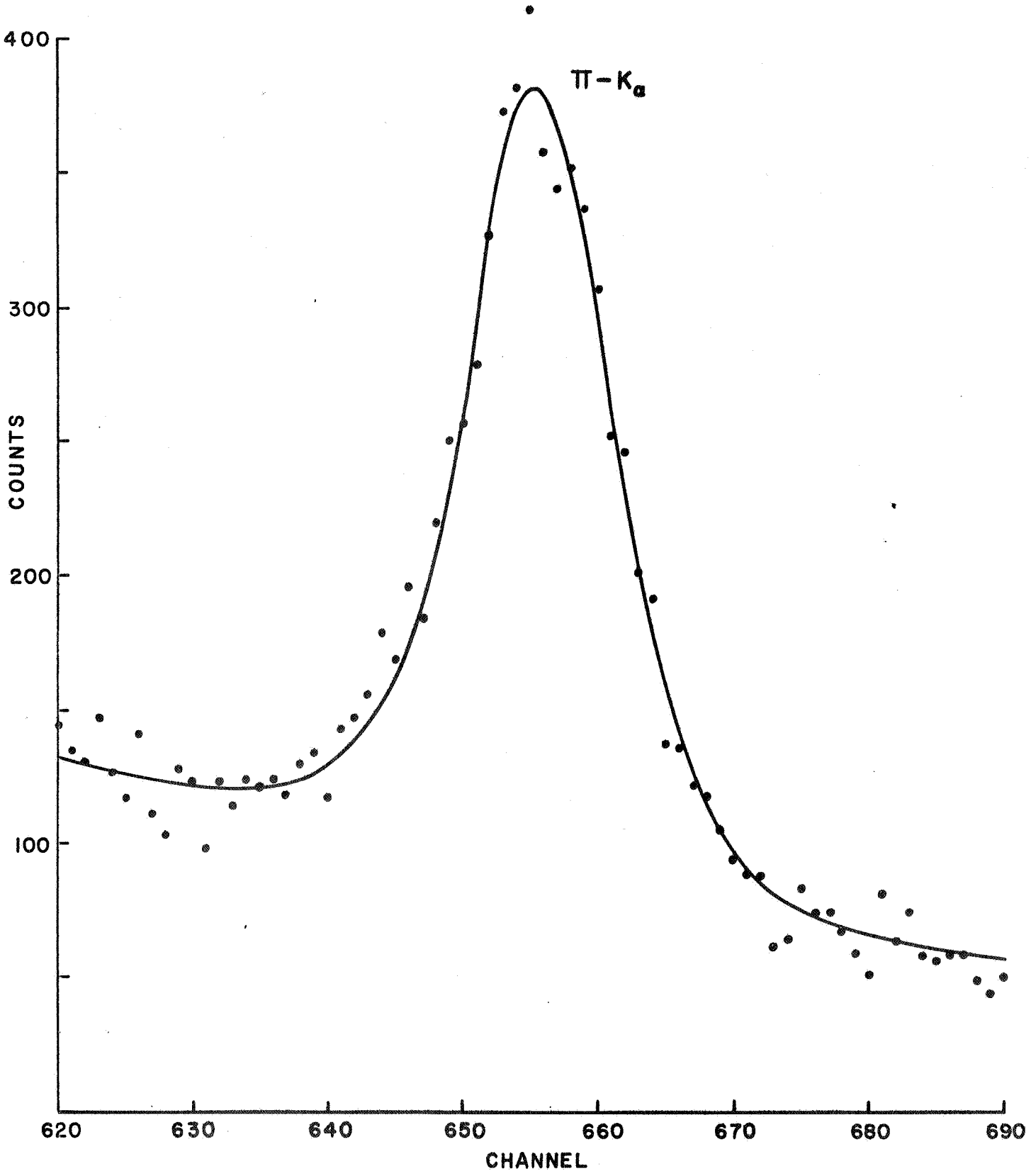
Be⁹ RUN A-20
400
300
200
100
COUNTS
π⁻ - Kα
620
630
640
650
660
670
680
690
CHANNEL

FIG. 16

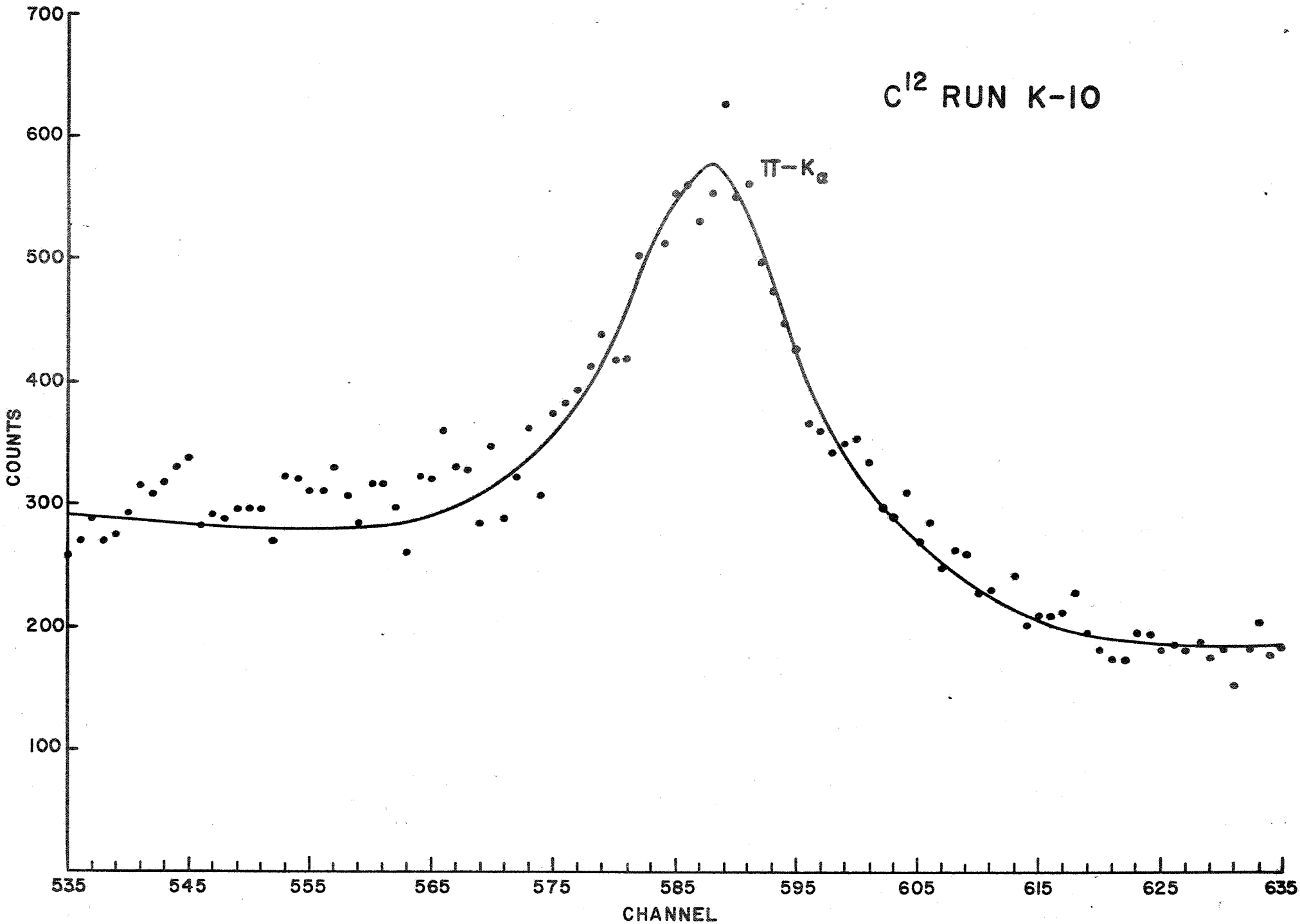
C12 RUN K-10
π−Kα
COUNTS
CHANNEL
700
600
500
400
300
200
100
535
545
555
565
575
585
595
605
615
625
635

FIG. 17

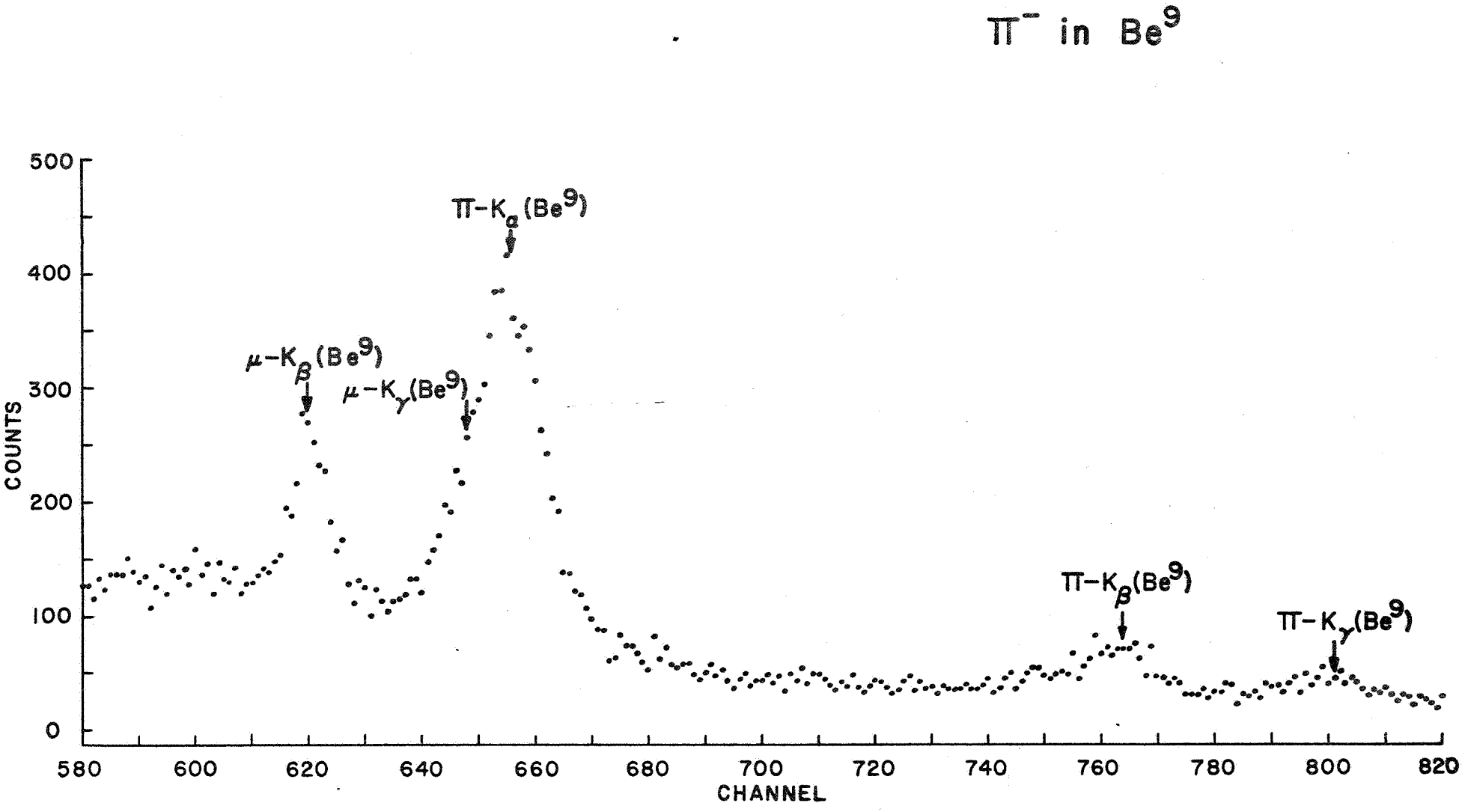
π^- in Be^9
π-K_α (Be^9)
μ-K_β (Be^9)
μ-K_γ (Be^9)
π-K_β (Be^9)
π-K_γ (Be^9)
COUNTS
CHANNEL
0
100
200
300
400
500
580
600
620
640
660
680
700
720
740
760
780
800
820

FIG. 18

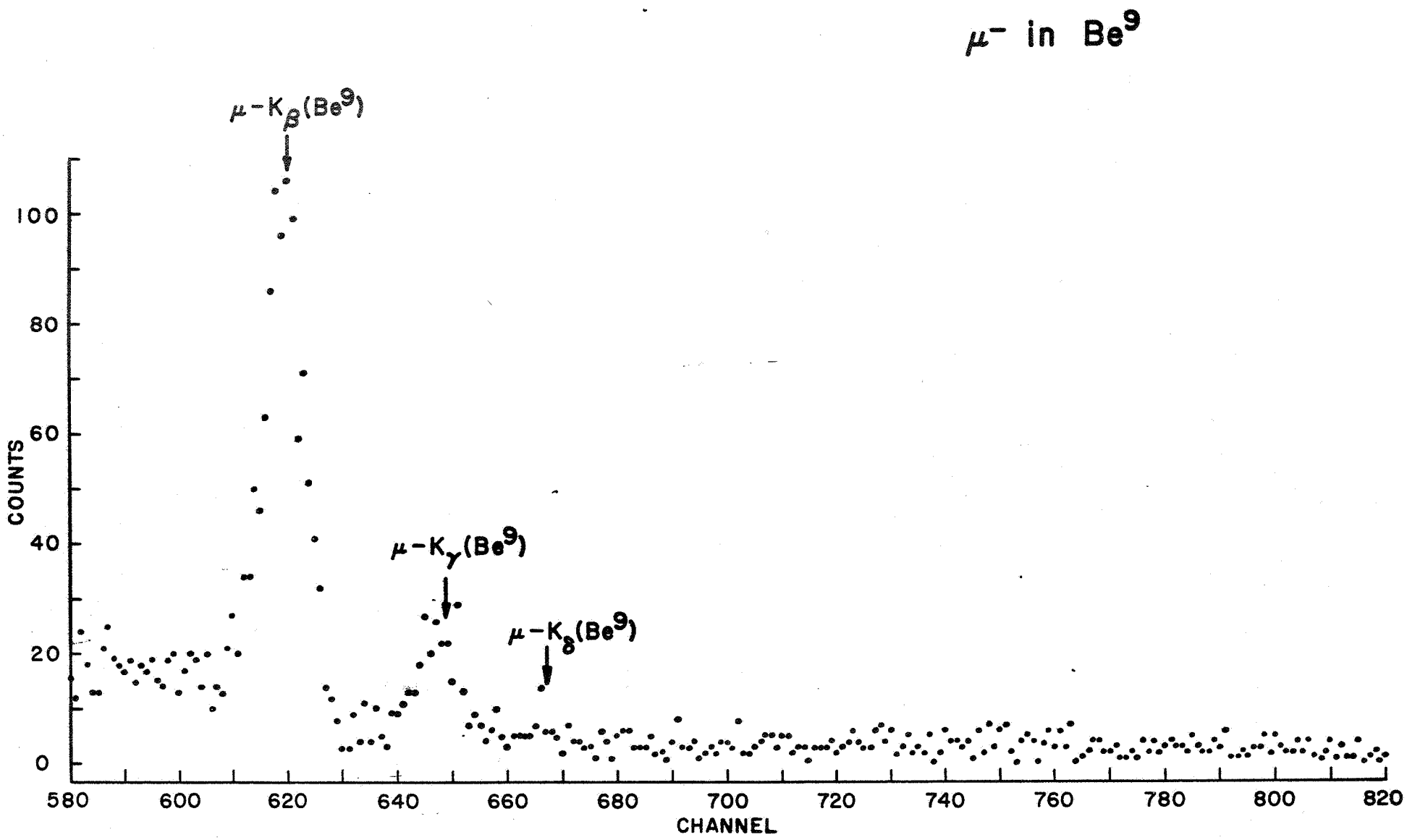
μ^- in Be^9
$\mu - K_\beta(Be^9)$
$\mu - K_\gamma(Be^9)$
$\mu - K_\delta(Be^9)$
COUNTS
0
20
40
60
80
100
580
600
620
640
660
680
700
720
740
760
780
800
820
CHANNEL

FIG. 19

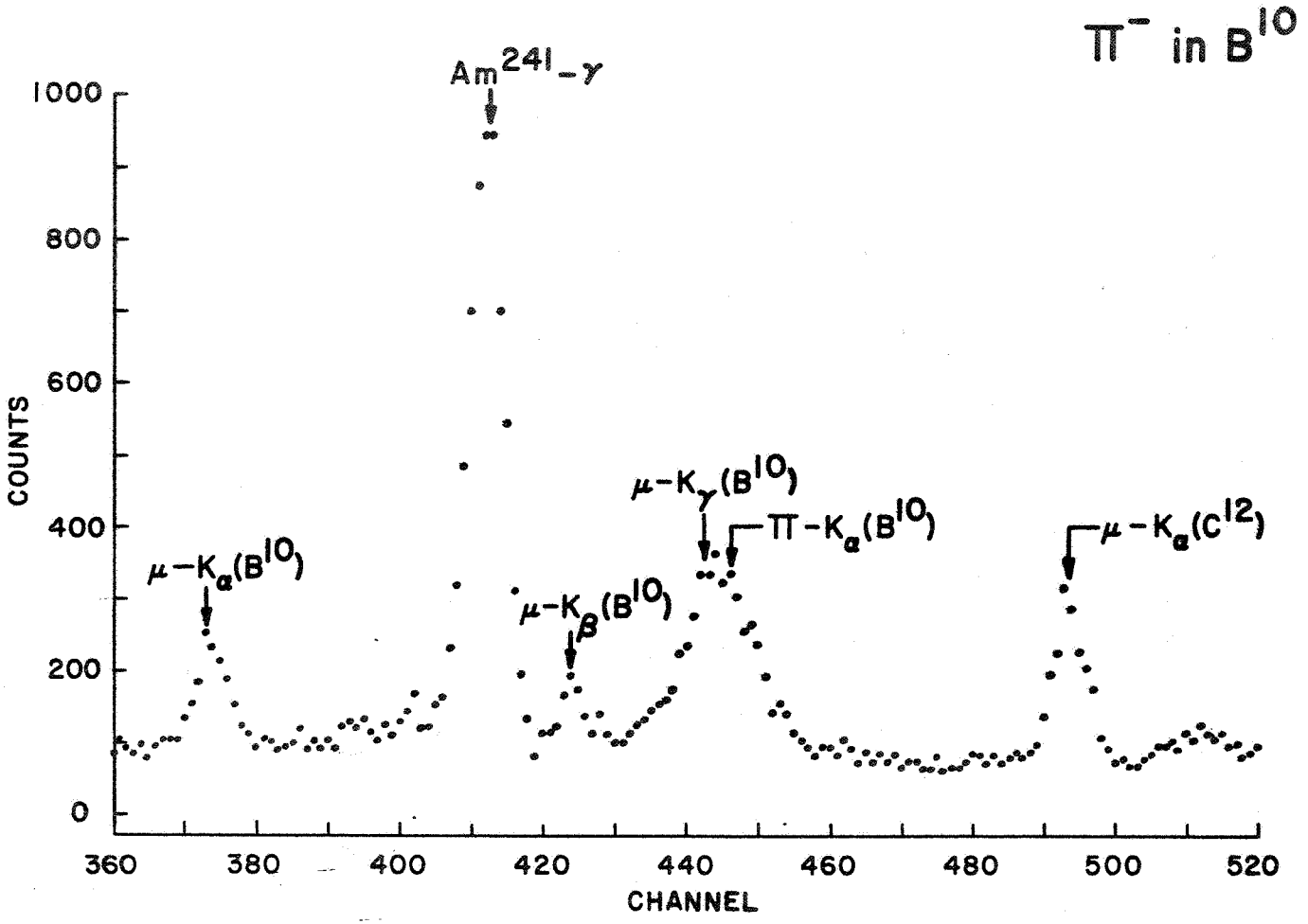
π^- in B^{10}
$Am^{241}-\gamma$
$\mu-K_\alpha(B^{10})$
$\mu-K_\beta(B^{10})$
$\mu-K_\gamma(B^{10})$
$\pi-K_\alpha(B^{10})$
$\mu-K_\alpha(C^{12})$
COUNTS
CHANNEL
0
200
400
600
800
1000
360
380
400
420
440
460
480
500
520

FIG. 20

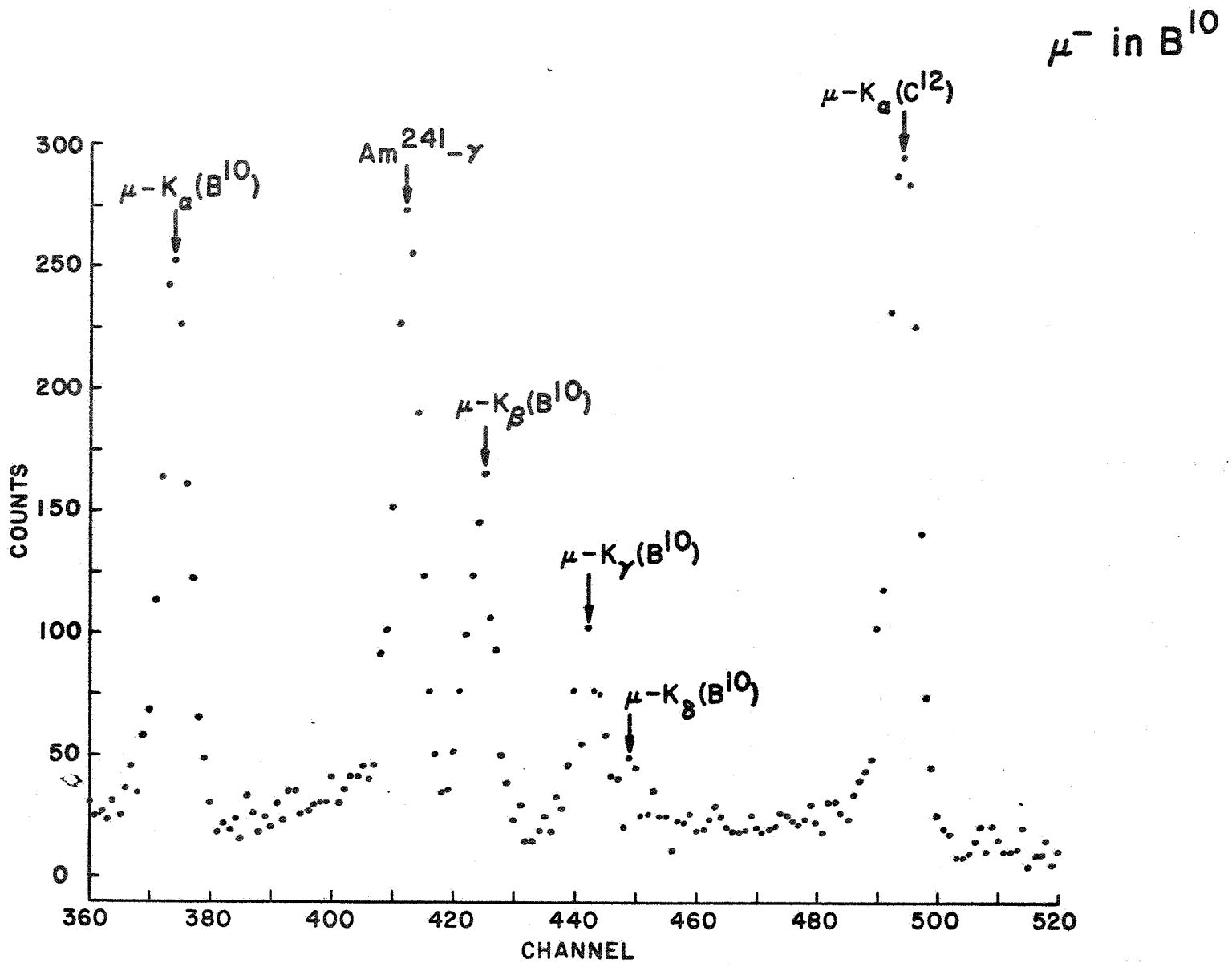
μ⁻ in B¹⁰
μ-Kα(C¹²)
Am²⁴¹-γ
μ-Kα(B¹⁰)
μ-Kβ(B¹⁰)
μ-Kγ(B¹⁰)
μ-Kδ(B¹⁰)
COUNTS
CHANNEL
300
250
200
150
100
50
0
360
380
400
420
440
460
480
500
520

FIG. 21

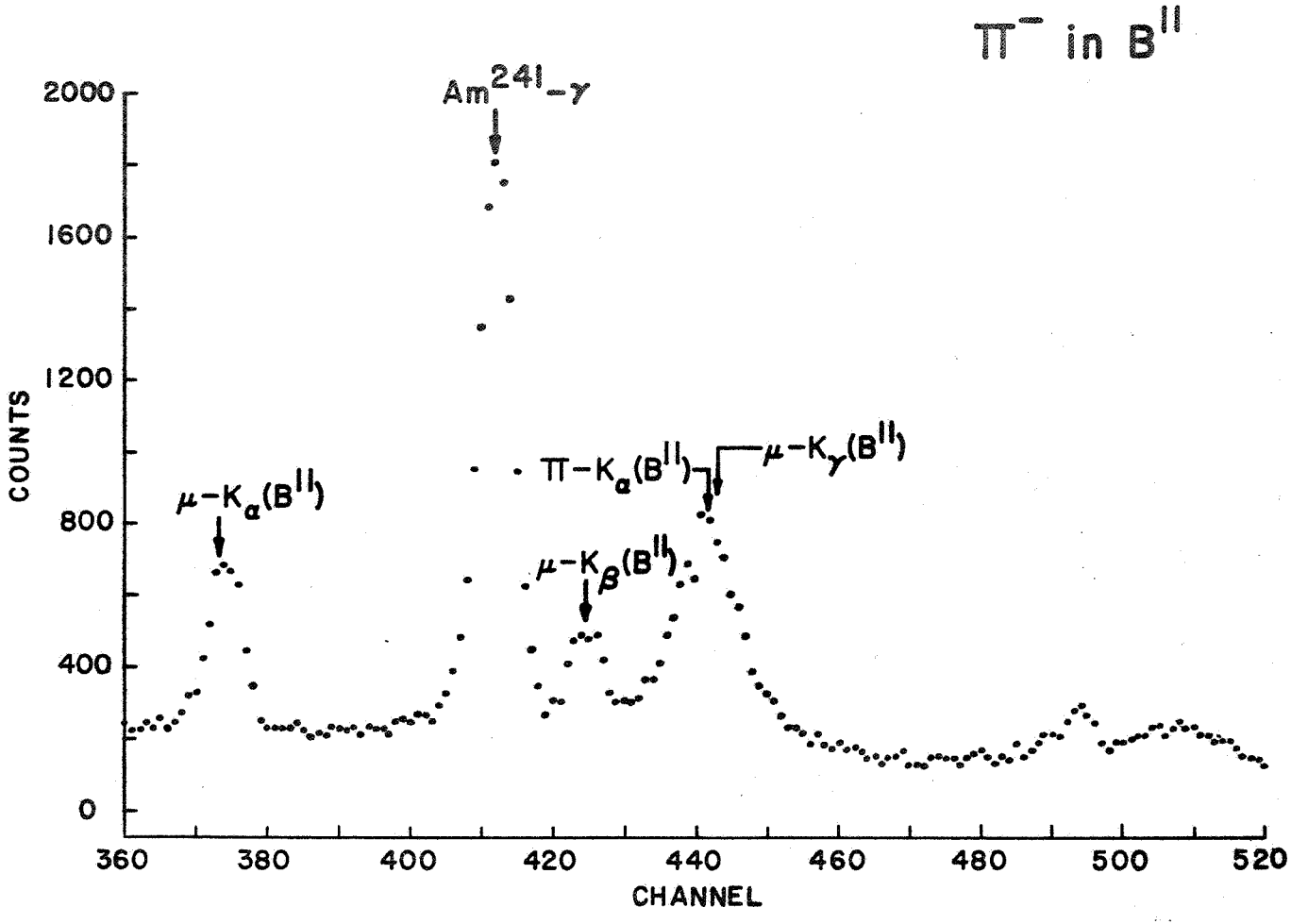
π^- in B^{11}
$Am^{241}-\gamma$
$\mu-K_\alpha(B^{11})$
$\pi-K_\alpha(B^{11})$
$\mu-K_\gamma(B^{11})$
$\mu-K_\beta(B^{11})$
COUNTS
2000
1600
1200
800
400
0
360
380
400
420
440
460
480
500
520
CHANNEL

FIG. 22

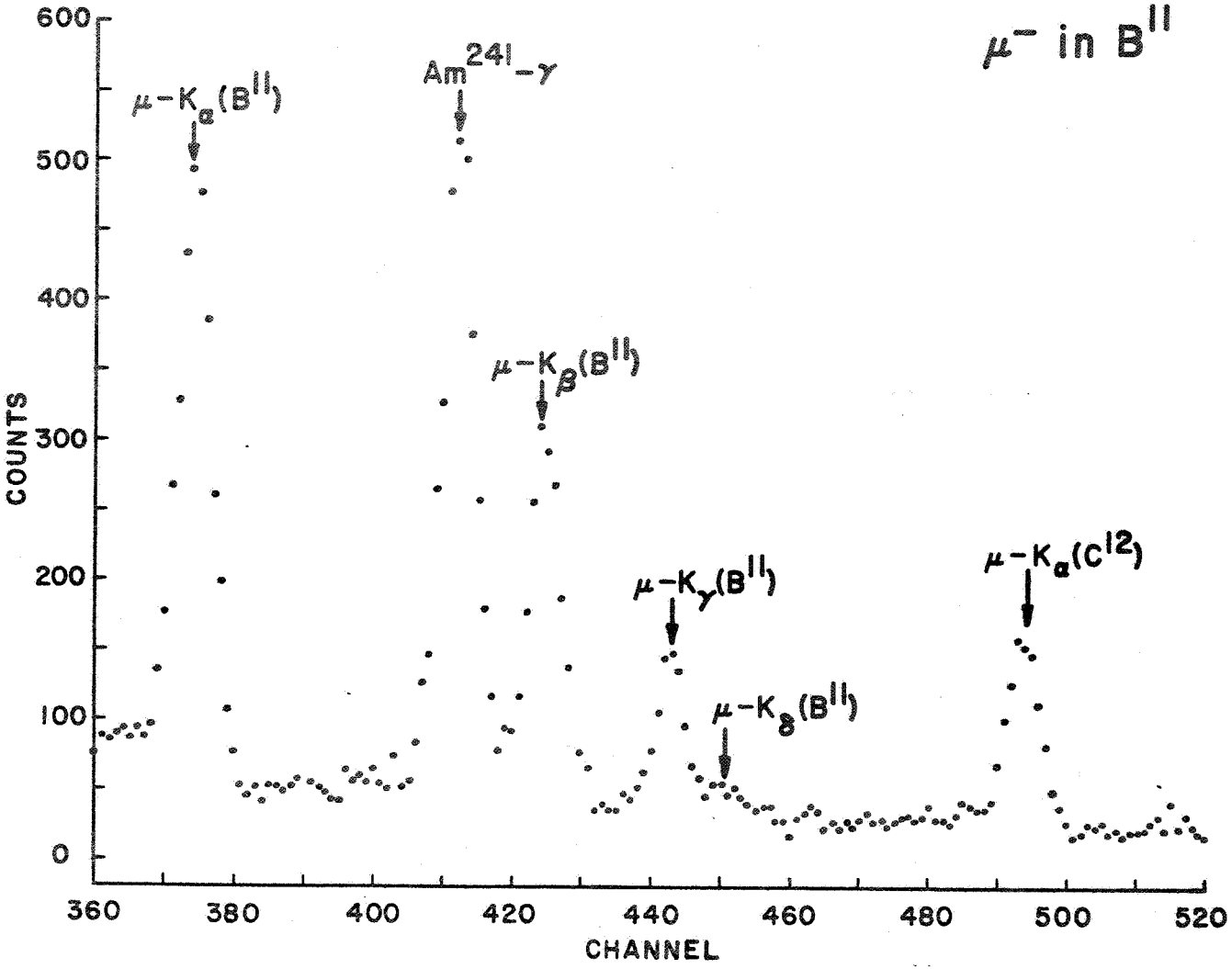
μ⁻ in B¹¹
μ-Kα(B¹¹)
Am²⁴¹-γ
μ-Kβ(B¹¹)
μ-Kγ(B¹¹)
μ-Kδ(B¹¹)
μ-Kα(C¹²)
COUNTS
CHANNEL
600
500
400
300
200
100
0
360
380
400
420
440
460
480
500
520

FIG. 23

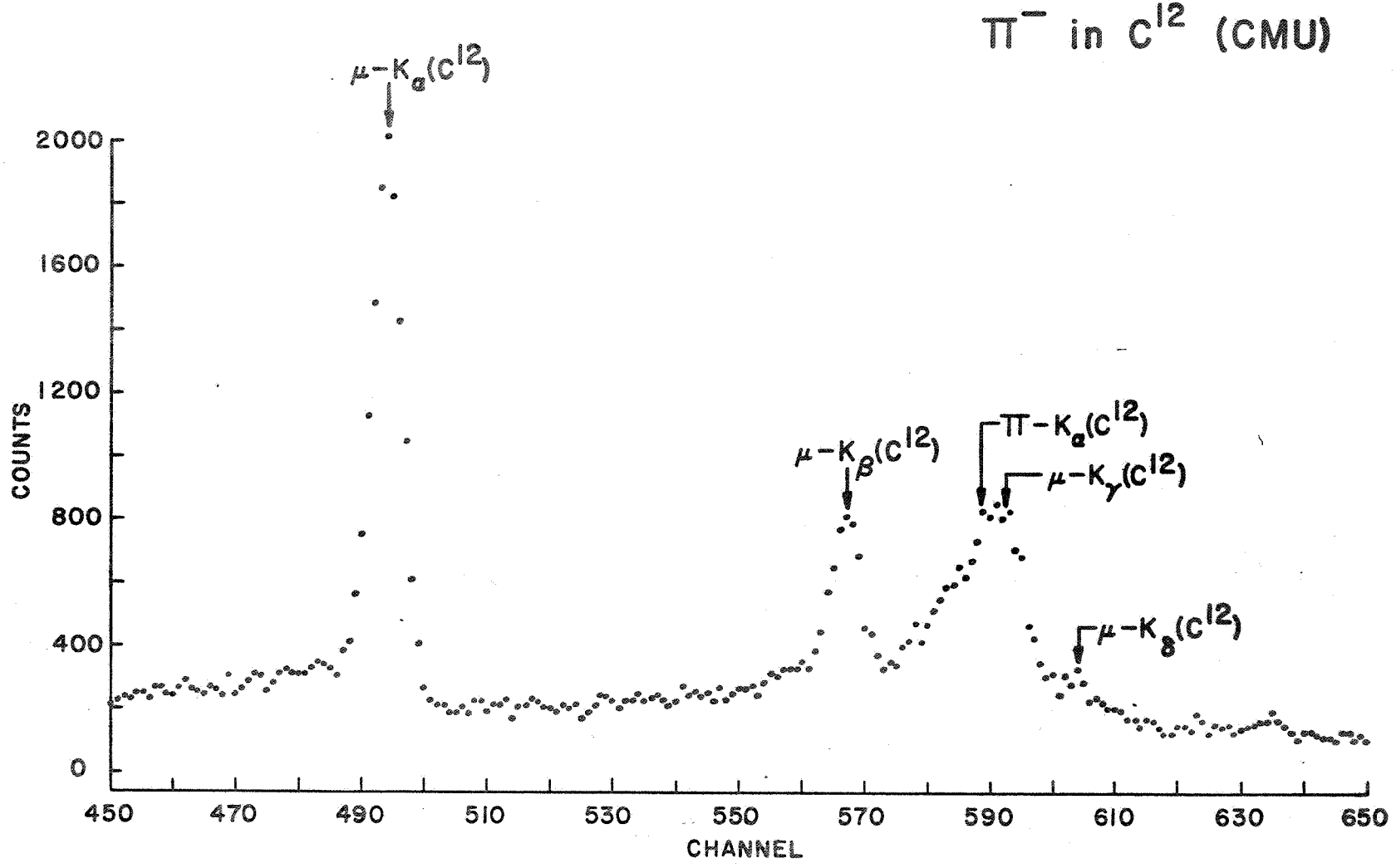
π^- in C^{12} (CMU)
$\mu-K_\alpha(C^{12})$
$\mu-K_\beta(C^{12})$
$\pi-K_\alpha(C^{12})$
$\mu-K_\gamma(C^{12})$
$\mu-K_\delta(C^{12})$
COUNTS
2000
1600
1200
800
400
0
450
470
490
510
530
550
570
590
610
630
650
CHANNEL

FIG. 24

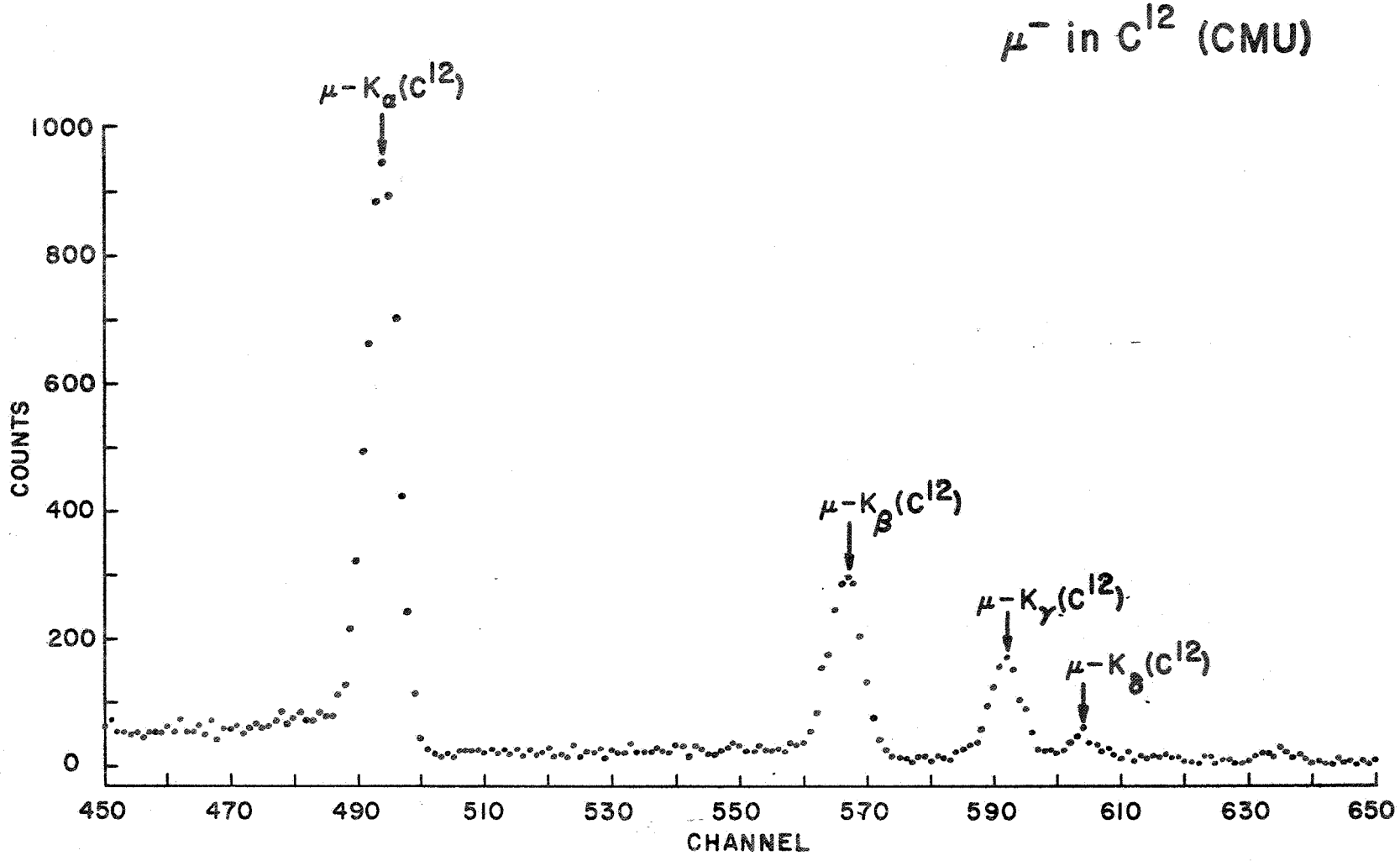
μ^- in C^{12} (CMU)
$\mu-K_\alpha(C^{12})$
$\mu-K_\beta(C^{12})$
$\mu-K_\gamma(C^{12})$
$\mu-K_\delta(C^{12})$
COUNTS
1000
800
600
400
200
0
450
470
490
510
530
550
570
590
610
630
650
CHANNEL

FIG. 25

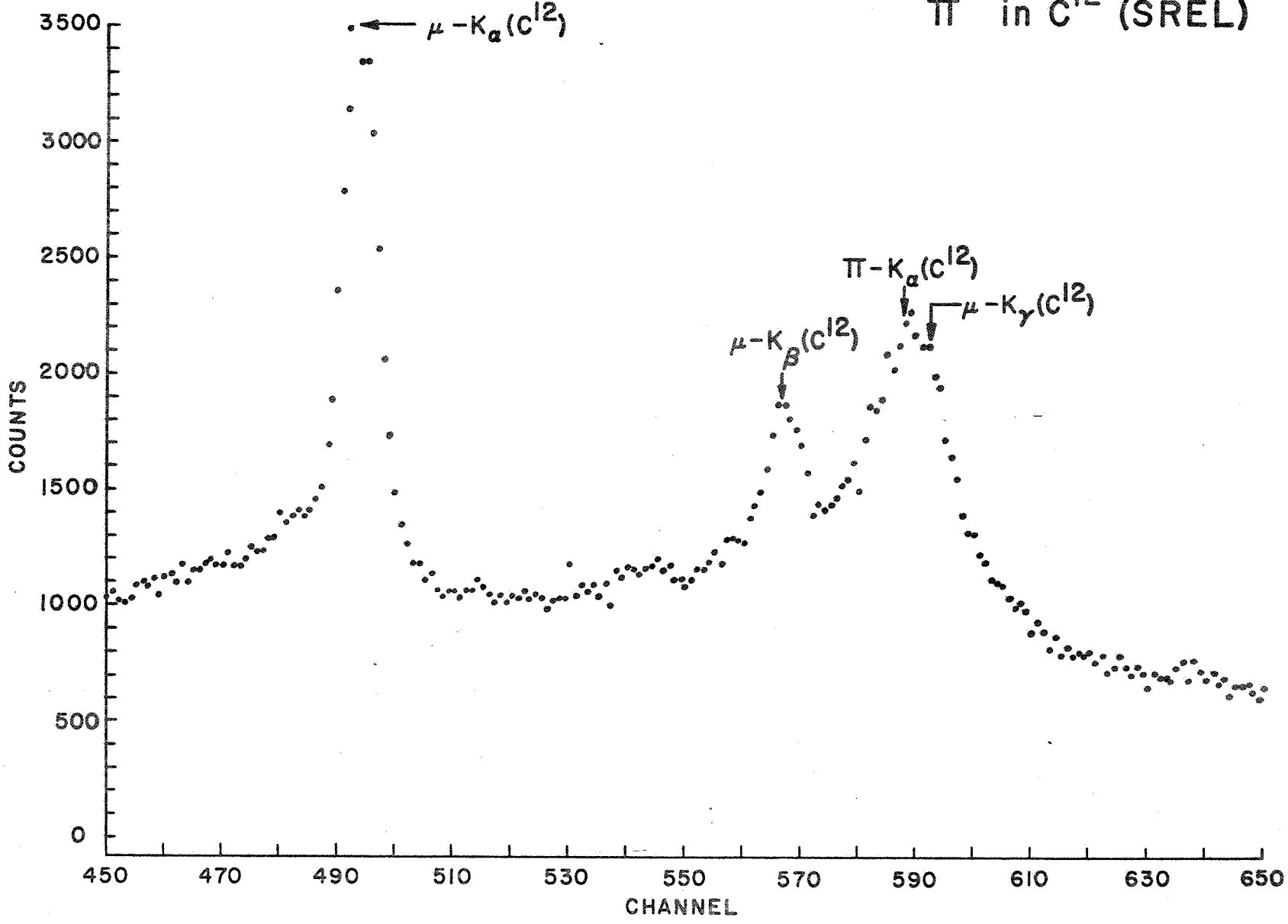
π^- in C^{12} (SREL)
$\mu - K_\alpha(C^{12})$
$\pi - K_\alpha(C^{12})$
$\mu - K_\beta(C^{12})$
$\mu - K_\gamma(C^{12})$
COUNTS
CHANNEL
0
500
1000
1500
2000
2500
3000
3500
450
470
490
510
530
550
570
590
610
630
650

FIG. 26

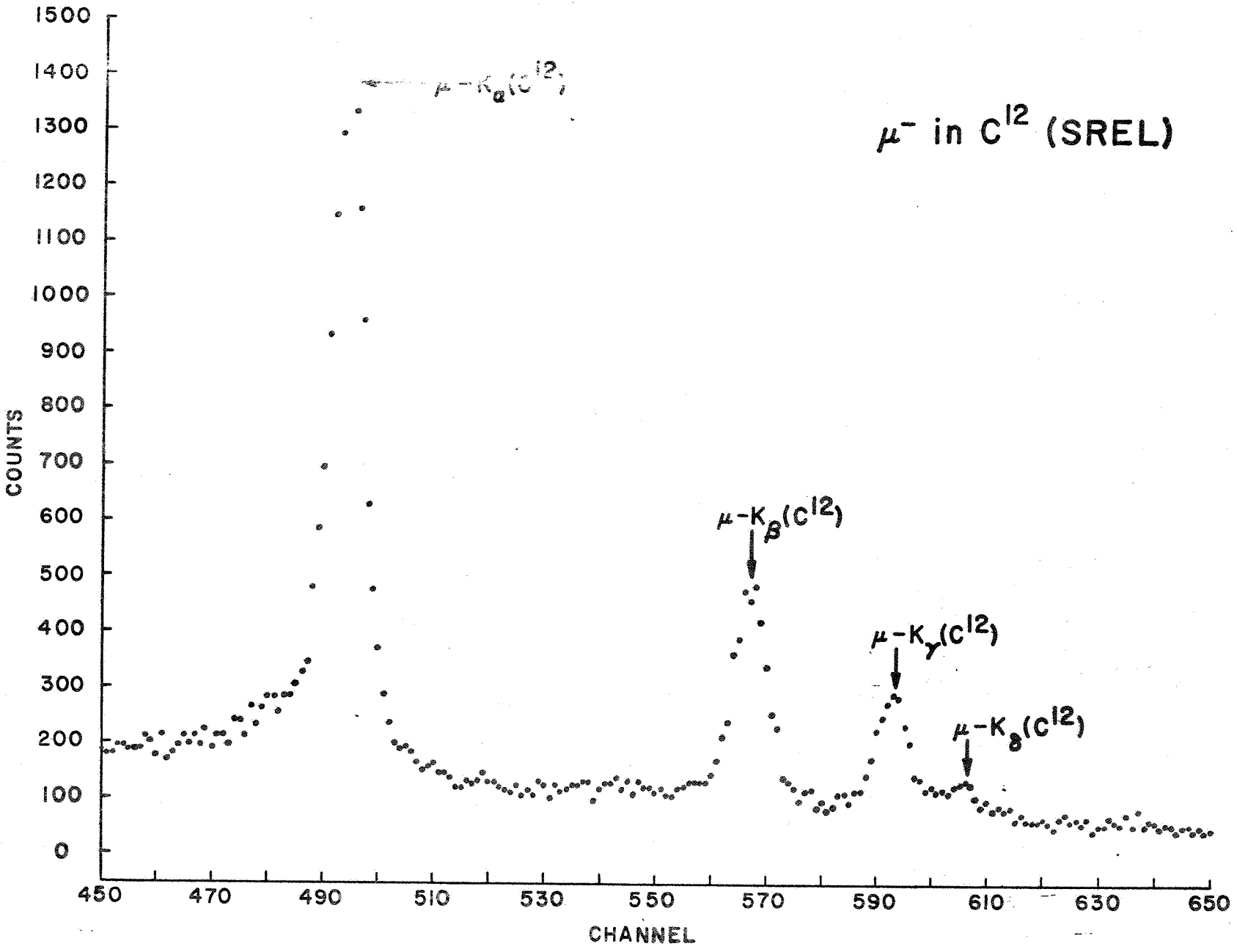
μ⁻ in C¹² (SREL)
μ-Kα(C¹²)
μ-Kβ(C¹²)
μ-Kγ(C¹²)
μ-Kδ(C¹²)
COUNTS
CHANNEL
0
100
200
300
400
500
600
700
800
900
1000
1100
1200
1300
1400
1500
450
470
490
510
530
550
570
590
610
630
650

FIG. 27

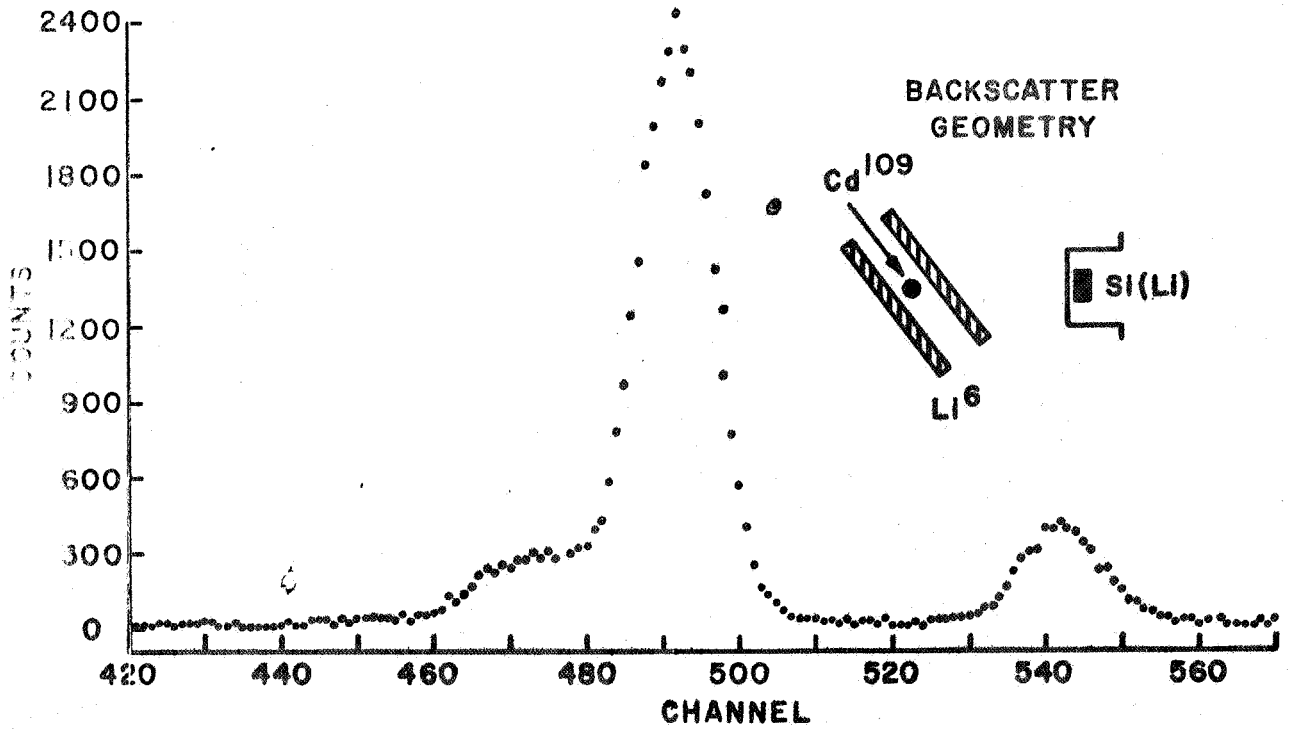

FIG. 28a

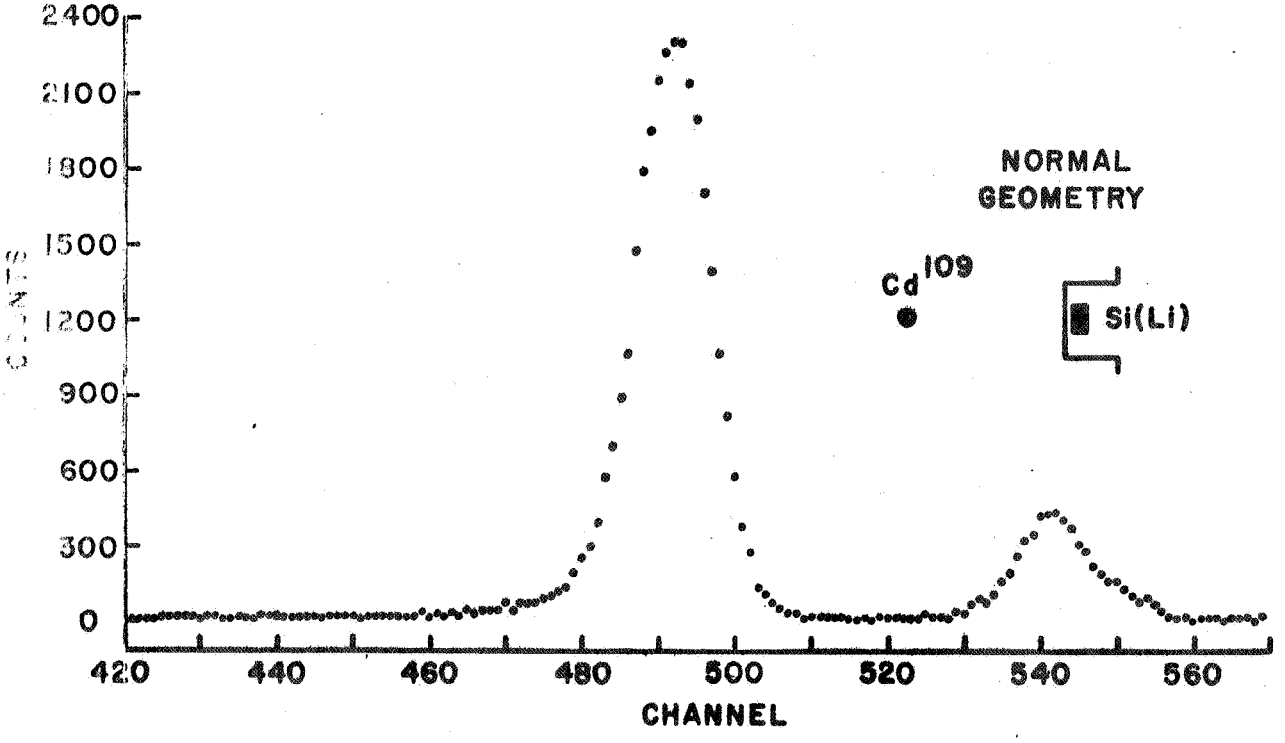

FIG. 28b

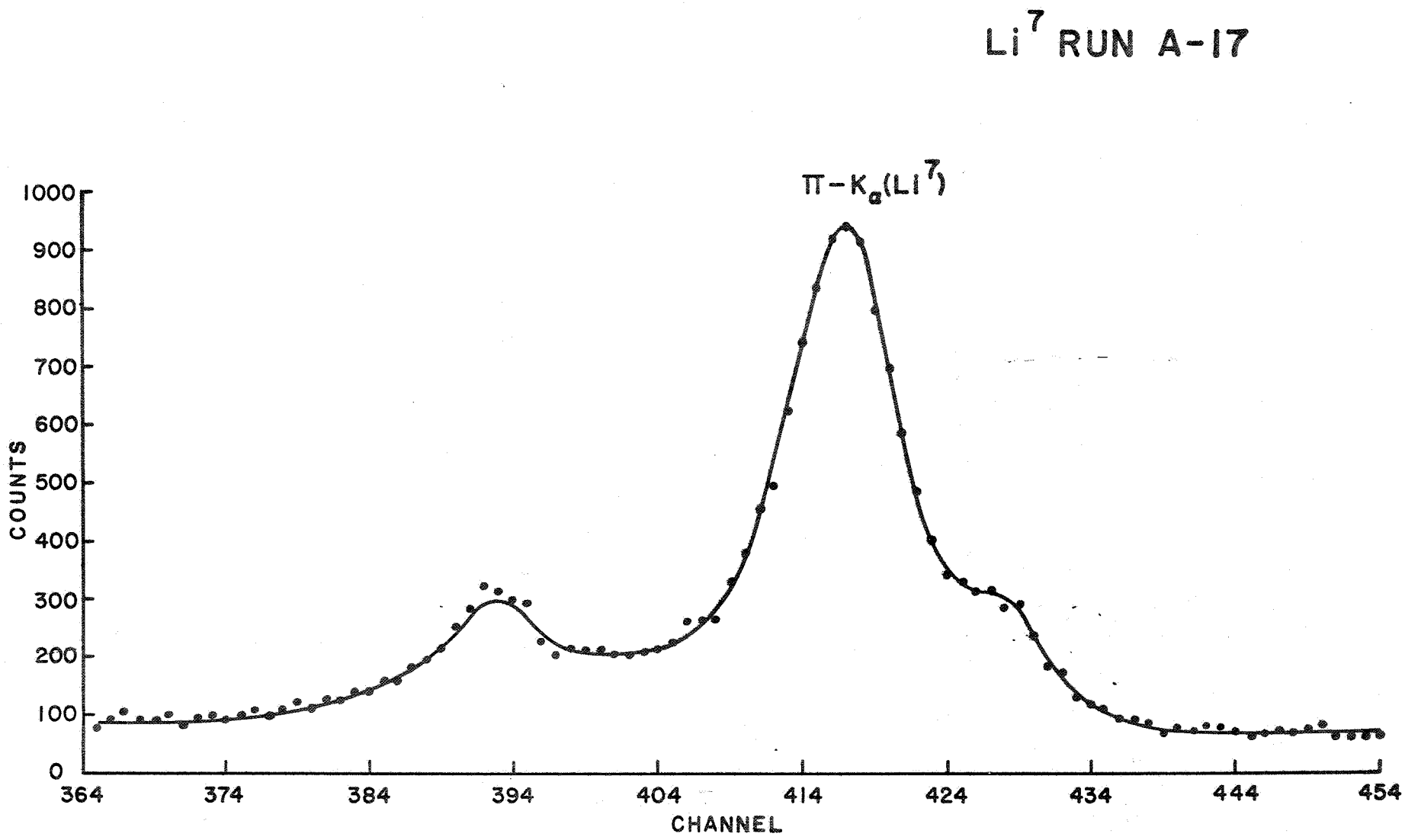
Li 7 RUN A-17
π−Kα(Li 7)
COUNTS
1000
900
800
700
600
500
400
300
200
100
0
364
374
384
394
404
414
424
434
444
454
CHANNEL

FIG. 29

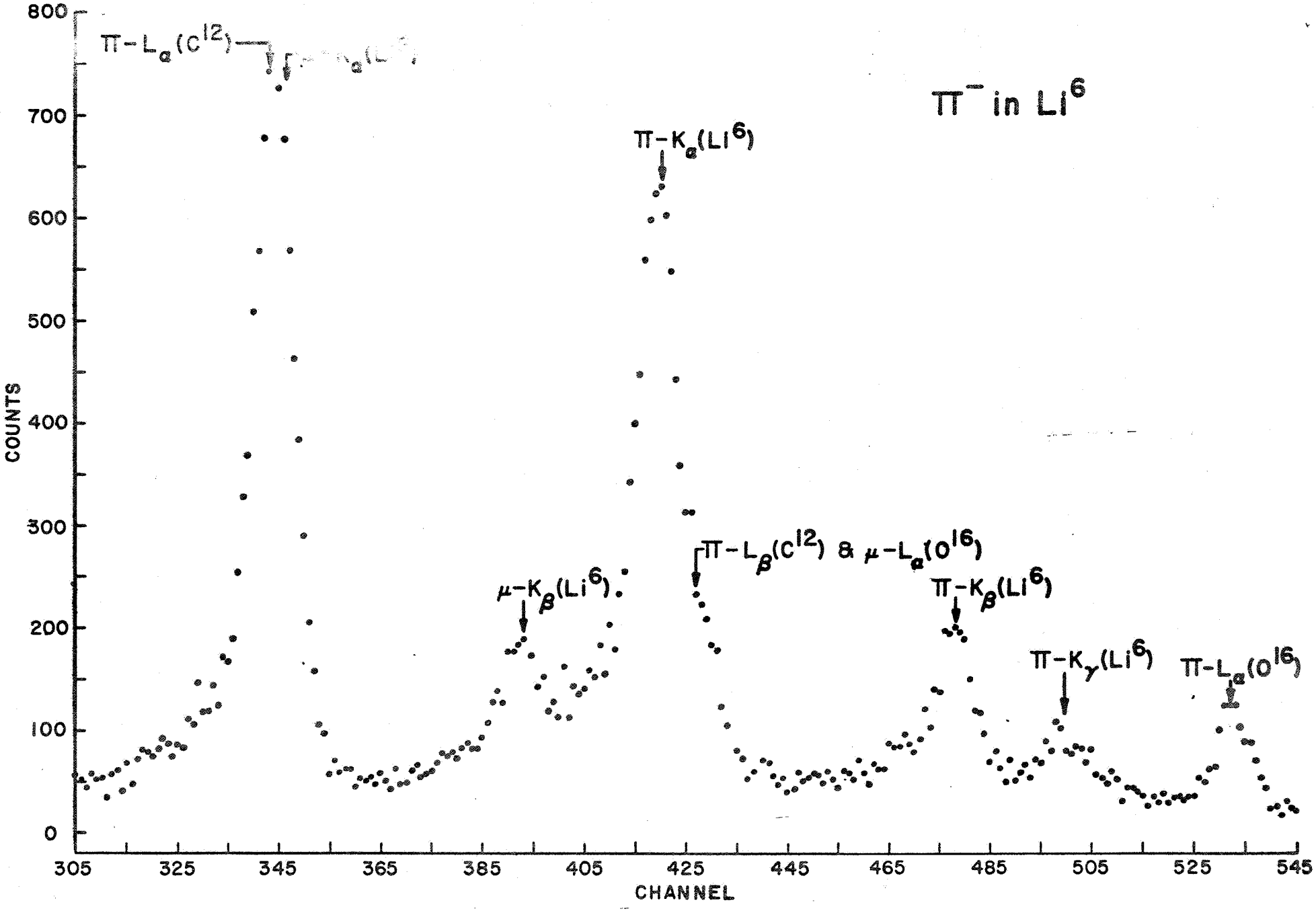
π⁻ in Li⁶
π-Lα(C¹²)
π-Kα(Li⁶)
μ-Kβ(Li⁶)
π-Lβ(C¹²) & μ-Lα(O¹⁶)
π-Kβ(Li⁶)
π-Kγ(Li⁶)
π-Lα(O¹⁶)
COUNTS
CHANNEL
0
100
200
300
400
500
600
700
800
305
325
345
365
385
405
425
445
465
485
505
525
545

FIG. 30

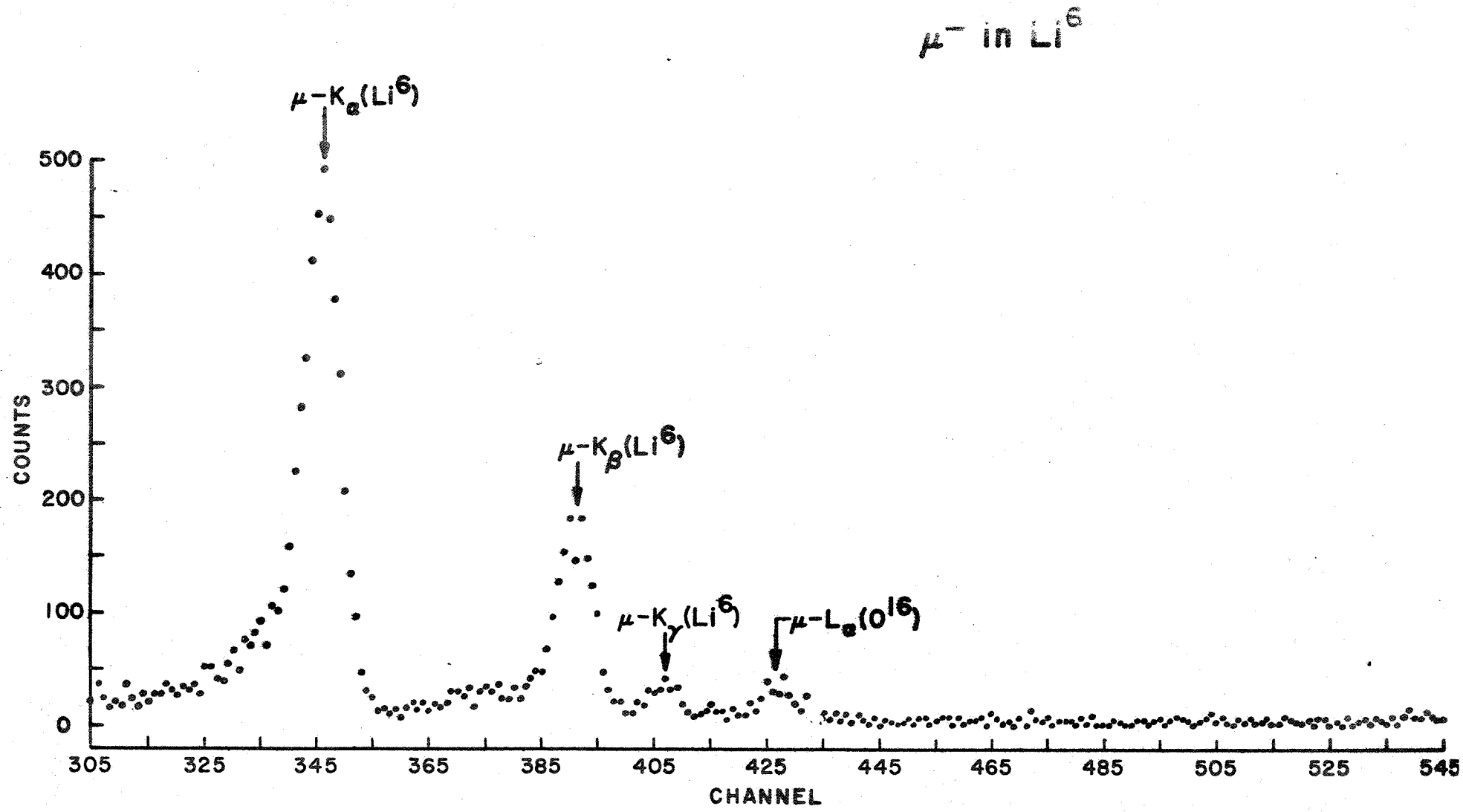
μ⁻ in Li⁶
μ-Kα(Li⁶)
μ-Kβ(Li⁶)
μ-Kγ(Li⁶)
μ-Lα(O¹⁶)
COUNTS
CHANNEL
0
100
200
300
400
500
305
325
345
365
385
405
425
445
465
485
505
525
545

FIG. 31

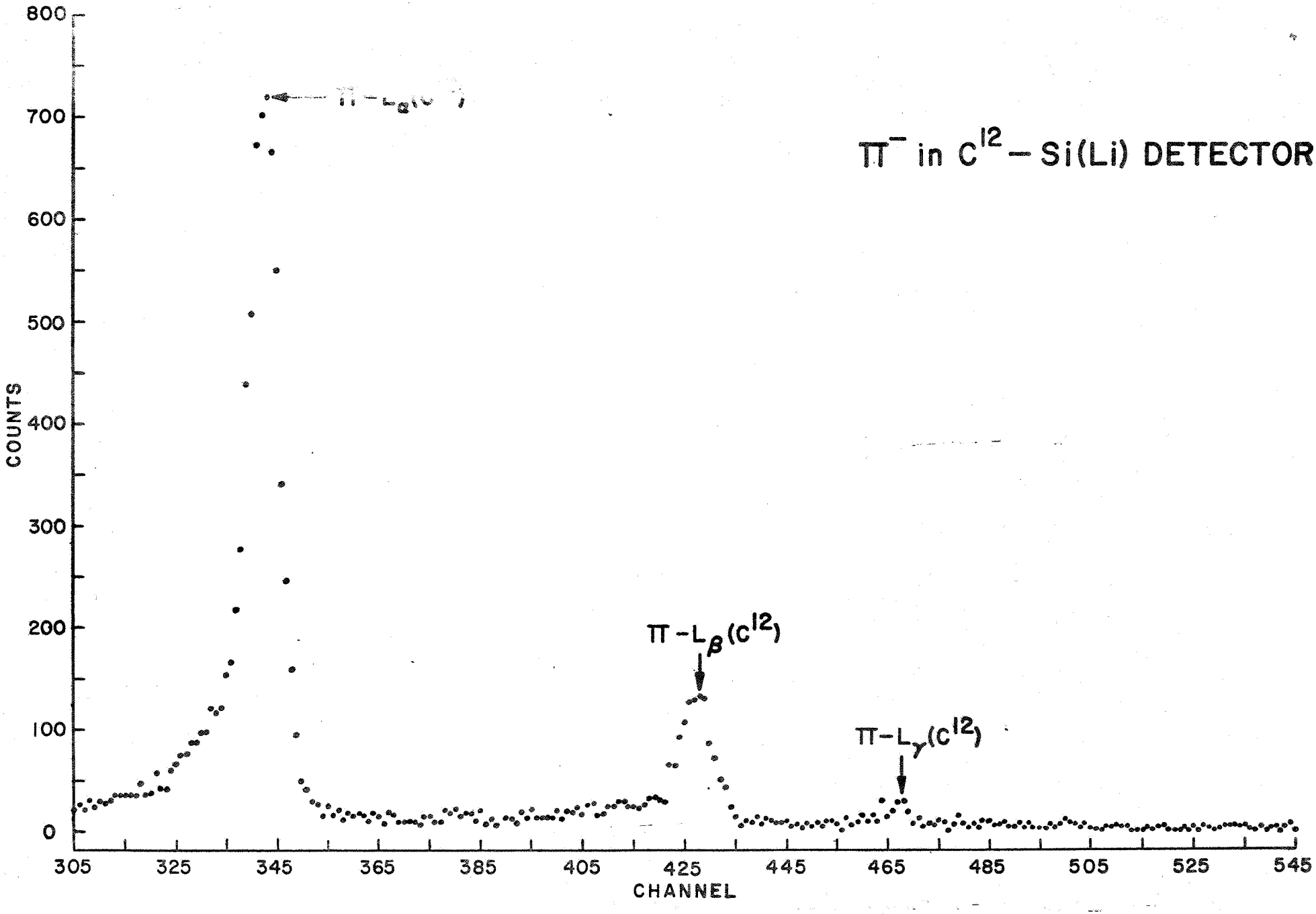
π^- in C^{12} – Si(Li) DETECTOR
COUNTS
CHANNEL
$\pi - L_\beta (C^{12})$
$\pi - L_\gamma (C^{12})$
800
700
600
500
400
300
200
100
0
305
325
345
365
385
405
425
445
465
485
505
525
545

FIG. 72

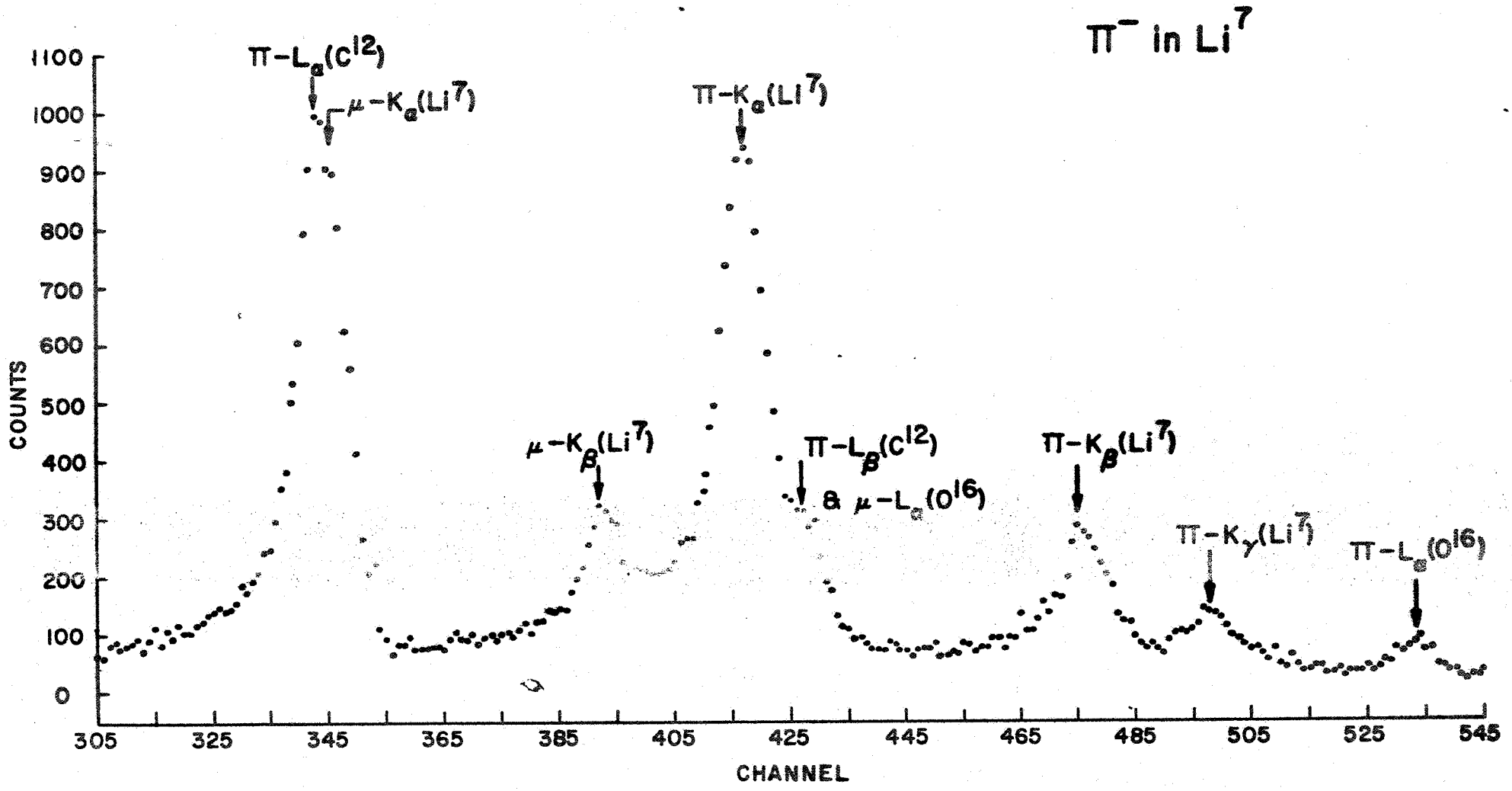
π⁻ in Li⁷
π-L_α(C¹²)
μ-K_α(Li⁷)
π-K_α(Li⁷)
μ-K_β(Li⁷)
π-L_β(C¹²)
& μ-L_α(O¹⁶)
π-K_β(Li⁷)
π-K_γ(Li⁷)
π-L_α(O¹⁶)
COUNTS
CHANNEL
0
100
200
300
400
500
600
700
800
900
1000
1100
305
325
345
365
385
405
425
445
465
485
505
525
545

FIG. 33

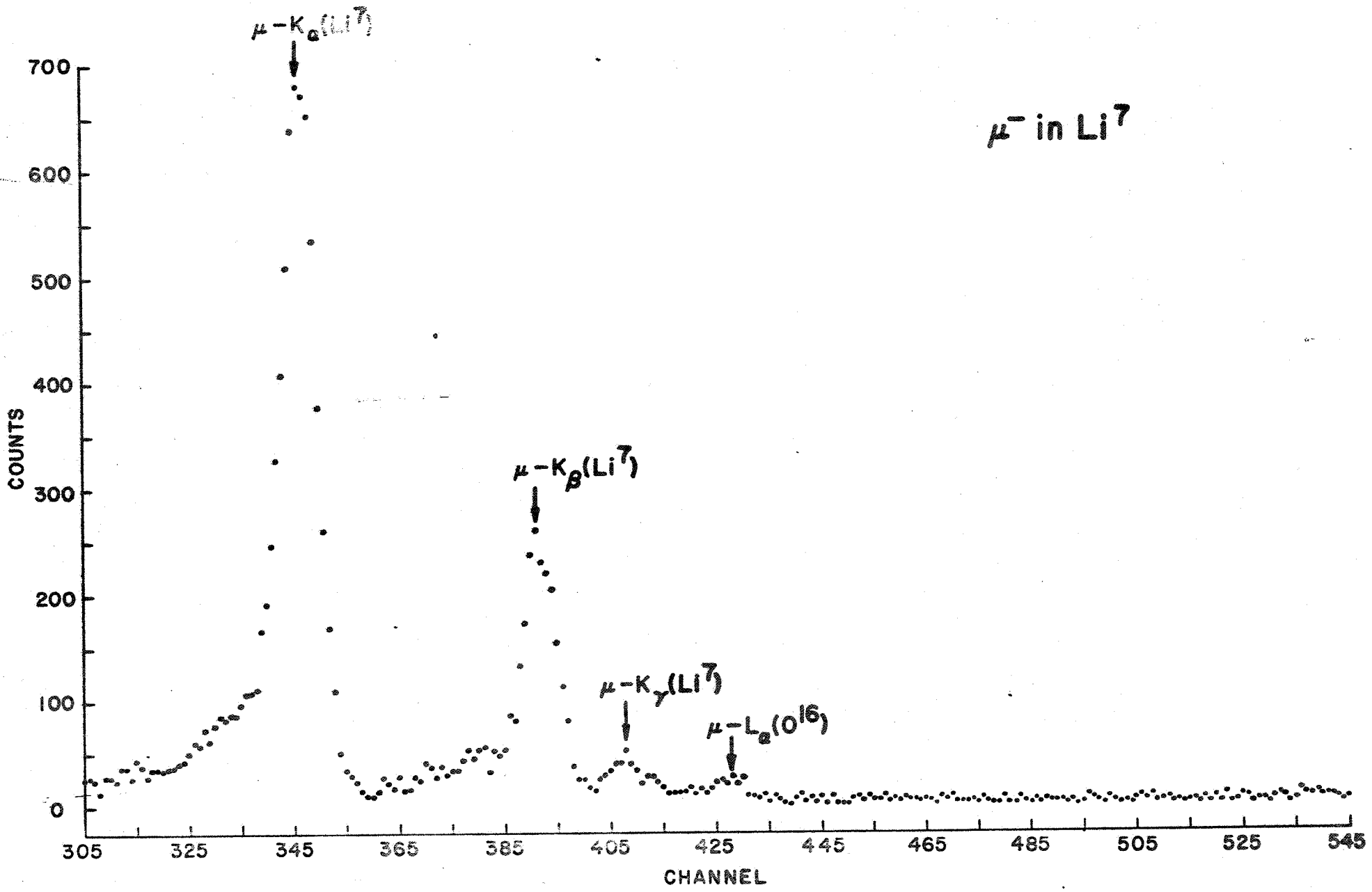
μ⁻ in Li⁷
μ−Kα(Li⁷)
μ−Kβ(Li⁷)
μ−Kγ(Li⁷)
μ−Lα(O¹⁶)
COUNTS
CHANNEL
0
100
200
300
400
500
600
700
305
325
345
365
385
405
425
445
465
485
505
525
545

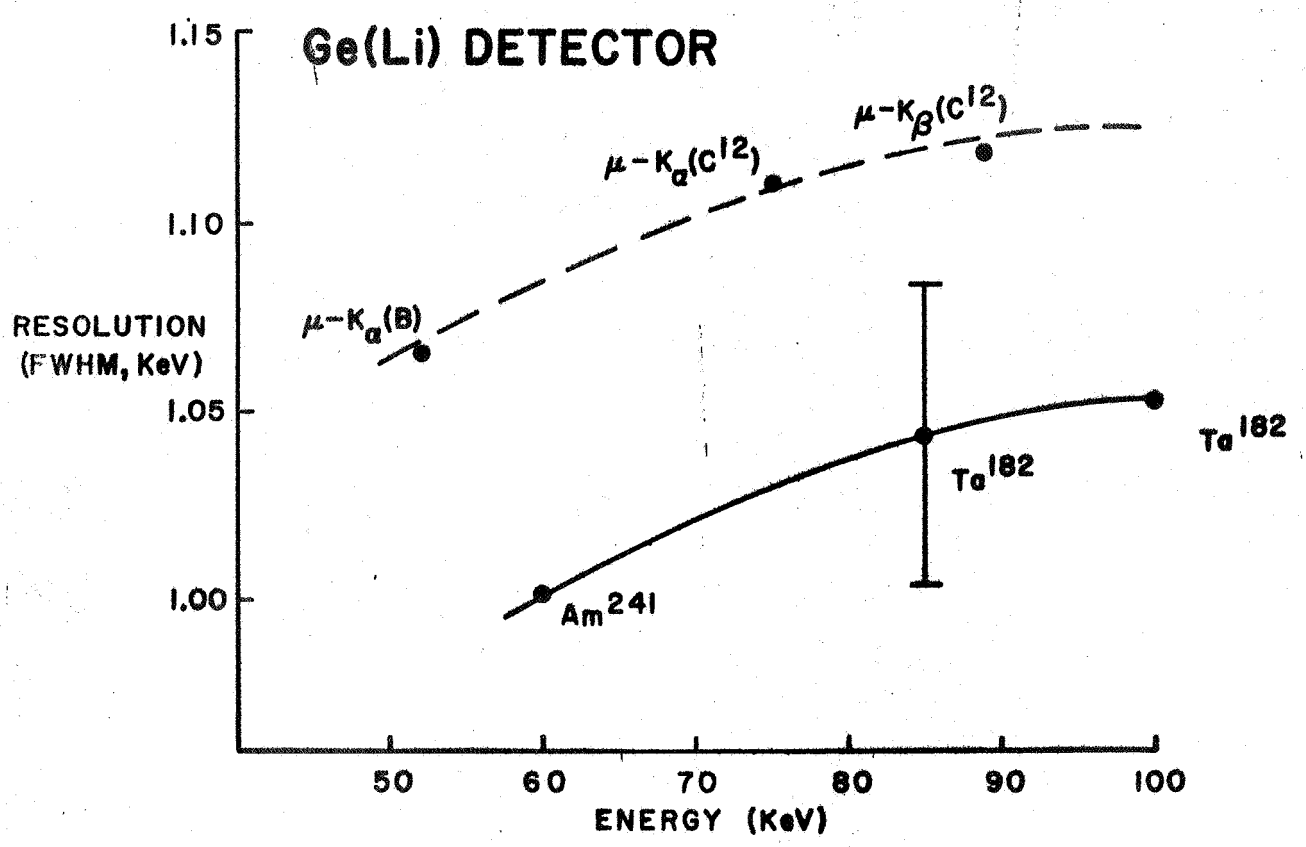

FIG. 35a

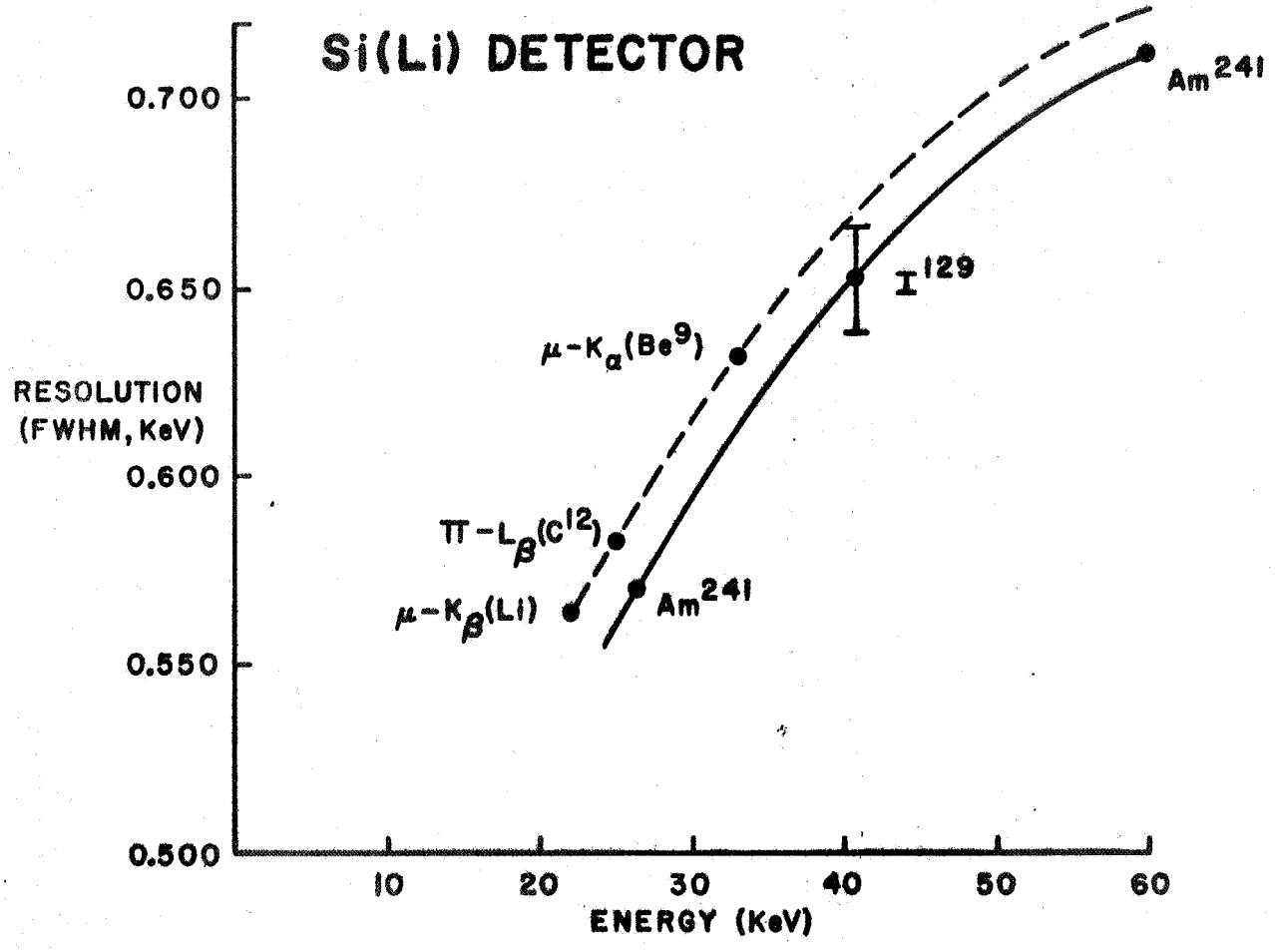

FIG. 35b

ERRATA

P. 4; 2nd line: Read e^2 for e.

P. 59; 1st, 4th and 6th lines: Read K for L.

P. 89; 5th line: Read 0.00 ± 0.09 for 0.00 ± 0.06

P. 96; Ref. 24: Read Yamazaki for Yamazoki